

# **FIELD STABILITY AND EXTERNAL INTERFERENCE SHIELDING OF 1.5 T CLINICAL MRI SCANNER**

**A Thesis Submitted  
in Partial Fulfilment of the Requirements for the  
Degree of**

**DOCTOR OF PHILOSOPHY**

**by**

**AJIT DATTU NANDAWADEKAR**

(Roll No. 2K20/PhD/EE/10)

**Under the Supervision of**

**Dr. Mukhtiar Singh  
Professor  
Department of Electrical  
Engineering**

**Dr. Soumen Kar  
Scientist - G  
Inter-University  
Accelerator Centre (IUAC)**



**To the**

**Department of Electrical Engineering  
DELHI TECHNOLOGICAL UNIVERSITY  
(Formerly Delhi College of Engineering)  
Shahbad Daultapur, Main Bawana Road, Delhi-110042, India**



## ACKNOWLEDGMENT

I would like to express my heartfelt thanks to everyone who has directly or indirectly contributed to my journey, without whose support this accomplishment would not have been possible. First and foremost, I owe my deepest gratitude to the Almighty for His divine grace and blessings, which enabled me to successfully complete the highest degree in the engineering discipline of my life.

I would like to express my sincere appreciation to my thesis supervisor, **Prof. Mukhtiar Singh**, Department of Electrical Engineering, Delhi Technological University. His exceptional guidance, unwavering encouragement, and positive outlook have been a constant source of motivation throughout my research journey. His insightful feedback and support have played a significant role in shaping this work.

I also wish to convey my utmost gratitude and profound respect to my research co-supervisor, **Dr. Soumen Kar** (Scientist G, IUAC, Delhi), for his invaluable guidance and continuous support throughout this research. His expertise and mentorship have been instrumental in the successful completion of this work.

A special thanks to **Dr. R.G. Sharma** (Emeritus Scientist, MeitY MRI Project Advisor), whose ongoing guidance and support have been crucial to my progress. I am truly grateful for his advice and encouragement during this entire process.

I gratefully acknowledge the Ministry of Electronics and Information Technology (MeitY), India, for providing the project funding that made this research possible. Additionally, I extend my sincere thanks to the Society for Applied Microwave Electronics Engineering & Research (SAMEER), Delhi Technological University, for their continued support throughout the course of my work.

I would also like to extend my heartfelt gratitude to the staff at the Inter-University Accelerator Centre (IUAC), including **Mr. Manoj Kumar, Mr. Suresh Babu, Mr. S.K. Saini, Dr. Joby Antony, Mr. Ganesh Chaudhari and Mr. Rajesh Kumar**, for their assistance and guidance in the projects and day-to-day activities. Their expertise has been indispensable to my research.

I am grateful to my colleagues **Vijay Soni, Sankar Ram T, Navneet Kumar, Bhavana Avasthi**, and **Farukh Khan**, whose help and support were invaluable in carrying out the experimental work for this research. I have learned much from working alongside them. I would also like to express my sincere appreciation to the technicians at IUAC for their continuous support and efforts throughout these years.

I find it difficult to express in words my deep gratitude to my siblings, their families, and my own family members. Their unwavering moral support and countless sacrifices have been my pillars of strength throughout this journey.

Lastly, I would like to thank everyone, both at IUAC and beyond, who has helped me, either directly or indirectly, in completing this work. Their assistance, in whatever form, has been vital in bringing this research to fruition.

Thank you all.

**DEDICATED TO MY BELOVED SISTERS**

**Meena and Sumitra**

## **CANDIDATE'S DECLARATION**

I, Ajit Dattu Nandawadekar, hereby certify that the work which is being presented in the thesis entitled 'Field Stability and External Interference Shielding of 1.5 T Clinical MRI Scanner' in partial fulfillment of the requirements for the award of the Degree of Doctor of Philosophy, submitted in the Department of Electrical Engineering of Delhi Technological University is an authentic record of my own work carried out during the period from Aug 2020 to Nov 2024 under the supervision of Prof. Mukhtiar Singh and Dr. Soumen Kar.

The matter presented in the thesis has not been submitted by me for the award of any other degree of this or any other Institute.

**Candidate's Signature**

## **CERTIFICATE BY THE SUPERVISORS**

Certified that Ajit Dattu Nandawadekar, (Roll No. 2K20/PhD/EE/10) has carried out their research work presented in this thesis entitled 'Field Stability and External Interference Shielding of 1.5 T Clinical MRI Scanner' for the award of Doctor of Philosophy from Department of Electrical Engineering, Delhi Technological University, Delhi, under our supervision. The thesis embodies results of original work, and studies are carried out by the student himself and the contents of the thesis do not form the basis for the award of any other degree to the candidate or to anybody else from this or any other University/Institution.

**Dr. Mukhtiar Singh**

Professor

Department of Mechanical Engineering

Delhi Technological University

**Dr. Soumen Kar**

Scientist - G

Inter-University

Accelerator Centre (IUAC)

**Date:**





## ABSTRACT

Ministry of Electronics and Information Technology (MeitY), Government of India, has initiated a project to develop a 1.5 T superconducting MRI scanner in India. Inter-University Accelerator Centre (IUAC), New Delhi, is primarily responsible for the development of a 1.5 T superconducting magnet and an ever-cooled cryostat for the MRI scanner. An actively shielded 1.5 T superconducting MRI magnet has been designed for a whole-body clinical scanner. The MRI magnet generates a 1.5 T magnetic field in a 45 cm Diametrical Spherical Volume (DSV) with  $\pm 5.5$  ppm homogeneity. The magnet has been wound by using braided polyethylene terephthalate (PET) insulated wire in channel (WIC) Niobium Titanium (NbTi) (low-temperature superconductor) wire on the bobbin. MRI magnet operates at 4.2 K (liquid helium) temperature, and its operating current is 450 A.

This thesis presents a comprehensive study focused on advancing the development and understanding of critical components in a 1.5 T actively shielded superconducting MRI magnet. The research addresses both theoretical and practical aspects essential for optimizing MRI performance, with a particular emphasis on superconducting joints, Persistent Current Switch (PCS), Electromagnetic Interference Shielding (EIS) coils, and cryogenic components.

The research provides a detailed analysis of various superconducting joint-making techniques, discussing their advantages and disadvantages from an industrial perspective. Additionally, the study explores the solder matrix replacement method for different joints, including Cu-NbTi to Cu-NbTi and CuNi-NbTi to Cu-NbTi conductors. The reasons for superconducting joint failures are thoroughly analyzed using Scanning Electron Microscopy (SEM) and Energy Dispersive X-ray (EDX) techniques, offering insights into improving joint reliability. A key achievement of this study is the development of a 4 K insert, which has enabled precise characterization of superconducting joints, an essential component for ensuring the stability and efficiency of MRI magnets. The insert has demonstrated the ability to achieve near-

perfect superconducting conditions, with measured electrical resistance as low as  $8 \times 10^{-15} \Omega$  at zero field between various conductor pairs.

The research has also contributed significantly to the development and testing of a prototype PCS designed for a whole-body MRI magnet. This system is crucial for maintaining the magnet's stability and operational efficiency. Through a comparative analysis of temperature profiles and switching behaviors across various thermo-foil heaters, the study identified optimal operating conditions.

The design of an EIS coil involves careful consideration of various factors, including the coupling factor, mutual inductance, turns ratio, geometrical factors, and self-inductance. The design process includes defining specifications, initial design choices, simulation and optimization, final development, and rigorous testing to ensure the final coil design delivers accurate and reliable measurements. Additionally, the study explored the EIS coil's performance during quench scenarios, offering valuable insights for enhancing the safety and reliability of MRI systems under various operational conditions.

Furthermore, the research extends to the characterization of power diodes operating at cryogenic temperatures, essential for their application in MRI systems. Detailed analysis of the V-I characteristics of power diodes, including HFR 120 and BYV 28–200, revealed significant behavioral changes at cryogenic temperatures (77 K and 4.2 K) compared to room temperature

In summary, this thesis provides a rigorous and detailed exploration of the development, optimization, and testing of essential components for a 1.5 T MRI magnet.

## LIST OF PUBLICATIONS

- a) Nandawadekar, A., Singh, M. and Kar, S., 2023, “Study of power diodes used for MRI applications,” *J. Power Electronics*, vol. 24, pp.316-323, doi.org/10.1007/s43236-023-00728-7
- b) Nandawadekar, A., Singh, M. and Kar, S., 2023, “A versatile 4 K insert for characterization of the superconducting joints,” *Rev. Sci. Instrumentation*, American institute of Physics, vol. 94(10):105108, doi: 10.1063/5.0161148.
- c) Ajit Nandawadekar, Soumen Kar, et al., 2021, “Thermal and Electrical Behaviour of the Persistent current Switch for a Whole-Body Superconducting MRI Magnet,” *IEEE Transactions on Applied Superconductivity*, vol. 31, no. 5, pp. 1-5, doi: 10.1109/TASC.2021.3076748
- d) Ajit Nandawadekar, Soumen Kar, et al., 2024, “Switching performance analysis of the Persistent Current Switch,” *Journal of superconductivity and novel magnetism*, Under review.

## CONFERENCE PRESENTATIONS

- e) The Applied Superconductivity Conference (ASC), 2020.
- f) International Forum on Applied Superconductivity and Magnetism (IFASM), Australia, 2022.
- g) National Conference on Cryogenics and Superconductivity (NCCS-28), IIT Kharagpur, 2022.
- h) Power India International Conference (PIICON), NIT Delhi, 2022.
- i) International Conference on Superconductivity and Magnetism (ICSM), Turkey, 2024.



## TABLE OF CONTENTS

Abstract .....	ix
List of Publications .....	xi
Conference Presentations .....	xi
Table of Contents .....	xiii
List of Figures .....	xvii
List of Tables.....	xxvii
List of Symbols, Abbreviations and Nomenclature .....	xxix
<b>Chapter 1 INTRODUCTION .....</b>	<b>1</b>
1.1 Background of the Thesis .....	1
1.2 Magnetic Resonance Imaging .....	3
1.3 Principle of MRI Imaging .....	6
1.4 Requirements of MRI Magnet.....	9
1.5 Stringent Requirements of MRI Magnet .....	15
1.6 The necessity of superconducting magnets in 1.5 T MRI systems .....	17
1.7 Importance of homogeneity and stability: Imaging point of view .....	19
1.8 Magnet specifications .....	20
1.9 Summary.....	21
<b>Chapter 2 LITERATURE REVIEW.....</b>	<b>22</b>
2.1 Introduction .....	22
2.2 MRI technology .....	23
2.3 Superconducting joints .....	25
2.4 Persistent current switch.....	30
2.5 External interference screening .....	35
2.6 Research gap.....	36
2.7 Research objectives .....	39
<b>Chapter 3 SUPERCONDUCTING JOINTS.....</b>	<b>41</b>
3.1 Introduction .....	41
3.2 Superconducting MRI magnet.....	43

3.3	Superconducting joints .....	45
3.4	Superconducting joint making methods and architectures: .....	46
3.5	Superconducting solders .....	51
3.6	Conductor used for MRI magnet winding .....	53
3.7	Superconducting joint making using solder matrix replacement method .	54
3.8	Procedure for building superconducting joints .....	58
3.9	Characterization of superconducting joint .....	63
3.10	Joint resistance measurement principle .....	64
3.11	Experimental test rig .....	65
3.12	Joint sample .....	75
3.13	Measurement process .....	76
3.14	Results and discussion .....	77
3.15	Characterization techniques .....	81
3.16	Summary .....	88
Chapter 4	PERSISTANT CURRENT SWITCH .....	89
4.1	Introduction .....	89
4.2	Operation of a PCS .....	90
4.3	Issues with the PCS .....	92
4.4	Design of the PCS .....	95
4.5	Experimental test setup .....	100
4.6	Results and Discussion .....	102
4.7	Summary .....	119
Chapter 5	EXTERNAL INTERFERENCE SCREENING COIL .....	120
5.1	Introduction .....	120
5.2	External magnetic interference .....	122
5.3	Working principle of EIS coil .....	124
5.4	Design of EIS coil .....	124
5.5	Design parameters .....	128
5.5.1	Number of turns calculation .....	128

5.5.2 Geometrical factor .....	129
5.5.3 Self-inductance .....	129
5.5.4 Coupling factor between main and screening coil .....	130
5.5.6 Screening factor .....	132
5.5.7 Homogeneity of EIS coil .....	132
5.6 Configuration of 1.5 T magnet .....	133
5.7 Configuration of EIS coil .....	133
5.8 Design of EIS coil .....	135
5.9 Different EIS coil configurations and screening factor calculations .....	137
5.10 Result analysis of EIS coil .....	141
5.11 Induced current during quench .....	149
5.12 Design and experimental test setup of the PCS .....	151
5.13 Summary .....	154
Chapter 6 EIS BYPASS DIODES .....	156
6.1 Introduction .....	156
6.2 EIS bypass diodes .....	157
6.3 Diode parameters .....	158
6.4 EIS PCS diode assembly .....	160
6.5 Forward voltage test .....	160
6.6 Results and discussion .....	164
6.7 Summary .....	169
Chapter 7 CONCLUSION, FUTURE SCOPE AND SOCIAL IMPACT .....	170
References .....	174





## LIST OF FIGURES

Figure 1.1 Precession of Proton in the presence of magnetic field.....	5
Figure 1.2 A conceptual cutaway view of an MRI Scanner consisting of various elements of an MRI scanner including a patient. [4] .....	9
Figure 1.3 The coil structure of an MRI magnet consists of three pairs of main coils and one pair of large shield coils which minimize the stray field outside the magnet. ....	10
Figure 1.4 The schematic representation of different cross-sectional layers of the MRI magnet.....	11
Figure 1.5 A set of X, Y, and Z gradient coils are installed inside the room-temperature bore of the magnet. Z coils are circular coils and Y & X coils are saddle-shaped. [5] .....	12
Figure 1.6 Z Gradient field increases from foot to head and so does the Larmor frequency. The signals are recorded from protons located in different parts of the body and the image is constructed. [6].....	12
Figure 1.7 The three types of RF coils (body, head, and surface) that are the antennae for transmitting pulses and receiving signals from the patient’s body. [7].....	13
Figure 1.8 Cryostat structure of cylindrical MRI magnet. [8]. ....	14
Figure 1.9 The 1.5 T superconducting magnet of IUAC. ....	20
Figure 3.1 Schematic of a PCS used for the persistent mode of operation of an MRI magnet.....	42
Figure 3.2 Simplified schematic of superconducting coils having inter-coil joints (J1-J7) and joints between coil and PCS (J8-J9).....	44

Figure 3.3 Actively shielded cylindrical MRI magnet configuration. The curved blue line in the circle represents 1 ppm uniformity.....	44
Figure 3.4 The simplified representation of the cold-press joint process. [95].....	48
Figure 3.5 Schematic of typical NbTi spot welded joint with NbTi filaments spot welded to a Nb-NbTi foil. The filaments of each wire can be twisted prior to spot welding if desired for ease of handling. [50, 97] .....	49
Figure 3.6 Binary phase diagram of the PbBi system. [102, 90] .....	51
Figure 3.7 (a) WIC conductor (b) Cross section of the WIC conductor. (c) NbTi Filaments. ....	53
Figure 3.8 A schematic of the Thornton matrix replacement method. [90].....	54
Figure 3.9 superconducting joint-making setup with argon hood and solder bath. ...	56
Figure 3.10 (a) A photograph of the spiral joint and (b) a photograph of the straight joint.....	57
Figure 3.11 PbBi solder bath without glass tube (b) PbBi solder bath with glass tube. ....	57
Figure 3.12 The EDS analysis of the PbBi solder.....	59
Figure 3.13 The EDS analysis of the Tin solder. ....	59
Figure 3.14 Joint-making station with argon hood.....	61
Figure 3.15 A photograph of the PbBi and Tin solder baths.....	61
Figure 3.16 Flow chart for WIC-WIC joint. ....	62
Figure 3.17 Flow chart for WIC to PCS joint. ....	63
Figure 3.18 Schematic representation of basic components of the 4 K insert. ....	65

Figure 3.19 (a) Photograph of the partial section of the 4K insert, (b) the 3D model of the 4K insert, and (c), the insert mounted into the 4K dewar. ....	67
Figure 3.20 (a) The photograph of the superconducting primary coil, (b) the dimensional schematic of the superconducting primary and the secondary coil, and, (c) the photograph of the superconducting secondary coil i.e. tests coil of the 4 K insert. ....	68
Figure 3.21 Schematic representation of the configuration of (a) a single straight joint between two ends of the secondary coil or the test coil, (b) two straight joints between two pairs of ends of two different conductors, and, (c) spiral joint between two ends of a single conductor of the secondary coil.....	70
Figure 3.22 (a) The 3D model of the 4K insert along with the relative position of the 1.5 T solenoid magnet with respect to the secondary coil and, (b) the axial field profile of the 1.5 T solenoid magnet of the 4K insert, (c) the photograph of the sample joint having straight configuration. ....	71
Figure 3.23 The photograph of the top lid of the helium dewar with the 4 K insert. ....	73
Figure 3.24 The photograph of the test rig for the measurement of the joint resistance using a 4 K insert probe. ....	75
Figure 3.25 The schematic representation of the major steps for the measurement of the joint resistance using a 4 K insert probe. ....	77
Figure 3.26 The variation of the magnetic field with the time during the process of current induction into the secondary coil using the 4 K insert.....	78
Figure 3.27 The long-term measurement of the decay of the secondary field using the 4K insert.....	80
Figure 3.28 The steady-state values of the joint resistance were calculated from the field decay at various background fields using the 4 K insert. ....	80
Figure 3.29 SEM image of the failed WIC to PCS wire joint.....	81

Figure 3.30 SEM image of the failed WIC to WIC wire joint. ....	82
Figure 3.31 SEM image of the failed WIC to PCS wire joint. ....	83
Figure 3.32 SEM image of the successful WIC to PCS wire joint. ....	83
Figure 3.33 SEM image of the failed WIC to PCS wire joint. ....	85
Figure 3.34 SEM image of the failed WIC to WIC wire joint. ....	86
Figure 3.35. SEM image of the successful WIC to WIC wire joint. ....	86
Figure 3.36 SEM image of the successful WIC to PCS wire joint. ....	87
Figure 4.1 Persistent mode operation of MRI magnet .....	91
Figure 4.2 Algorithm for the operation of the PCS and power supply. ....	92
Figure 4.3 The critical current curve of the multi-strand CuNi-NbTi conductor [Bruker OST] [116]. ....	95
Figure 4.4 The equivalent resistance diagram of the six-strands CuNi-NbTi conductor where $R_{stand}$ is the normal resistance of each strand. ....	96
Figure 4.5 The length of the PCS wire vs the ratio of the energy loss. ....	98
Figure 4.6 The prototype PCS developed for the 1.5T MRI magnet. ....	99
Figure 4.7 (a) A simplified electrical schematic of the superconducting magnet with the PCS and, (b) the schematic of the measurement test setup. ....	100
Figure 4.8 (a) The 4K rig for testing the PCS and, (b) the schematic representation of the 4 K rig used for the thermal and electrical characterization of the PCS. ....	101
Figure 4.9 Normal resistance of the PCS for different heater currents. ....	103
Figure 4.10 PCS temperature with respect to different currents. ....	104

Figure 4.11 The total dissipation of heat in the PCS during the ramp-up of the magnet with the different heater currents through the FH1.....	105
Figure 4.12 The total dissipation of heat in the PCS during the ramp-up of the magnet with the different heater currents through the FH2.....	105
Figure 4.13 The temperature and voltage profile of the PCS with 100mA of current through the FH1 heater and 250 mA through the PCS. ....	106
Figure 4.14 The temperature and voltage profile of the PCS with 100mA of current through the FH2 heater and 250 mA through the PCS. ....	106
Figure 4.15 The temperature and voltage profile of the PCS with 100mA of current through the FH1  FH2 heater and 250 mA through the PCS.....	108
Figure 4.16 The temperature and voltage profile of the PCS with 200mA of current through the FH1 heater and 250 mA through the PCS. ....	108
Figure 4.17 The temperature and voltage profile of the PCS with 200mA of current through the FH2 heater and 250 mA through the PCS. ....	109
Figure 4.18 The temperature and voltage profile of the PCS with 200mA of current through the FH1  FH2 heater and 250 mA through the PCS.....	110
Fig. 4.19 (a) The temperature and the voltage profile of the PCS (a) with 250 mA of current through the FH1 heater and 250mA of current through the PCS at the resistive state and, (b) with 250 mA of current through the heater FH2 and 250 mA of current through the PCS at its resistive state. (c) with 250 mA of current through the heaters FH1  FH2 and 250 mA of current through the PCS at its resistive state.....	112
Figure 4.20 The temperature and voltage profile of the PCS with 350mA of current through the FH1 heater and 250 mA through the PCS. ....	113
Figure 4.21 The temperature and voltage profile of the PCS with 350mA of current through the FH2 heater and 250 mA through the PCS. ....	114

Figure 4.22 The temperature and voltage profile of the PCS with 350mA of current through the FH1  FH2 heater and 250 mA through the PCS.....	115
Figure 4.23 The temperature and voltage profile of the PCS with 500mA of current through the FH1 heater and 250 mA through the PCS. ....	116
Figure 4.24 The temperature and voltage profile of the PCS with 500mA of current through the FH2 heater and 250 mA through the PCS .....	117
Figure 4.25 The temperature and voltage profile of the PCS with 500mA of current through the FH1  FH2 heater and 250 mA through the PCS.....	117
Figure 4.26 The estimated energy dissipation on PCS at various normal resistance during ramping of the MRI magnet.....	118
Figure 5.1 Fluctuation in the magnetic field in the environment outside the MRI.[77-78].....	123
Figure 5.2 Fluctuation in magnetic field in the environment of Accelerator laboratory CERN, Geneva as measured using a fluxgate magnetometer and a detection bandwidth of 0.01 Hz.[77] .....	123
Figure 5.3 Schematic of EIS coils with main coils. ....	124
Figure 5.4 The schematic representation of the axial and radial position of one of the EIS coils relative to its associated magnet coil. Due to the axis symmetry configuration, one-half of the EIS coil and the associated magnet coil have been shown. ....	135
Figure 5.5 (a) Homogeneity in the FOV. (b) Homogeneity of the main magnet.....	136
Figure 5.6 The position of the EIS coil concerning the main magnet.....	138
Figure 5.7 (a) Homogeneity of magnet and EIS coil in 45 cm FOV. (b) The homogeneity of magnet and EIS coil in 45 cm FOV for different induced currents. ....	139

Figure 5.8 (a) Homogeneity of magnet and EIS coil in 45 cm FOV. (b) The homogeneity of the magnet and EIS coil in 45 cm FOV for different induced currents. .....	141
Figure 5.9 The simplified electrical scheme of the EIS coil and the magnet.....	142
Figure 5.10 The geometrical factor of the EIS coil for each with radial separation of 5 mm, 10mm, and 20 mm between the EIS coil and the associated magnet coil. ....	143
Figure 5.11 The peak-to-peak homogeneity in the FOV of 45 cm at the iso-center of the magnet with the induced current up to 5 A in the EIS coil with radial separation of 5 mm between the EIS coil and the associated magnet coil. ....	145
Figure 5.12 The mutual inductance between the EIS coil and the magnet coil for all four cases (Case-1 to Case-4) with the radial separation of 5 mm, 10 mm, and 20 mm between them. ....	146
Figure 5.13 The coupling factor between the EIS coil and the magnet coil for all four cases (Case-1 to Case-4) with the radial separation of 5 mm, 10 mm, and 20 mm between them. ....	147
Figure 5.14 The screening factor (in %) of the EIS coil in each case (Case-1 to Case-4) with the radial separation of 5 mm, 10 mm, and 20 mm between the EIS coil and the corresponding magnet coil. ....	148
Figure 5.15 The quench-induced eddy current in the EIS coil of all cases (Case-1 to Case-4) in correlation with the magnet's current decay when the EIS coil's PCS is at normal state (quench during ramping up of the MRI magnet).....	150
Figure 5.16 The quench-induced eddy current in the EIS coils of all four cases (Case-1 to Case-4) during persistent operation of the MRI magnet (EIS circuit is in a superconducting state).....	151
Figure 5.17 The PCS mounted onto the 1.5 T MRI magnet. ....	152

Figure 5.18 The schematic diagram of the setup for testing the PCS of the EIS circuit. .....	153
Figure 5.19 The PCS's temperature and voltage profile with 100 mA of current through the FH1 and 250 mA current through the PCS. ....	153
Figure 5.22 The temperature and the voltage profile of the PCS with 250 mA of current through the FH1 and 250 mA of current through the PCS.....	154
Figure 6.1 Simplified electrical scheme of the magnet circuit and the EIS circuit of an MRI magnet.....	158
Figure 6.2 (a) Vishay diodes: (a) standard recovery diode (stud version) 70 HFR 120 [122]; (b) Ultrafast avalanche sinter glass diode BYV 28-200 [123]. ....	159
Figure 6.3 The back-to-back diode assembly of EIS circuit. ....	160
Figure 6.4 Simple electrical circuit diagram for the V-I characterization of the diodes. .....	161
Figure 6.5 Photograph of the experimental test set up for the V-I characterization of diodes at room temperature (300 K). ....	161
Figure 6.6 Photograph of the experimental test set up for the V-I characterization of diodes at 77 K.....	162
Figure 6.7 Mounting configurations for two diodes on a fixture. ....	162
Figure 6.8 (a) Photograph of the 4.2 K test probe for the diodes; (b) V-I characterization test setup of the diodes at the temperature of LHe (4.2 K). ....	163
Figure 6.9 Test setup of the PCS diode assembly at room temperature (300 K). ....	164
Figure 6.10 Forward characteristics of HFR 120 and BYV 28-200 diodes at 300 K. .....	166
Figure 6.11 Forward characteristics of HFR 120 and BYV 28-200 diodes at 77 K.	166



Figure 6.12 Forward characteristics of HFR 120 and BYV 28-200 diodes at 4.2 K. .....	167
Figure 6.13 Forward characteristics of the back-to-back diode assembly of the PCS at 300 K.....	167
Figure 6.14 Forward characteristics of the back-to-back diode assembly of the PCS assembly at 77 K.....	168



## LIST OF TABLES

Table 1.1 Gyromagnetic ratios of some nuclei. ....	4
Table 1.2 General specifications of the 1.5 T MRI magnet. ....	21
Table 3.1 Lead-based solder materials. [90] .....	52
Table 3.3 EDX analysis of PbBi solder. ....	59
Table 3.4 EDX analysis of Tin Solder. ....	59
Table 3.5 Parameters of the primary coil. ....	68
Table 3.6 Parameters of the secondary coil. ....	69
Table 3.7 Parameters of the superconducting magnet. ....	70
Table 3.8 Heat inleak to 4.2K through the 4K insert. ....	74
Table 3.9 Parameters of the two sets of measurement. ....	79
Table 3.10 Details of the material present in the WIC to PCS joint. ....	86
Table 3.11 Details of the material present in the WIC to WIC joint. ....	86
Table 3.12 Details of the material present in the WIC to WIC joint. ....	87
Table 3.13 Details of the material present in the WIC to PCS joint. ....	87
Table 4.1 Design parameters of the PCS. ....	99
Table 5.1 The parameters of the whole-body 1.5 T MRI magnet. ....	133
Table 5.2 Main magnet Configuration. ....	136
Table 5.3 Main magnet parameters. ....	136
Table 5.4 EIS coil parameters. ....	139

Table 5.5 The parameters of the EIS coil for case I. ....	139
Table 5.6 EIS coil parameters. ....	140
Table 5.7 EIS Coil parameter for Case II. ....	140
Table 5.8 The turns ratio between the EIS coil ( $N_s$ ) and the corresponding magnet coil ( $N_c$ ) for the Case-1 to Case-4. ....	142
Table 5.9 Design parameters of the PCS. ....	152
Table 6.1 BYV 28-200 diode parameters. ....	159

## LIST OF SYMBOLS, ABBREVIATIONS AND NOMENCLATURE

- MRI – Magnetic Resonance Imaging
- NMR – Nuclear Magnetic Resonance
- $\omega$  – Larmour frequency (Hz)
- $\gamma$  – proton gyromagnetic ratio (Hz/T)
- $B_z$  – Magnetic field on the Z axis (T)
- $T_C$  – Critical temperature (K)
- $B_C$  – Critical field (T)
- $J_C$  – Critical current density (A/m<sup>2</sup>)
- $B_{max}$  – Maximum magnetic field (T)
- SMES – Superconducting Magnetic Energy Storage
- $B_0$  – Background magnetic field, field strength, centre magnetic field (T)
- L – Inductance (H)
- I – Current (A)
- J – Current Density (A/m<sup>2</sup>)
- ppm – Parts Per million
- NbTi – Niobium Titanium
- PbBi – Lead Bismuth
- FEA – Finate element method
- CT – Computer tomography
- SEM – Scanning Electron Microscopy
- EDX – Energy- Dispersive X-ray Spectroscopy
- RF – Radio Frequency
- FOV – Field of View
- MICE – International Muon Ionization Cooling Experiment
- QPS – Quench protection systems
- $B_x, B_y, B_z$  – Components of the magnetic field vector (T)
- $\mu_0$  – permeability constant ( $4\pi \times 10^{-7}$ )
- t – Temperature (K)



## CHAPTER 1

### INTRODUCTION

#### 1.1 Background of the Thesis

Magnetic resonance imaging (MRI) has emerged as a pivotal diagnostic tool for identifying critical injuries and diseases. By 2010, approximately 30,000 MRI systems had been installed globally, with an additional 3,000 systems being installed annually, reflecting a consistent 10% annual growth rate in usage. This surge in demand is further evidenced by an estimated half a million scans conducted daily worldwide, underscoring the importance of MRI technology in modern medicine. MRI uses a strong magnetic field and radio waves to generate images of the body that can't be seen well using X-rays or CT scans, i.e. it enables the view inside a joint or ligament to be seen, rather than just the outside. A superconducting solenoid magnet is the heart of any whole-body clinical MRI scanner which needs a very high spatial homogeneity along with the field stability better than 0.1 ppm/hr [1,2]. The spatial homogeneity and field stability are the two most crucial factors in MRI system performance, essential for high-quality imaging.

This thesis delves deeply into the application of superconducting technology to improve these parameters within clinical MRI systems. It is structured into six distinct chapters, each addressing critical aspects of the research endeavor. These chapters encompass a range of topics, from the fundamental principles of MRI imaging and its integration into MRI technology to the practical challenges and solutions in achieving optimal field stability and homogeneity. Through this comprehensive exploration, the thesis aims to advance the understanding and implementation of superconducting technology in enhancing MRI system performance, ultimately contributing to more accurate and reliable diagnostic imaging.

Chapter 2, delves into the foundational understanding of external interference screening (EIS), persistent current switch (PCS), and superconducting joints through an exhaustive literature survey, culminating in the formulation of the problem statement.

Chapter 3, focuses on the development of inter-coil superconducting joints, where a specialized technique is developed to make those joints and characterized for its current carrying capacity and electrical characteristics under varying magnetic fields. The chapter also introduces a novel test setup to accurately measure the ‘superconducting joints’ extremely low electrical resistance.

Chapter 4, the design and fabrication of persistent current switches (PCS) take center stage. Detailed testing is conducted to assess their current carrying capacity and transition characteristics, alongside thermal and electrical analyses aimed at optimizing switching performance.

Chapter 5, shifts the focus towards designing an efficient superconducting external interference coil (EIS) system for whole-body 1.5T clinical MRI magnets. Through finite element analysis (FEA) simulations and analytical calculations, parameters like mutual coupling, radial gap, homogeneity, and screening factors are optimized to enhance coil efficiency.



Chapter 6, explores the various diodes utilized for PCS protection, providing a detailed summary of the test setups employed and the results of diode testing at different temperatures.

Finally, Chapter 7 offers a comprehensive summary of research findings, along with insightful recommendations for process improvement. Conclusions drawn from the preceding chapters are synthesized into a cohesive report, accompanied by a delineation of future research avenues.

Collectively, this thesis endeavors to advance the understanding and application of superconducting technology in augmenting the functionality of Superconducting joints, PCS, and EIS coils within clinical MRI systems.

## **1.2 Magnetic Resonance Imaging**

Nuclear magnetic resonance (NMR), discovered by Bloch and Purcell in 1946, has emerged as a powerful technique in chemistry and physics, offering rich insights into atomic properties and interactions. The NMR signal, characterized by parameters like initial strength, frequency of oscillation, and rate of recovery and decay, provides valuable information about atomic populations and their surrounding environment.

In recent years, NMR has been extended to the *in vivo* study of human anatomy, facilitated by advancements in signal excitation and spatial mapping techniques. By leveraging the differential decay and recovery characteristics of proton NMR signals, magnetic resonance imaging (MRI) has become a preferred modality for diagnostic imaging of the head, spine, and joints. Ongoing developments aimed at improving image quality, acquisition speed, and quantitative accuracy continue to expand the clinical applications of MRI.

Originally invented in the early 1970s, MRI gained commercial traction about a decade later, gradually replacing invasive diagnostic procedures with non-invasive alternatives. Magnetic Resonance Imaging (MRI) uses a strong magnetic field and radio waves to generate images of the body that can't be seen well-using X-rays or CT scans, i.e. it enables the view inside a joint or ligament to be seen, rather than just the outside. Commonly used to examine internal body structures to diagnose strokes, tumours, spinal cord injuries, aneurysms and brain function.

As we know, the human body cell is mostly of water (70%), and each water molecule contains a hydrogen nucleus (proton) which becomes aligned in a magnetic field. An MRI scanner uses a strong magnetic field to align the proton 'spins', a radio frequency is then applied which causes the protons to 'flip' their spins before returning to their original alignment.

Protons in the different body tissues return to their normal spins at different rates so the MRI can distinguish between various types of tissue and identify any abnormalities. How the molecules 'flip' and return to their normal spin alignment are recorded and processed into an image. MRI doesn't use ionising radiation and is increasingly being used during pregnancy with no side effects on the unborn child reported.

- Nuclear Spin

In MRI, nuclear spin refers to the intrinsic angular momentum of atomic nuclei. This property is crucial for MRI because it allows nuclei to interact with magnetic fields. There are various nuclei that are important in MRI imaging, the list of various nuclei is given in Table 1.1 below.

Table 1.1 Gyromagnetic ratios of some nuclei.

<b>Nucleus</b>	<b>H<sup>1</sup></b>	<b>C<sup>13</sup></b>	<b>F<sup>19</sup></b>	<b>N<sup>23</sup></b>	<b>P<sup>31</sup></b>
Gyromagnetic ratio ( $\gamma$ )	42.58	10.71	40.08	11.27	17.25

However, most anatomical MRI focuses on protons, primarily because the hydrogen nucleus, consisting of a single proton, behaves like a simple magnet and is naturally abundant in the human body. Since the human body is composed of about 70% water, and each water molecule contains two hydrogen atoms, there is a vast number of protons available for MRI imaging. Each proton has a quantum mechanical property called spin, which makes it behave like a tiny magnet with a magnetic moment which is shown in Fig.1.1[3].

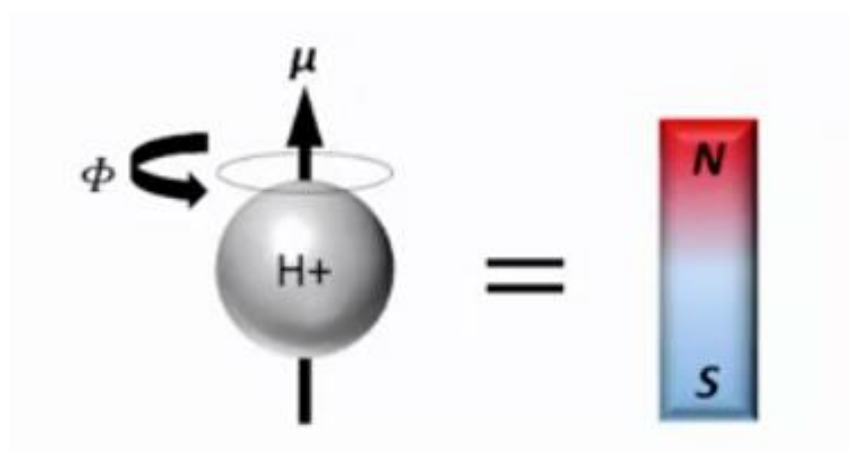


Figure 1.1 Precession of Proton in the presence of magnetic field.

- Gyromagnetic Ratio:

The gyromagnetic ratio ( $\gamma$ ) is a proportionality constant that relates the magnetic moment ( $\mu$ ) of a nucleus to its angular momentum ( $J$ ). For protons, this relationship is given by the Eq. (1.1):

$$\mu = \gamma \times J \quad (1.1)$$

Both  $\mu$  and  $J$  are vector quantities, meaning they have both magnitude and direction. The gyromagnetic ratio is specific to each type of nucleus and is a key factor in determining the Larmor frequency, which is the frequency at which nuclei precess in a magnetic field.

- Larmor Frequency:

The Larmor frequency is the frequency at which the magnetic moments of the nuclei precess around the direction of the applied magnetic field. It is given by:

$$\omega_0 = \gamma \times B_0 \quad (1.2)$$

Where  $B_0$  is the strength of the magnetic field. For hydrogen protons, the gyromagnetic ratio ( $\gamma$ ) is approximately 42.58 MHz/Tesla. Thus, in a 1.5 T MRI scanner, the Larmor frequency would be:

$$\omega_0 = 42.58 \times 1.5 = 63.87 \text{ MHz} \quad (1.3)$$

### 1.3 Principle of MRI Imaging

MRI works by exploiting the magnetic properties of hydrogen nuclei in the body, using nuclear magnetic resonance (NMR) to produce detailed images of human body tissues. The process of scanning begins with the patient being placed inside the MRI machine, where a strong magnetic field, typically ranging from 1.5 to 3 T, aligns the magnetic moments of the protons either parallel (low energy state) or antiparallel (high energy state) to the field. This alignment creates a net magnetization in the direction of the magnetic field because slightly more protons occupy the lower energy state. This phenomenon is described by the “Zeeman Effect”.

An RF (radio frequency) pulse is then applied perpendicular to the magnetic field using RF coils. This pulse is tuned to the Larmor frequency specific to the hydrogen protons, causing them to absorb energy and tip over, usually by 90 degrees, from their alignment with the magnetic field. This disrupts the net magnetization, causing the protons to precess (wobble) around the magnetic field axis. Once the RF pulse is turned off, the protons begin to relax back to their original alignment, emitting RF signals as they do so. This process, known as free induction decay (FID), is the core of the signal generation in MRI.

To convert these signals into spatially resolved images, MRI machines use gradient coils to produce small, varying magnetic fields along different spatial axes (x, y, and z). This spatial encoding allows the MRI system to determine the location of the precessing protons. The first step in this encoding process is slice selection, where a gradient field is applied along one axis to select a specific slice of the body by exciting only protons within that slice at a specific Larmor frequency. Next, phase encoding gradients are applied, which vary along one direction within the selected slice, causing the protons to acquire different phases depending on their position. Finally, frequency encoding gradients (readout gradients) are applied while the signal is being measured, causing the precession frequencies of the protons to vary linearly with their position along another axis.

The resulting signals, containing spatial information, are collected by receiver coils and stored as raw data in a format known as K-space. These data represent the spatial frequencies of the imaged object. Through mathematical processing, specifically the Fourier transform, the data from k-space are converted into spatial domain images. This transformation allows the creation of detailed images of the body's internal structures.

Different tissues in the body relax at different rates, providing contrast in the images. The two primary types of relaxation are T1 (spin-lattice relaxation), which is the time it takes for protons to return to their equilibrium state along the magnetic field, and T2 (spin-spin relaxation), which is the time it takes for protons to lose phase coherence in the transverse plane. By adjusting the timing of the RF pulses and gradient fields, MRI can produce various imaging sequences, such as T1-weighted, T2-weighted, and proton density (PD) images, each highlighting different tissue properties and pathologies.

The field strength has to be very uniform in the imaging volume (typically the cross section of the human body, with diameter of spherical volume (DSV) around 45 to 50 cm at the centre of the magnet) and it has to be extremely stable during scan.

Hence, one of the key requirements for a whole-body MRI scanner is stringent homogeneity, typically in the range of 10 ppm peak-to-peak over a large volume of 45-50 cm DSV. Poor homogeneity will interfere with the linear gradient field and thus distorts the spatial information within the scan volume and degrade the image quality. Temporal stability of the field must at least equal to the homogeneity during the period of image acquisition.

The quality of image is directly dependent on the magnetic field strength. As the proton polarization which determines the strength of the NMR signal, increases linearly with field strength. Higher field strengths therefore enable increased signal-to-noise ratio and better image equality. This also allows shorter scan times and reducing patient discomfort. There is therefore a trend toward higher field strength scanners. Field strength of more than 1 T can only be achieved practically through the use of superconducting magnets. The limiting factor in high field MRI has always been superconducting magnet technology. The challenge for designers has been to increase the field strength achievable with a large bore magnet without sacrificing spatial homogeneity, temporal stability, or patient access and without exorbitantly increasing magnet weight, cost, and stray fields.

The first practical superconducting magnets were built in the 1960's following the discovery of NbTi alloy. It was, however, the invention of Magnetic Resonance Imaging that took superconductivity from the scientific laboratory to everyday use. MRI has transformed superconductivity from a scientific curiosity to a phenomenon that improves people's lives.

In summary, MRI imaging involves aligning proton spins in a strong magnetic field, perturbing them with an RF pulse, and detecting the resulting signals as the protons relax. Spatial encoding with gradient fields, coupled with sophisticated image reconstruction techniques, allows for the generation of detailed images of the body's internal structures, making MRI a powerful, non-invasive diagnostic tool.

## 1.4 Requirements of MRI Magnet

### A. The Magnet:

The heart of an MRI scanner is a large superconducting magnet. Fig.1.2 shows a conceptual cutaway view of an MRI Scanner consisting of various elements and the object for scan, a patient. It is seen from the figure that the magnet system consists of many sets of axisymmetric coils, each set performing a different function. For example, the two large shield coils reduce stray field, the shim coils improve the field homogeneity, main coils provide the axial field  $B_0$ , Gradient Coils allow spatial encoding of MR signal for imaging, RF Coils transmit and/or receive MR signals and EIS coils prevent distortion of the main field by moving metal objects like vehicles, escalators near the scan room.

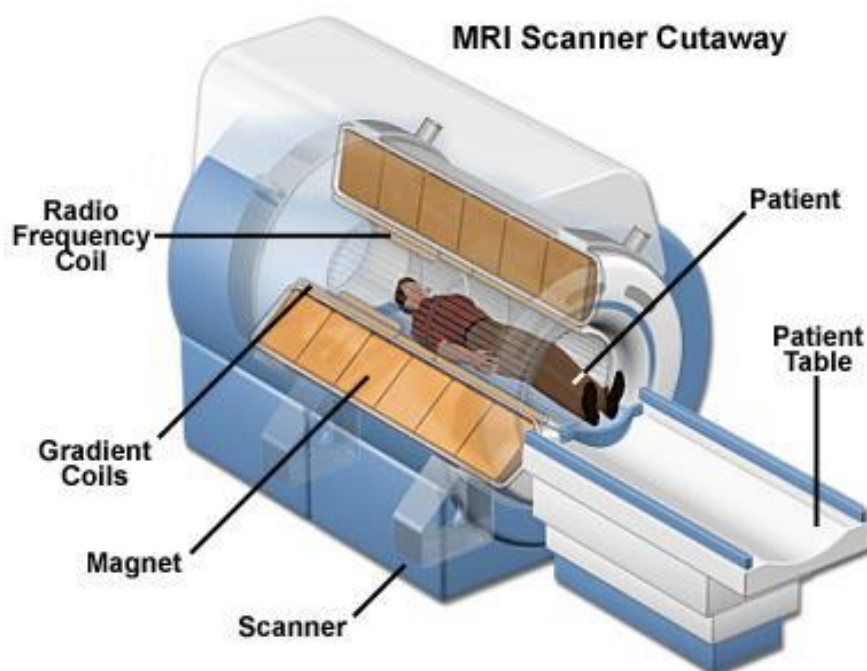


Figure 1.2 A conceptual cutaway view of an MRI Scanner consisting of various elements of an MRI scanner including a patient. [4]

A multicoil design is preferred for the main magnet over the single solenoidal design because one gets the required homogeneity of field using much smaller length

of the conductor which makes the scanner cheaper. The most popular design of the 1.5/3 T MRI magnet consists of three pairs of axis-symmetric primary coils and one pair of large shield coils with a reverse current polarity as shown in Fig.1.3. The shield coils minimize the stray field outside the magnet. The current flow through the shield coils is in a direction opposite to that in the primary coils. The shield coils generate a negative field resulting in the reduction of the stray field to below 5 G inside the imaging room to protect the sensitive electronic instruments or any person with a pacemaker. All the eight coils are however connected in series and energized by a single power supply. Fig.1.4 shows a schematic representation of the tentative configuration of different layers in the cross -section of the MRI magnet.

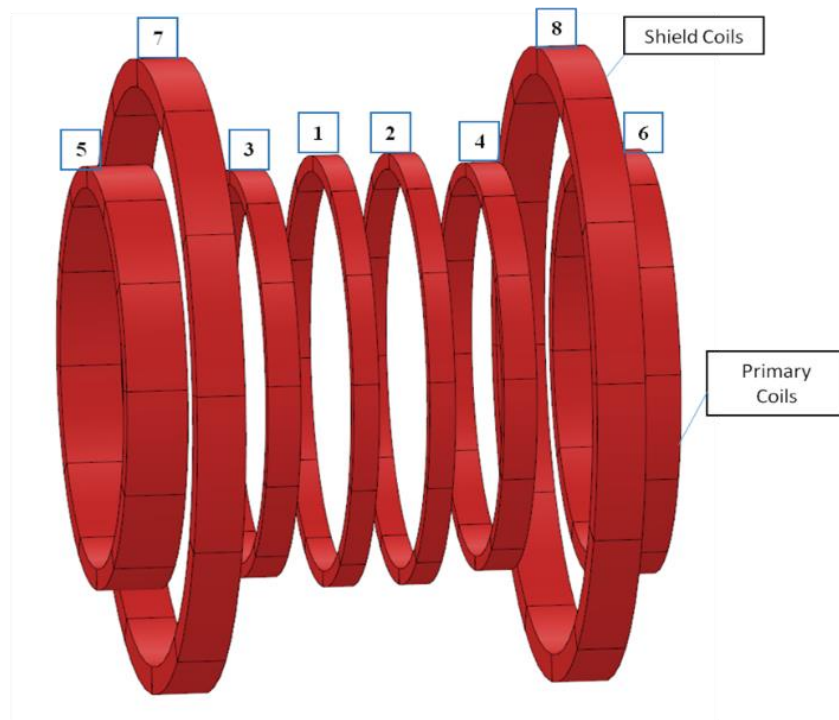


Figure 1.3 The coil structure of an MRI magnet consists of three pairs of main coils and one pair of large shield coils which minimize the stray field outside the magnet.



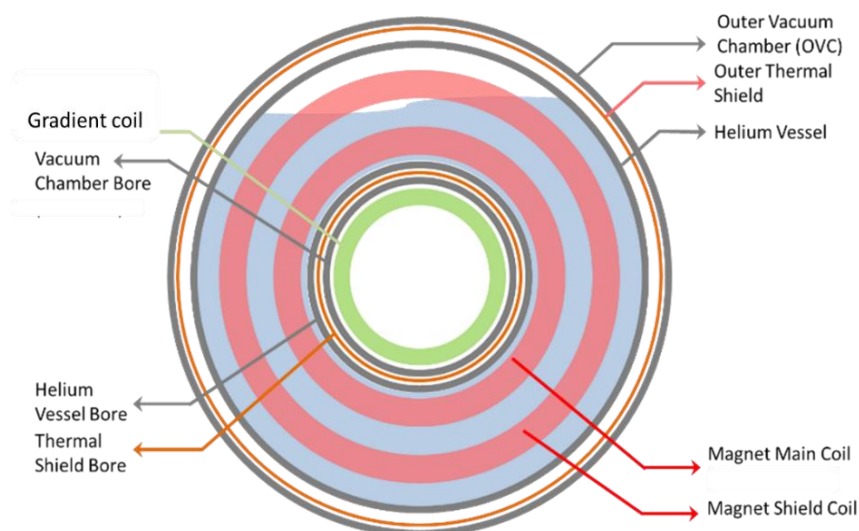


Figure 1.4 The schematic representation of different cross-sectional layers of the MRI magnet.

### **B. Gradient Coils:**

The Gradient coil is an essential component in any MRI scanner, responsible for providing spatial information, unlike other imaging modalities that rely on detector positions. They generate variable magnetic fields superimposed on the main static magnetic field ( $B_0$ ), usually aligned along the z-axis. This creates linear variations of the field and the protons acquire different resonant frequency,  $\omega L$  at different locations of the body across the field of view (FOV). The gradients are of the order of 50 mT/m and a slew rate of switching pulses up to 200 T/m/s over the FOV. The schematic of the three gradient coils is shown in Fig.1.5, how the total field on a proton increases from feet to head. The Larmor frequency, being proportional to field, too increases from feet to head. Fig.1.6 shows the drawing of the Z gradient coil and the patient position [6]. The field gradient created by these coils enables distinction between the NMR signal (Larmor frequency) from protons in one “slice” of the body (a plane perpendicular to the direction of the field) and the signal from protons in another “slice” of the body. Higher the magnetic field gradient the thinner the slices can be made which leads to greater spatial resolution. This variation causes the precession frequency of protons to become a function of spatial location, enabling spatial encoding for image formation. MRI scanners have three gradient coils for the x, y, and

z directions, which modulate the main magnetic field's strength rather than generating fields along these axes. The x and y gradient coils modulate the field strength as a function of position along their respective axes, while the z gradient coil does the same along the z-axis. This modulation creates spatially varying magnetic fields, resulting in different precession frequencies at different locations.

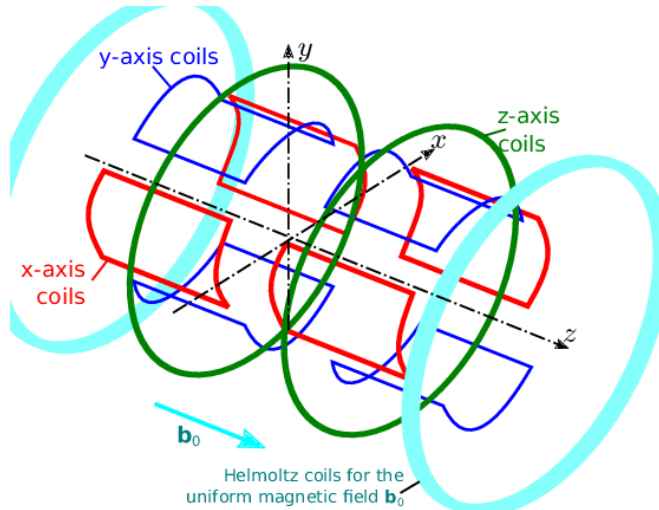


Figure 1.5 A set of X, Y, and Z gradient coils are installed inside the room-temperature bore of the magnet. Z coils are circular coils and Y & X coils are saddle-shaped. [5]

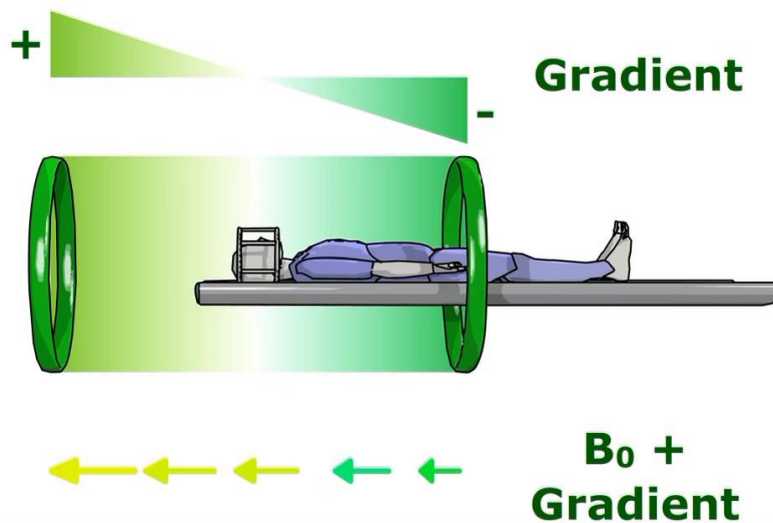


Figure 1.6 Z Gradient field increases from foot to head and so does the Larmor frequency. The signals are recorded from protons located in different parts of the body and the image is constructed. [6]

### C. RF Coils:

The RF coils are strategically positioned within the magnet assembly, situated in close proximity to the patient's body. Functioning as antennae, these coils play a vital role in both transmitting and receiving signals from the tissue during MRI scans. Various coil designs are tailored for specific anatomical regions, including body, head, and surface coils, each optimized to capture signals from their respective areas with efficiency, which is shown in Fig.1.7. While in some applications utilize the same coil for both transmitting and receiving signals, others employ separate coils for these functions, depending on the imaging requirements and desired signal quality.

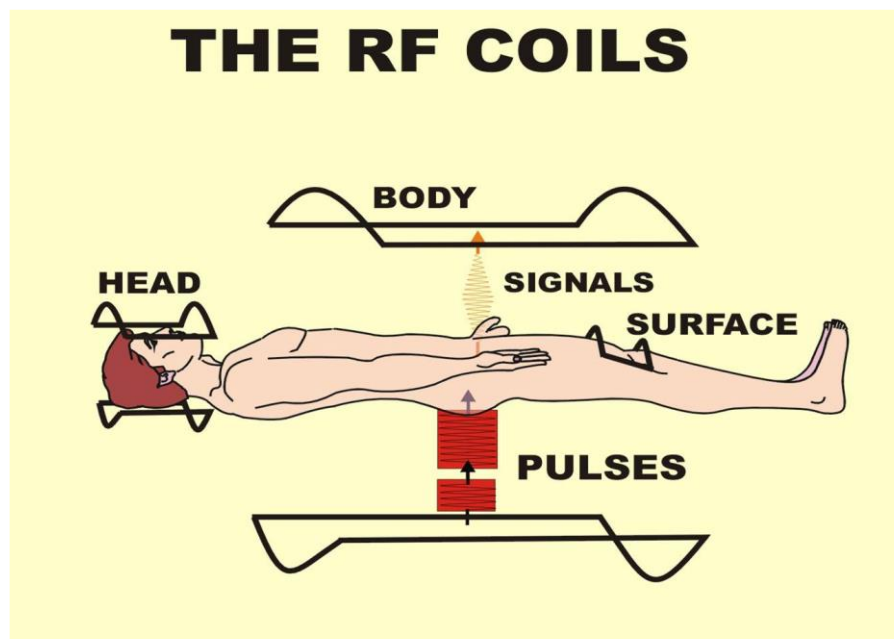


Figure 1.7 The three types of RF coils (body, head, and surface) that are the antennae for transmitting pulses and receiving signals from the patient's body. [7]

### D. Mechanical and cryogenic structure

The key components of the mechanical structure of a cylindrical MRI magnet are depicted schematically in Fig.1.8. The superconducting coil, housed within a vacuum-sealed vessel filled with liquid helium (illustrated in grey). The inner wall of this vessel

features precisely machined circumferential grooves to secure the coil sections firmly in place. This coil support must be extremely rigid to withstand the substantial magnetic forces generated between the coil sections. In some designs, this support structure is separate from the helium container.

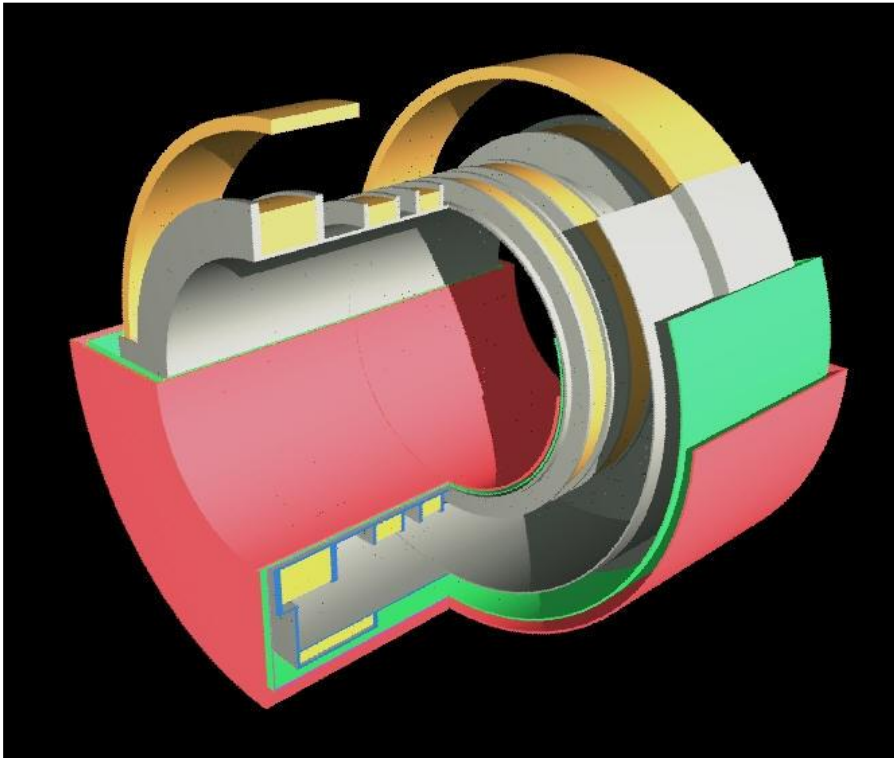


Figure 1.8 Cryostat structure of cylindrical MRI magnet. [8].

Encasing the helium vessel is another airtight enclosure known as the outer vacuum container (shown in red). This outer surface constitutes the visible exterior of the magnet. The space between the two containers is evacuated to prevent heat transfer via gas conduction. The cold mass, comprising the helium tank and coils, is supported by several thin elements typically made from glass-reinforced plastic. The primary mode of heat transfer from the outer vacuum container's warm surface to the cold mass is thermal radiation. To mitigate this heat load, one or two additional closed shells, usually made of thermally conductive materials like aluminum, are placed inside the vacuum space. When these shields are connected to the heat stations of a cryogenic

refrigerator, they capture and remove nearly all incoming radiation heat, significantly reducing the amount that reaches the cold mass.

Radiation heat transfer is further minimized by layering aluminized plastic foil (superinsulation) within the gaps. In a dual-shield system, the helium tank's heat load, which causes helium evaporation, can be reduced to about 30 mW, resulting in a helium loss of roughly one liter per day. Recently, cryogenic refrigerators capable of providing approximately 1 Watts of cooling power at 4 K have been developed. MRI manufacturers are increasingly integrating this technology to eliminate helium boil-off entirely. With these refrigerators installed, a single radiation shield suffices, allowing for reduced clearance between the vacuum space walls. This reduction can lower manufacturing costs or result in a more compact magnet design. The cryostat has to support a huge cold mass, (magnet weighing ~ 2 tons) using high strength / low thermal conductivity material rods or bars welded to the outer vacuum vessel. Detailed calculations are needed to be made and the final design of the cryostat must consider the stresses produced under extreme conditions including quench.

## 1.5 Stringent Requirements of MRI Magnet

High image quality needs stringent requirements on the performance of the superconducting magnet

- Field strength ( $B_0$ ): The scan time and image resolution are directly proportional to the field strength because of the enhanced signal-to-noise ratio (SNR) and resolution. Hence higher and higher magnetic field strength is considered despite the technical challenges.
- Imaging volume: The larger the imaging volume, the better. However, it does require a trade-off owing to the increased cost. The need for the high-performance gradient and RF-system, as well as the passive shim and covers translates a patient bore with 60 or 70 cm diameter into a typical warm bore diameter of the

primary magnet of 85-95 cm. The diameter of the maximum imaging volume (FOV) will be half of the diameter of the magnet bore.

- Field homogeneity: The greater the uniformity, the better. Homogeneity of 10 ppm peak-to-peak of the background field ( $\mathbf{B}_0$ ) within typically 45-50 cm FOV. For particular imaging procedure, the surfaces of the smaller dimension and higher homogeneities may be specified.
- Signal-to-Noise ratio (SNR): The SNR is the most important parameter defining image quality in MRI. A low SNR means that the contrast between different tissues can't be resolved.
- Long-term field stability: The MRI magnet requires long-term stability in the central field ( $\mathbf{B}_0$ ). The temporal stability should be better than 0.1 ppm/hr which is 0.09% per year. This order of stability will eliminate any further recharging of the magnet to restore the frequency in operating bandwidth. The desired order of the temporal stability is an order of magnitude better than modern high-current power supplies can provide. Hence, the commercial MRI system is operated in persistent mode.
- Short-term field stability: The induced eddy current in the magnet system by the pulsing of the gradient coil greatly affects the image quality. Hence, short-term stability needs to be taken care of during scanning.
- Stray field shielding: For any MRI scanner, one of the most critical requirements is the 5 G stray footprint in maximum 5m (axial) x 3m (radial) elliptical region for safety reason.
- Cryogenic cooling: An ideal MRI magnet system needs minimum servicing. The cryogenic system of the MRI should be completely invisible to the user. The technology of cryocooler based Helium re-condensation has made it possible to minimize the Helium re-filling frequency and makes it a zero-boil off (ZBO) system.
- Reliability: The MRI magnet system must be rugged, highly reliable, safe, and fully self-protected. All the critical parameters of the magnet need to be monitored and logged continuously to report any abnormal situation. There

should be an emergency shut-down mechanism that enables quick discharging of the magnet if necessary.

- Length: The problem of claustrophobia has always been an issue. The shorter, the better.
- Weight: One of the driving parameters for cost reduction of an MRI machine is the metallic weight of the machine. Hence the future technology is moving for lower and lower weight of the system for ease in transportation, installation in the site, etc.

## **1.6 The necessity of superconducting magnets in 1.5 T MRI systems**

Superconducting magnets are integral to 1.5 T MRI systems due to their ability to produce high magnetic fields with numerous advantages. High-field magnets, such as the 1.5 T, significantly enhance the signal-to-noise ratio, leading to superior image quality. This improved resolution allows for the better detection of small structures, such as calcifications and hemorrhages, and improves the visibility of gadolinium contrast enhancements. These enhancements are particularly crucial in life-threatening situations where detailed and accurate imaging information is essential for guiding surgeons and physicians in making informed decisions about patient care.

Using copper-based magnets to generate such high magnetic fields is impractical for several reasons. Copper conductors inherently have electrical resistance, which results in substantial power consumption. For a 1.5 T magnetic field, the power requirements would be prohibitively high for everyday clinical use. Additionally, generating a high magnetic field with copper would require either a significantly larger conductor or an increased number of turns in the coil. Both options would result in a considerably larger magnet, which is impractical for clinical settings. Furthermore, the resistive nature of copper generates a significant amount of heat, necessitating a large and complex cooling system to dissipate this heat. This additional requirement would further increase the size and complexity of the magnet, making it unsuitable for use in hospitals. Copper-based magnets also struggle to achieve the high

field homogeneity necessary for MRI, which is essential for producing clear and accurate images.

In contrast, superconducting magnets offer a more feasible solution for high-field MRI applications. Superconductors can carry much higher currents than copper conductors without any electrical resistance. This property allows superconducting magnets to generate strong magnetic fields, like 1.5 T, with a more compact and manageable magnet size suitable for clinical environments. Additionally, superconducting magnets can operate in a persistent mode, providing excellent field homogeneity and stability. This consistency is crucial for high-quality imaging and enables the use of specific pulse sequences that are not possible with resistive magnets.

The high initial fabrication and operational costs of superconducting magnets are justified by their numerous benefits. These magnets offer superior image quality, enhanced diagnostic capabilities, and the flexibility to use advanced imaging techniques. The high field homogeneity provided by superconducting magnets directly improves image quality and enables certain pulse sequences that are critical for advanced imaging but impossible with resistive magnets. These capabilities are essential for providing detailed and accurate diagnostic information, which is particularly important in critical and complex medical conditions.

Superconducting magnets have undergone rigorous scrutiny and validation before becoming a standard technology in MRI. Despite their high costs, their ability to provide superior imaging quality, stability, and homogeneity has made them indispensable in medical imaging. The use of superconducting magnets in MRI represents a significant advancement in the field, offering enhanced diagnostic capabilities that justify the investment and operational costs associated with their use. As a result, superconducting magnets are now widely accepted and utilized in MRI systems, demonstrating their critical role in advancing medical imaging technology.



## **1.7 Importance of homogeneity and stability: Imaging point of view**

Homogeneity and stability are crucial factors in magnetic resonance imaging (MRI) from an imaging perspective due to their significant impact on image quality, diagnostic accuracy, and the reliability of results. Here's why homogeneity and stability are essential:

### **1.7.1 Homogeneity:**

**Image Quality:** Homogeneous magnetic fields ensure uniformity in the resonance frequency across the imaging volume. This uniformity minimizes distortions and artifacts in the resulting images, leading to clearer and more accurate representations of anatomical structures.

**Contrast Enhancement:** Homogeneous fields improve the contrast between different tissues, allowing for better differentiation between structures with similar signal characteristics. This is especially important in identifying subtle abnormalities or pathologies.

**Spectral Resolution:** Homogeneity facilitates high spectral resolution, enabling the detection of chemical shifts and molecular compositions, which can provide additional diagnostic information.

**Spatial Encoding:** In gradient-based MRI techniques, such as diffusion-weighted imaging or functional MRI, homogeneity ensures precise spatial encoding, leading to accurate localization and mapping of physiological processes.

### **1.7.2 Stability:**

**Consistency:** Stable magnetic fields maintain consistent imaging parameters over time, ensuring reproducibility and consistency in image quality and diagnostic interpretation across multiple scans or sessions.

**Longitudinal Studies:** For longitudinal studies or follow-up examinations, stable fields are essential to track changes in tissue characteristics or disease progression accurately.

**Motion Artifacts:** Stability minimizes motion artifacts by reducing variations in magnetic field strength, which can occur due to patient movement or scanner instabilities.

**Quantitative Analysis:** Stable fields are critical for quantitative MRI techniques, such as diffusion tensor imaging or magnetic resonance spectroscopy, where accurate measurements of tissue properties rely on precise and stable magnetic field conditions.

In summary, homogeneity and stability are paramount in MRI for achieving high-quality images, accurate diagnoses, and reliable research outcomes. They ensure uniformity, consistency, and reproducibility in imaging parameters, ultimately enhancing the clinical utility and scientific value of MRI in healthcare and research.

## **1.8 Magnet specifications**

The detailed specifications of the proposed MRI magnet and zero boil-off cryostat, along with the design of the MRI system, are outlined in Table 1.2 below. Also, the proposed model of the MRI scanner of the IUAC is shown in the Fig.1.9.



Figure 1.9 The 1.5 T superconducting magnet of IUAC.

Table 1.2 General specifications of the 1.5 T MRI magnet.

<b>Parameters</b>	<b>Value</b>
Field Strength	~ 1.5 T
Peak field	4.12 T
Operation Current	~ 450 A
Imaging Volume	A 45 cm of diameter at the centre
Conductor	NbTi (T <sub>c</sub> = 9.2 K) WIC
Homogeneity	<b>± 10ppm in the Imaging Volume</b>
Field Stability	<b>0.1ppm/hr</b>
Stored Energy	3.71 MJ
Total inductance	42 H
Inner diameter of the magnet	~1.0 m
Outer diameter of the magnet	~1.8 m
Length of the magnet	~1.5 m

## 1.9 Summary

The introduction chapter covers the key components of MRI, with a focus on the magnet's critical role. It highlights the importance of magnetic field homogeneity and stability for high-quality imaging. Superconducting magnets are necessary for generating the strong, stable magnetic fields required for MRI. The chapter also discusses the stringent requirements for MRI magnets, including precise field strength and control, essential for ensuring accurate imaging and patient safety.

## CHAPTER 2

### LITERATURE REVIEW

#### 2.1 Introduction

Superconducting magnets represent the cornerstone of Magnetic Resonance Imaging (MRI), a pivotal technology in modern medical diagnostics. The journey of MRI development traces back to the 1960s when practical superconducting magnets were first realized following the discovery of NbTi alloys. This breakthrough enabled the production of high magnetic fields necessary for generating detailed images of internal body structures without ionizing radiation. Notably, the publication of the first human body images in 1977 marked a transformative moment in medical imaging, highlighting MRI's potential as a non-invasive diagnostic tool [9]. Over the decades, MRI technology has advanced significantly, largely driven by innovations in superconducting materials and magnet designs. High-temperature superconductors (HTS), explored extensively in recent literature, promise enhanced performance over

traditional NbTi alloys due to their higher critical temperatures and current densities [4, 8].

## 2.2 MRI technology

K. Pieterman and H. Postma (1984, 1986) developed a 1.5 T MRI magnet for research purposes, documenting the construction, cooling system, and instrumentation in their work [10 – 11]. Their papers provided valuable insights into the fabrication of coils, bobbins, and support structures.

The founding of Philips Healthcare in 1891 and GE Healthcare in 1994 increased market demand for more economical, lighter, and smaller MRI systems. In 1994, Y. Iwasa began large-scale academic research supported by the MRI industry, producing extensive literature on MRI magnet operation. The results were later compiled in his book [12], which, based on actual laboratory and industry magnets, thoroughly explored the design and development process, including fundamental aspects like quench protection and cryostat design.

Recent research for the International Muon Ionization Cooling Experiment (MICE) (2005-2011) explored the practical issues in designing superconducting magnets with a field range of 2-5 T and currents of 200-250 A. Key contributors Michael A. Green and Steve Virostek published detailed studies on fabrication, assembly, and alignment, highlighting how various parameters impact magnet performance [13 – 18].

The ISEULT/INUMAC Whole Body 11.7 T MRI Magnet project (2008-2017) involved a collaboration among the University of Freiburg, Siemens Healthcare, Bruker BioSpin GmbH, and CEA, France. This project, which achieved the highest magnetic field strength for an MRI magnet to date, produced extensive literature on the fabrication and winding processes [19 – 28]. The published work includes detailed

mechanical and thermal analyses, as well as a discussion of various manufacturing challenges and the solutions implemented [29].

The Institute of Electrical Engineering at the Chinese Academy of Sciences, under the leadership of Q. Wang, developed a 9.4 T high-field MRI for research purposes between 2012 and 2017, in close collaboration with domestic industries [30], [33]. This magnet was designed as a concentric solenoid rather than a split-type. The published papers focus on the stress analysis of these superconducting MRI magnets, examining the impact of various factors, such as winding tension, on the resulting operational stresses

Few researchers also published review papers in the area of MRI magnets. Y. Lvovsky and P. Jarvis (2005) of GE Healthcare presented the basic design of superconducting magnets and specific design criteria for MRI magnet design [2]. They also discussed current technologies involved and different solutions for the problems. The paper also lists the basic relation between the magnetic field and the geometry of the coils. J. Overweg (2006) of Philips Research also summarised the operation of modern MRI magnets with a brief introduction of each key technological area [34]. The paper gives an overview of the MRI magnet configurations and various ancillaries associated with MRI magnets.

Y. Lvovsky *et al.* (2013) summarised in their detailed review both non-traditional approaches and emerging trends in superconducting magnets for MRI, along with market trends and various cost reduction strategies [35]. The paper discusses the economic and market factors that drive the MRI industry and peaks into the non-traditional configurations, such as open magnets and walk-through magnets, which have emerged recently. The paper also discusses high-field magnets and advanced solutions for future MRI magnets. M. Parizh *et al.* (2017) reviewed recent advances in MRI magnet design, with specific interests in the use of HTC superconductors for MRI magnets [2]. They discussed the feasibility of new conductors that can be used for MRI magnets in terms of characteristics such as

stability, conductor shape, ease of handling, insulation, and manufacturability. They concluded that though there are feasible alternatives, new developments need to be made before they can be commercially marketed. Bruce Breneman (2019) discusses the advantages of superconductivity and provides a detailed description of MRI scanner design, highlighting the physics and applied engineering aspects crucial to optimizing MRI performance [9, 10].

### 2.3 Superconducting joints

The idea of monitoring a field generated by the induced current in a superconducting loop over an extended period to detect its variation with time is not new. Collins, using this technique, performed such a test from 16 March 1954 to 31 August 1955 to show that the current induced in a superconducting lead torus was essentially persistent [36].

In 1976, M. J. Leupold and Y. Iwasa introduced a technique for measuring superconducting joint resistance using the current decay method, developed during the construction of a 7 T NMR magnet. This approach enables the measurement of joint resistance and current-carrying capacity within just a few hours. Notably, the evaluation can be performed on joints situated in an ambient magnetic field. The total resistance of all joints was found to be less than  $10^{-12} \Omega$ . These joints were made using single-core NbTi wires, [37 – 38].

Roy F. Thornton (1986) described how to prepare superconducting joints with NbTi filamentary wire in his patent. A core problem for joining Nb-based materials is surface oxidation due to exposure to oxidizing agents (nitric acid, water, solvents, and air) during the removal of the Cu matrix. This will be the base reference for the solder matrix method of the superconducting joint. Due to the oxidation problem discussed, poor wetting reportedly prevents soldering to bare NbTi filaments, and common fluxes are unable to remedy this. Thornton's matrix replacement technique is the most commonly used method in the literature in light of this issue. Thornton found that

joints made with more Bi-rich solders (in the range of 30{55.5 wt. % Bi) had higher critical currents. This is understandable since  $J_c$  values in PbBi increase with the density of Bi interphase boundaries, as discussed in [39].

T. Tominaka, & S. Kakugawa (1991) used a radio frequency superconducting quantum interference device (R.F.-SQUID) to calculate superconducting joint resistance utilizing a voltmeter. In this technique, a sensitive voltmeter is used to measure the voltage generated across the superconducting joint. The paper also discusses superconducting joint techniques like soldered joints, spot-welded and cold-welded joints, etc. There is a qualitative difference between solder joints and other joint techniques. The current decay pattern of the other joints is qualitatively different than the solder joint. Also, the flux creeping phenomenon is present in the cold-welded and spot-welded joints. They mentioned that the initial field decay happened due to the change of the current distribution inside the superconducting multifilamentary wire. The measured resistance of the cold-welded joint was around  $10^{-14}$ , with the joint length of 20 mm in zero background field [40].

W. Wen *et al.* (1992) developed a setup for field decay measurement based on a current comparator. They noted that the current decay method, along with the SQUID voltmeter, is typically used to measure joint resistance below  $10^{-13} \Omega$  in the absence of a background field. The team prepared various joints using both the cold press method and diffusion welding, and they tested the performance of these joints in a background field of approximately 6 T, as described in reference [41].

S. Phillip *et al.* (1995) discussed the detailed procedure of spot-welding joint and crimped joint techniques to make joints of multifilamentary superconducting wire. They mentioned that a small shunt used with the joints would be used as a thermal anchor, and when the current exceeds the critical values, it will protect the joint. The joint resistance is measured in the vacuum environment. The value of joint resistance was less than a few  $n\Omega$  [42].



A fundamental study of inhomogeneous current induction and transfer in face-to-face lap joints has been carried out by S. Mizumaki & A. Yamamoto (1997). To simulate the practical situation, they used two types of superconducting wires (CuNi-NbTi, and Cu-NbTi) to prepare the face-to-face lap joint using the diffusion bonding technique. A Hall probe array was attached along the length of the diffusion-bonded multifilamentary NbTi joint, made in the termination orientation. In research, it was found that as a transport current through a joint was increased, the current penetrated further along the joint's length [43].

D. T. Ryan & H. Jones (1997) presented results of E-I characterization for a numb of samples of commercial superconducting wires from electric fields of order  $1 \mu\text{V m}^{-1}$  to  $1 \text{pV m}^{-1}$ . In addition, they mentioned that the critical current for filamentary NbTi and filamentary Nb<sub>3</sub>Sn samples measured by the four-probe method was lower than the critical current measured by the field decay method. The reason for this important comment was not mentioned in this paper [44].

Junsheng Cheng *et al.* (2012) fabricated the NbTi superconducting joints for a 400-MHz nuclear magnetic resonance (NMR) magnet system. Also, the advantages of the solder matrix replacement method and joint process using the same way are explained in detail. The overall measured resistance of the joints under the background field of 1 T is  $9.58 \times 10^{-12} \Omega$ , and the calculated inhomogeneity produced by the joints is in the range of 0.0001 ppm. They concluded that the joint position almost has no adverse effect on the homogeneity of a magnetic field [45].

Jianhua Liu *et al.* (2013) tested the electrical properties of the superconducting joints using the inductive resistance testing (IRT) method. The persistent joints between NbTi multifilamentary conductors were fabricated using the cold-pressing welding method by applying different pressures for each joint (4MPa -20 MPa). The resistances of these persistent joints are all less than  $1 \times 10^{-13} \Omega$  in a 1 T background magnetic field and can meet the requirements of most NMR and MRI magnets [46].

Jianhua Liu *et al.* (2013) The superconducting joints were fabricated using the cold pressing welding method for a 400 kHz NMR magnet. The electrical properties of the joints were measured using the IRT method. The total resistance of all joints is  $3 \times 10^{-14} \Omega$  at 120 A of current under 1 T background magnetic field. From the test, results in the author concluded that the under-zero background field current in the persistence joint circuit decreased sharply due to the flux creeping phenomenon. After a few hours, the current will slowly decay due to the thermal-assisted flux flow [47].

Siyuan Liu *et al.* (2013) fabricated and tested the superconducting joints for the 7T animal MRI magnet using the solder matrix replacement method in the open air. The electrical characteristics of the joints were tested using the IRT method. The joints fabricated using  $1.5 \times 1 \text{ mm}^2$  Nb-Ti/Cu wire achieved an  $I_c$  of 1,160 A and a resistance of  $1.5 \times 10^{-14} \Omega$  in 0.6 T at 4.2 K., and the NbTi/CuNi sample joint carries a current up to 630 A with a resistance lower than  $4 \times 10^{-14} \Omega$  under a magnetic field of 0.6 T Also, the design of the current decay measurement setup explained in detail. [48 – 49].

Brittles *et al.* (2016) enhanced field measurement sensitivity by utilizing a widely available Magnetic Properties Measurement System (MPMS) to conduct an inductive resistance testing method for measuring joint resistance. This technique is recognized as the most sensitive method suitable for low-temperature applications. The authors noted that the resistance values they measured were comparable to those obtained by other researchers who produced similarly manufactured joints and characterized them using the conventional IRT method [61]. Additionally, the paper provides a detailed review of the advancements in joint development for various types of superconductors, including NbTi, Nb<sub>3</sub>Sn, MgB<sub>2</sub>, BiSCCO, and REBCO. It also explores the different materials and solders used in creating superconducting joints [50]. The brittle thesis gives a detailed idea of different superconducting joint techniques and the SQUID loop's inductive resistance testing method. Also, Superconducting and Microstructural Properties of the superconducting joint using Microscopy [51].

In 2015, Motomune *et al.* studied current paths in Nb-Ti joints fabricated using the solder matrix replacement method. Here a total of 8 one-loop joint samples were prepared and tested. A conventional Nb-Ti wire 2.0 mm in diameter was used for making the loops. The resistances of the loops were lower than  $10^{-13} \Omega$  and independent of the composition and solidification rate in Pb-Bi. [52].

Dipak Patel *et al.* (2019) evaluated two types of Pb-Bi solder as potential candidates for Nb-Ti superconducting joints in terms of their  $J_c$  and  $T_c$ . The solders show around 2% deficiency in the composition. Also, the EDX mapping of two PbBi solders was carried out. The optimal etching time for the Cu matrix with tin (Sn) and Sn with Pb-Bi was then evaluated by scanning electron microscopy (SEM). The joints were fabricated using the solder matrix replacement method. A resistivity of  $3.25 \times 10^{-14}$  was achieved with a self-field at liquid helium temperature. They also reported that loose Cu or S.S. wire binding in the joint for improving joint performance was not favorable in terms of achieving higher joint performance [53].

Till the date there is no study has been reported in the literature on lead-free solder joints of NbTi wires. A study by S. Santra *et al.* (2019) compared the microstructural and microtextural evolution of solid NbTi and liquid InSn-based solders at the interface between solid NbTi and liquid InSn-based solders [54]. Kensuke Kobayashi *et al.* (2020) fabricated the superconducting joint and tested it at 3k temperature, which is achieved using a cryocooler. Also, the Resistances of the Nb-Ti sample that was joined using Pb-Bi solder were successfully evaluated to be in the range of  $10^{-14}$ – $10^{-13} \Omega$  at 4.2 K with sample current up to  $\sim 350$  A [55].

Weilun Tan (2020) Explained the methods for developing superconducting joints like the cold press method, ultrasonic welding method, spot welding method, and Thornton's replacement method are discussed. Also, The Different properties used for persistent joint fabrication are discussed. One of their joint in a closed loop achieved joint resistance in the range of  $10^{-14}$ – $10^{-13} \Omega$  at 4.2K with a sample current of up to 350A [56].

Feng Zhou *et al.* (2013) explained the cold pressing method of superconducting joints and the quasi-static analysis of the cold pressing process performed using the Abaqus-Explicit method. The press amount of 61%-65.5% shows smaller resistances than the other samples, which corresponds with the conclusion from the simulation [57].

Martin N. Wilson (1982), a key figure in the growth of superconducting technology, published his book on superconducting magnets [58]. His work is still considered one of the most concise and complete guides to superconductor magnet design. His book summarizes the analytical methods used for magnetic field calculation, force calculation, and stress analysis of superconducting solenoid magnets. He also lists other technologies associated with the superconducting magnet operation, such as PCS design, joint design, instrumentation, etc.

## 2.4 Persistent current switch

The PCS is a key component for superconducting magnets to operate in persistent current mode. In thermally controlled PCS, it usually takes several seconds or longer to transition from a normal state to a superconducting state or vice versa. This sharp and reversible transition of superconductor from one state to another state due to different triggering methods like thermal, current, or magnetic field-controlled triggering gives its prominent switching properties.

Hagedorn and P. Dullenkopf (1974) designed a PCS permit's switch off of current from 20-90 A within a few milliseconds with a normal resistance of about 20  $\Omega$ . R V Harrowell (1973) described a protection PCS for power system components like superconducting cables or generators. The main advantages of the PCS are: that it does not require ancillary equipment for detecting the fault and triggering the PCS, and its temperature rise during the fault is small enough to allow immediate superconduction at the end of the fault [59].

R. D. Isaac and R. B. Schwarz (1975) designed a PCS built using only common laboratory materials. The paper highlights the importance of operating superconducting solenoids in persistent mode to minimize helium consumption and enhance magnetic field stability. This is crucial for experiments involving superconducting materials, as a stable magnetic field is often required for accurate results. One of the main challenges addressed in the paper is the difficulty in building a compact and reliable persistent switch. Previous attempts may have faced issues related to size, reliability, or the materials used, which the authors aim to overcome with their design. In order to change the superconducting state of the PCS, two strain gauges were used to heat a small piece of superconducting wire. To power the heaters, a 100mA current was sufficient to maintain the superconducting loops in the normal state [60].

S. Yamamoto *et al.* (1988) give a clear idea of the transient characteristics of power diodes in cryogenic temperature and their application to the protection of PCS in superconducting magnet systems. In the case of power diodes, the forward voltage - forward current characteristics at low temperature are different from those at ordinary temperature. The characteristics depend on temperatures. At low temperature, the forward voltage drop of power diodes will be 6 times larger than the room temperature forward voltage drop. A detailed description of this change in voltage is given in this paper. Also, the author proposed three criteria for power diodes as they are applied to protect persistent current switches [61].

H. Maeda *et al.* (1991), from Toshiba R &D Centre, Japan designed two sets of PCS using 0.3mm and 0.9mm diameter conductors, and the degradations are compared between the 0.3 mm PCS and the 0.9 mm PCS. From the test results of both PCS, the author concluded that the instability of the PCS depends on conductor diameter; the thinner the conductor, the more stable the PCS is [62]. The temperature rise, due to self-field A.C. loss during ramping up the current, causes degradations. The quench current gradually decreases to the adiabatic value, if the current sweep rate is progressively increased.

T. K. K.O. *et al.* (1995) analyzed the PCS temperature characteristics quenched by applying  $I^2R$  power using heat transfer equations. Also, the optimal conditions for the design of the PCS were derived in this paper. The designed PCS was tested by applying 100A current in the persistence current mode [63, 64]. A twisted multifilament NbTi cable with a CuNi matrix was used for the PCS, and a NiCr wire was used for the heater of the PCS. The normal resistance of the PCS was around 2.8  $\Omega$ . When the heater currents were 100, 150, and 200mA in energization to 100A, the temperatures of the PCS were 8.3, 12.5, and 19 K, respectively. The optimal control current which minimized the thermal losses to quench the PCS was about 150mA.

Bijan Dom *et al.* (1995) In this paper, a PCS that allows a cryogen-free M.R. magnet to be ramped up to its designed magnetic field and parked in a persistent state has been designed built, and installed in a magnet. The PCS design criteria, which have to operate in a cryogen-free magnet, are different from those of liquid helium-cooled magnets. The ramping heat load from the PCS should be small enough such that the second stage of a cryocooler can handle it. At the same time, the PCS should be small enough such that its temperature recovery after a ramp is fast, given the small cooling capacity of the cryocoolers [65].

To know information of adiabatic method and condition to obtain designed resistance and characteristics. Rock-Kil KO *et al.* (2001) designed and tested around 5 PCS considering different design parameters. The computer simulations on the temperature distribution of PCS 1 were performed in this study with the help of ANSYS to verify whether the superconducting part was superconductive or not. Also, they mentioned that operations of PCS with minimum heater current had the advantage of minimum thermal losses and fast recovery time. In this work, as a thermal insulator for PCS, cotton tape that contained gum, commonly utilized to provide electrical insulation, was used. To use the cotton tape as a thermal insulator for PCS, the author calculated thermal conductivity, 0.29 W/m.K. The author designed and fabricated the PCS with this value. The experimental results for the verifying were in good accord

with calculated results for design. The adiabatic method with cotton tape also reduced the time of fabrication [66].

Most conventional persistent current switches consist of NbTi superconductive wire since its machinability is fairly good without hurting critical current density. However, the superconducting transition temperature ( $T_c$ ) of NbTi is relatively low, so unfavorable quenching may take place due to a small temperature margin when operated at 4.2 K. To eliminate this disadvantage, M. Tomita *et al.* (2001) a PCS consisting of Nb<sub>3</sub>Sn superconducting wire was designed for Superconducting Magneto Hydro-Dynamic Propulsion Ship (MHDS). Also, the different heater power applied to the PCS and the PCS performance were observed. From simulation results, it is found that 99.9 % of PCS conductors driven normal by warming for 300s with a 20 W power given to the heater. At the same time, it took only 66 s for the PCS to recover the superconducting state, which is reasonably short and thus is viable for practical applications. [67].

Dong Keun Park *et al.* (2006) A high-temperature superconducting (HTS) PCS system was designed and tested in this research. The HTS PCS was optimally designed using two different HTS tapes, second-generation coated conductor (CC) HTS tape and Bi- 2223 HTS tape by the finite element method (FEM) in thermal quench characteristic view [68].

W.B. Ma *et al.* (2006) Developed a 7 T experiment system for an MRI PCS test at the Institute of High Energy Physics (IHEP) of China. The system mainly consists of a 7 T background superconducting coil, two pairs of 800 A vapor-cooled current leads, a data acquisition system, and more. The NbTi superconducting coil, with an operating current of 376 A, has a central field of 7 T and a clear bore of 80 mm. A no-impregnation technique was used to fabricate this coil. The coil reached 96% of its short sample performance after three times quench. The PCS for the 7T magnet was designed and tested by applying 600A current in the persistence current mode with a background field of 5T [69].

Chunyan Cui *et al.* (2006) Designed and fabricated three superconducting switches with different thermal insulation materials for 400 MHz NMR magnets. A NbTi/CuNi superconducting wire with higher resistance is used and wound on the PCS bobbin in a bifilar manner for low inductance and minimum field perturbation. The experiments for the heating power and current-carrying performance have been carried out. The minimum power required for the PCS for transition is around 0.69 W, and the off-time is less than 10 S. The results also show that the performance of GFRP is better than paraffin. However, to meet the requirement of NMR magnet stability of 0.01 ppm, the performance of the superconducting joints is very important. Numerical simulations by the FEM method for the switching performance of temperature distribution during heating and cooling cycles are performed. There is an essential contradiction between the recovery time and high efficiency regarding the thickness of the insulation layer. On the one hand, the thickness should be small to achieve fast recovery. On the other hand, a small thickness would lead to more loss because more power is needed to sustain the resistive state of the PCS [70]. Milward and Stephen R. described the design details of the PCS control system for reducing a heat load while charging the superconducting Magnet [71].

Siyuan Liu *et al.* (2013) developed a thermally triggered PCS for a 7T animal MRI magnet, achieving an off-state resistance of 5  $\Omega$  at room temperature and 3.5  $\Omega$  at 4.2 K. Thermal analysis using ANSYS indicated that PTFE outperformed GFRP in insulation, with the PCS design enabling better control over switching resistance [72].

Chunyan Cui *et al.* (2016) presented the results of their work on a conduction-cooled PCS. The PCS has an off-state resistance of around 10  $\Omega$  using three strands and a 12 m length of CuNi-NbTi wire. The heat dissipation in the PCS is inversely proportional to the normal resistance of the PCS. The tested maximum persistent current is 170 A, and the magnetic field is 1.41 T [73].

Chao Li *et al.* (2018) explained the results of ac field-controlled PCS. The designed PCS was tested in the liquid nitrogen temperature [74 – 75]. The advantage



of the field-controlled PCS is its flexibility in controlling the value of the switching-off resistance. The response and recovery time of the PCS is less than 10 milliseconds. The results author concluded that the design is very compact and energy-saving, allowing us to develop a large dynamic resistance in a compact volume and with less power.

## 2.5 External interference screening

The Whole-Body clinical MRI scanners need a highly homogeneous magnetic field inside the field-of-view (FOV) at its imaging volume. The peak-to-peak homogeneity for a whole-body MRI magnet should be better than  $\pm 5$  ppm at the FOV of 45-50 cm [76]. Any external magnetic disturbances may lead to a change in the central magnetic field ( $B_0$ ) at the iso-center and its homogeneity at the imaging volume. An actively shielded magnet is relatively sensitive to external disturbances as it cannot automatically compensate for the external disturbances in its imaging volume [77].

The imaging volume of the MRI magnet needs to be protected from any such external magnetic interference. Kellogg J. (2011) Explained the various techniques available for shielding such external disturbances in the presence of a low magnetic field [86]. Still, it is difficult to shield the fluctuation using an iron or  $\mu$ -metal shield at the high field region. As a result of the high-field region, high-permeable materials, such as iron or metal, will be saturated. Thus, the shielding is ineffective. To achieve a shielding effect against any external magnetic interference, G. Gabrielse *et al.* (1991) introduced a method in which a set of shorted superconducting coils known as  $B_0$  compensation coil or screening coil which are symmetrically positioned radially from the axis and with respect to the midplane [78 – 79]. It is self-activated and works passively in the system. The spatial homogeneity of the MRI magnet needs to be preserved or even improved by the  $B_0$  compensation coil. Various researchers have designed such types of coils for whole-body MRI magnets. [82 – 85]. But most of them discussed the design aspects of it. There has been limited research reporting on their characteristics during operation or even during quenching of the MRI magnet. The magnetic active compensation system is also a technique used by some researchers.

The induced eddy current shields the high-frequency fluctuations in the ambiance on the outer vacuum jacket (Al-alloy or stainless steel) or the thermal radiation shield (Al-alloy) around the solenoid magnet of the MRI. The low-frequency fluctuations in the ambiance magnetic field may cause a significant change in the  $B_0$  field and its resonance frequency. G. Gabrieleise *et al.* (1988) & M. Lakrimi1 *et al.* (2016) Explained that the fluctuation in the ambient field varies between 10 nT to 10 nT depending on the solar activity or moving metal objects such as lifts, vehicles in the vicinity of the MRI magnet. It happens because Faraday's law of induction states that, in a magnetic field, a current or voltage will be induced in a fast-moving conducting material [80 – 81].

Hiroshi Ueda & Ito *et al.* (2015,2019) described the development of a 9.4-T REBCO coil system for whole-body MRI. In REBCO coils, screening currents are remarkably induced in the winding tape by the perpendicular component of the magnetic field to the wide face of the REBCO tape, generating an irregular magnet field that deteriorates the magnetic field homogeneity. In this paper, detailed analysis and evaluation of the influence of the shielding-current magnetic field, and examine a method and procedure for reducing it is explained in detail. They used demagnetization methods to improve temporal stability and to enhance spatial homogeneity. A tape scribing technique was used by combining both methods' results, the target values of 1 ppm/h and 10 ppm were achieved [87].

## 2.6 Research gap

The development of MRI magnets was mostly constrained to industries or research institutes in close collaboration with the industry. Due to the intellectual property (I.P.) rights and the level of competition between industries, most of this data is not available in the public domain. The data available are related to different types of magnets and do not apply directly to MRI magnets. The following gaps are identified based on the literature survey:

**Superconducting joints:**

Superconducting joint technology is one of the most crucial for the temporal stability of the superconducting coils of the MRI. An extreme low value of electrical ( $< 10^{-10}$  Ohm) resistance between the superconducting wires makes the technology very challenging in the MRI system. It is also equally important to design a 4 K experimental rig to characterize the superconducting joints with low electrical resistance. Although the basic mechanism of joint characterization, many researchers discussed the E.M. performance of the experimental test rig is not analyzed in detail considering the sensitivity of the measurement needed for such characterization. This is likely due in part to the commercial engineering focus of joint development, an endeavor led predominantly by magnet manufacturers. Many researchers have reported experimental data for superconducting joints, but the theoretical understanding of such joints is yet to be made.

The detailed analysis and extensive studies of the multi-strand/ multi-filament conductors of the PCS and the magnet have not given for better understanding of such joints for their practical application. Most of the available studies on superconducting joints are primarily for smaller applications in lab-scale research magnets.

**Persistent current switch:**

The PCS is one of the most critical components of the MRI magnet. Many researchers have developed PCS's for various applications. Minimal experimental studies have been reported on the analytical calculation of total energy dissipation and the design parameters of the PCS in the MRI system during its operating cycle. In most of the literature, only the design aspects of PCS are explained. There is room for an investigation into the PCS's temperature profile and electrical switching behavior for MRI magnets. The normal resistance of the PCS at various temperatures above critical temperature has not been studied so far, which is crucial for MRI magnets.

The MRI magnet needs two types of superconducting joints: Cu (NbTi)-Cu (NbTi) and CuNi (NbTi)-Cu (NbTi). The joint morphology, filament orientation between the conductor of the PCS and the wire-in-channel conductor of the MRI magnet have never been analyzed.

### **EIS coil:**

To achieve an efficient shielding effect against any external magnetic interference, a set of shorted superconducting coils known as  $B_0$  compensation coil or screening coil which are symmetrically positioned radially from the axis and with respect to the midplane. It is self-activated and works passively in the system. The spatial homogeneity of the MRI magnet needs to be preserved or even improved by the  $B_0$  compensation coil. Such types of coils for whole-body MRI magnets have been designed by various researchers. Most of them discussed the design aspects of it. In most of the literature, only the design aspects of the EIS coil are explained. There will be scope for optimization in designing the EIS coils to achieve an effective screening factor while considering the effect of the spatial field homogeneity. There have been no studies published regarding the characteristics of the EIS coil during the operation or during the MRI magnet's quenching.

## 2.7 Research objectives

To achieve these goals, the following research objectives are set:

1. Design and development of the PCSs through an extensive thermal and electrical analysis to achieve efficient switching performance for MRI magnet system
2. Design and development of a 4K test rig for characterization of the PCSs at 4.2K
3. Development of superconducting joints for the MRI magnet to achieve field stability in the MRI magnet system. Detailed characterization of the morphology of the superconducting joints and testing at 4K.
4. Design and development of a 4K test rig for characterization of the superconducting joints at 4.2K
5. Design an optimized superconducting EIS coil system for a whole-body 1.5T MRI magnet system through an analytical calculation in correlation with the magnetostatics simulation for various competing parameters like mutual coupling, coupling factors, field homogeneity, screening factors, etc



## CHAPTER 3

### SUPERCONDUCTING JOINTS

#### 3.1 Introduction

In the MRI magnet, the superconducting coils are initially energized to the target current using a magnet ramping unit (MRU). Once the magnet is parked at the target field, the MRU is disconnected from the magnet after establishing the persistent current through the magnet and the PCS. In the persistent mode, the magnet circuit consisting of the multiple superconducting coils and the PCS, behaves as the L–R circuit. Hence, the temporal field stability is governed by the standard current-decay equation of the L–R circuit as given by the following equation:

$$I(t) = I_0 e^{\frac{-Rt}{L}} \quad (3.1)$$

Where,  $L$  is the inductance of the magnet,  $I_0$  and  $I(t)$  are correspondingly the initial current and the current at time  $t$ , and  $R$  is the equivalent electrical resistance of the circulating current path.

The decay of the current is determined by the overall resistance of the circuit. The desired stability ( $<0.1\text{ppm/hr}$ ) of the MRI magnet will be achieved with a total electrical resistance of  $10^{-13} - 10^{-14} \Omega$  in the entire MRI magnet system. This extremely low electrical resistance value will only be possible by superconducting joints between coils, or joints between the coil and the PCS. Hence superconducting joints play the most crucial role in determining the stability of the MRI system. These joints need to be made ‘insitu’ once the coils are wound on the bobbin. There is no possibility to characterize the quality of such in situ joints until the MRI magnet is housed in a cryostat and cooled to 4.2 K. Hence, the jointing process needs to be established for their in-situ implementation after rigorous testing of the sample joints.

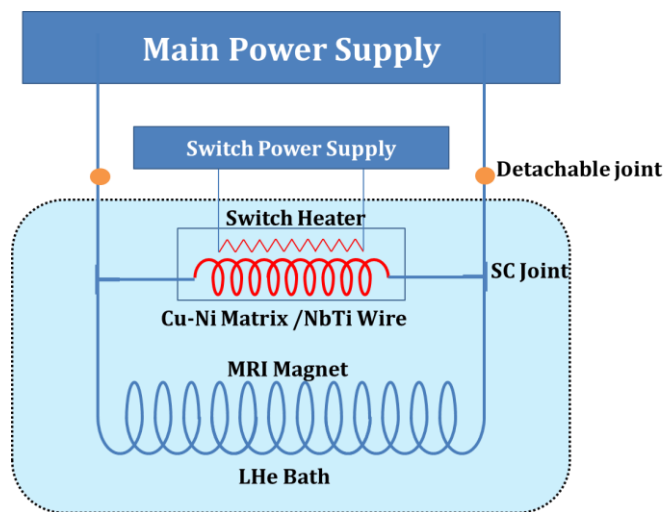


Figure 3.1 Schematic of a PCS used for the persistent mode of operation of an MRI magnet.

In this chapter, the joint-making process is discussed in detail, including the critical parameters and techniques involved in ensuring high-quality superconducting joints. The solder matrix replacement method used for joint fabrication is thoroughly examined, highlighting the importance of maintaining optimal conditions for soldering



and tinning. The chapter also delves into the joint resistance measurement process, emphasizing the need for precise control over factors such as temperature, time, joint configuration, and cleanliness to achieve reliable and efficient connections. Additionally, the reasons for joint failure are elucidated with the help of Scanning Electron Microscopy (SEM) and Energy-Dispersive X-ray Spectroscopy (EDX) analysis. This analysis reveals the presence of impurities and other defects that compromise joint performance, providing valuable insights for improving joint fabrication techniques. By addressing these factors and implementing solutions such as the use of glass tubes to maintain solder purity, the chapter discusses the importance of meticulous process control in achieving optimal joint performance. The findings and methodologies discussed herein lay the groundwork for further advancements in the field of superconducting joint technology, contributing to the development of more robust and efficient superconducting systems.

### **3.2 Superconducting MRI magnet**

An MRI magnet consists of main coils, shield coils, EIS coils, each of them performs different functions. For example, three pairs of coils (C1-C6) having mirror symmetry provide the required homogeneous main field,  $B_0$ . One pair of coils (C7-C8), known as shield coils, produces a magnetic field that is in the opposite direction of the other three pairs as shown in Fig.3.2. All eight coils are joined in series through superconducting joints and are energized by a single power supply. A PCS or superconducting switch is connected in series with the eight coils.

Typically, MRI magnets are constructed in a modular manner due to several factors: (i) constraints related to the maximum length of individual wires, (ii) challenges in controlling the magnetic field geometry, (iii) technical restrictions on coil size, and (iv) limitations in arranging the coil to generate a highly uniform and potent magnetic field.

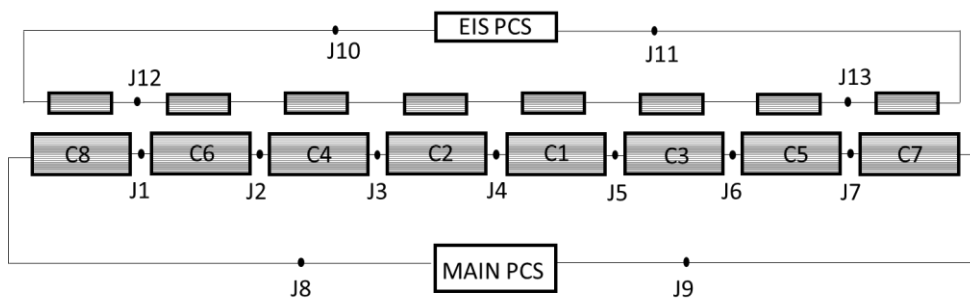


Figure 3.2 Simplified schematic of superconducting coils having inter-coil joints (J1-J7) and joints between coil and PCS (J8-J9).

Three pairs of field-shaping coils (C1 - C6) are symmetrically located along the magnet axis. One pair of shield coils (C7 - C8) is co-axially located at the larger radius. The current in the shield coils is in the reverse direction and the primary purpose of these two coils is to reduce the stray magnetic field outside the magnet. Thus, the magnetic moment created by the primary coils is canceled by creating the opposite magnetic moment by the shield coils. All coils within the MRI magnet are interconnected in series through the superconducting joints. Any resistance in these joints can lead to decay in current during persistent mode operation.

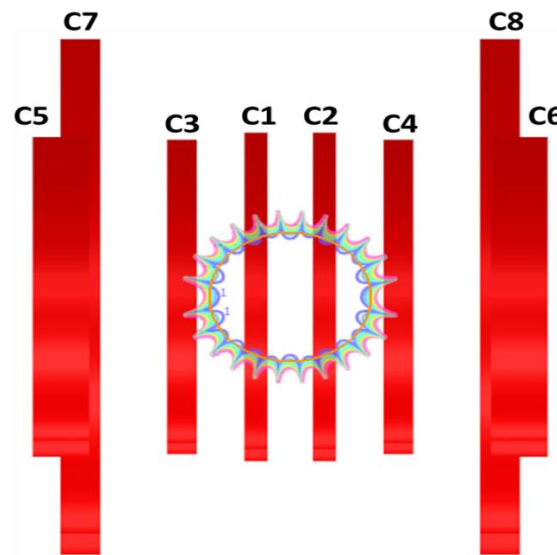


Figure 3.3 Actively shielded cylindrical MRI magnet configuration. The curved blue line in the circle represents 1 ppm uniformity.

### 3.3 Superconducting joints

Joints are used to connect all of a magnet coil in order when a single length of conductor is not long enough to build a coil and must be joined with other lengths of conductor. They can also be used between separate sections of a magnet to allow different conductors to be used at different places in the magnet as the magnetic field and internal stresses change. This allows the specifications of each conductor in a magnet system to be tailored to the local conditions that it will experience during operation. Some joints connect two conductors of the same type and some are hybrid joints, connecting different types of superconductors. The superconductors used in modern magnets have many small superconducting filaments embedded in a matrix of normal metal (multifilamentary conductors) which adds to the complexity of building joints.

Within our magnet system, we employ two distinct types of conductors. The conductor utilized for the main coils and shield coils remains consistent, whereas a different conductor is employed for the PCS. Specifically, a wire-in-channel (WIC) NbTi conductor is utilized for the main coils, while a CuNi matrix multistrand NbTi conductor is employed for the superconducting switch.

In most cases, the electrical resistance ( $R$ ) of such magnet circuits is dominated by the electrical resistances of the inter-coil joints or the coil-to-PCS joints. The magnetic field is proportional to the current. Hence, the Eq. (3.2) can be written as;

$$B(t) = B_0 e^{-\frac{tR}{L}} \quad (3.2)$$

where  $B_0$  and  $B(t)$  are correspondingly the initial magnetic field and the magnetic field at time  $t$ . Using Eq. (3.2), the field decay equation can be derived as given by Eq. (3.3)

$$\Delta B = B_0 - B(t) = B_0 \left(1 - e^{-\frac{tR}{L}}\right) \quad (3.3)$$

Using Eq. (3.3), the total resistance of the circuit can be expressed in terms of total energy ( $E = \frac{1}{2}LI^2$ ) which is given by Eq. (3.4)

$$R < \frac{2E * \text{Field Decay}}{3600I^2} \quad (3.4)$$

Where  $\frac{\Delta B}{B_0}$  is the field decay in ppm, and the total energy E is in MJ.

Currently, the Inter-University Accelerator Centre, New Delhi, is developing an actively shielded 1.5 T superconducting magnet for a whole-body clinical scanner [88]. The operating current of the magnet is ~450 A. The total stored energy of the magnet is about 3.7 MJ. To achieve field stability better than 0.1 ppm/hr, the effective resistances should be less than  $1 \times 10^{-9} \Omega$ . A multi-coil magnet typically has a few inter-coil joints and two coil-to-PCS joints. Hence, to achieve very high temporal stability, the electrical resistance of each such joint has to be  $\sim 10^{-13} \Omega$  or better. Each electrical joint needs to be made in situ directly onto the magnet after the completion of the winding of the coils.

### 3.4 Superconducting joint making methods and architectures:

The superconducting wire consists of filaments such as are embedded inside the stabilizer i.e. copper. To get a higher value of joint resistance it is necessary to remove the normal conductive metal and connect the filaments directly to each other. Ensuring the exposure of these filaments is a crucial aspect during joint fabrication, given NbTi rapid reaction with air. The formation of a non-superconducting interfacial oxide layer not only increases joint resistance but also diminishes the wettability of NbTi filaments. Recent X-ray Photoemission Spectroscopy (XPS) experiments conducted by Davies et al. revealed that even a brief 10-minute exposure to air results in the formation of a non-superconducting oxide layer exceeding 3 nm in thickness [89]. Furthermore, exposure to just 10,000 Langmuirs of oxygen (approximately 50  $\mu\text{s}$

exposure in the air) initiates the oxidation process, highlighting the sensitivity of NbTi to atmospheric conditions [90].

Various methods have been developed to prevent these issues, including cold or hot pressure bonding, spot welding, and solder matrix replacement [91 - 92]. Among these techniques, solder matrix replacement, initially proposed by Thornton, stands out as one of the most dependable methods for superconducting jointing. In the following section, we will delve into the intricacies of this technique.

### **3.4.1 Cold press welding**

Cold press welding is another simplest method to join the niobium-titanium filaments without an intermediate material. This method is also called crimping. This method, which was first patented by James Nuding for multifilamentary NbTi wires [93], involves removing the copper stabiliser with acid, twisting the exposed filaments together, and then placing them in a tube called a crimp and pressing them at room temperature. The detailed process of the cold press joint is explained in Fig.3.4.

The crimping pressure is the main component that influences joint performance [94]. Many studies indicate that performance varies with pressure, but no comprehensive study has been done to guarantee that something will function well under pressure. It demonstrates some ambiguity in the combined techniques.

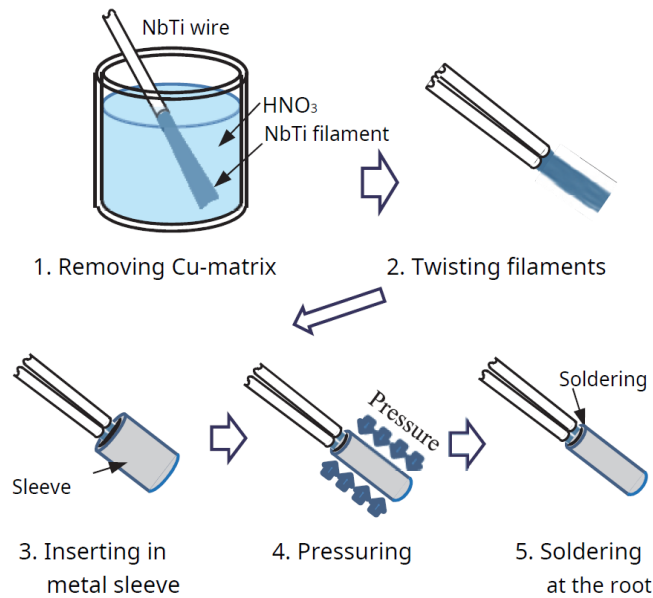


Figure 3.4 The simplified representation of the cold-press joint process. [95]

### 3.4.2 Spot welding

It is a process commonly used to join sheet metal and involves passing a high current pulse through the workpieces, generating sufficient resistive heat to fuse them. Spot welding is very effective at fusing the filaments, eliminating oxides, and forming a consolidated bulk. However, the temperature is raised to  $>2000^{\circ}\text{C}$  in the center (melting the NbTi) and Cu infiltrates from the electrodes to form Cu-Nb-Ti phases.

- Persistent joint properties can be achieved with spot welding.
- However, the dendritic microstructures are typical of an as-cast microstructure in Nb-Ti, which has a wide composition range between the liquidus and solidus lines.
- The heat-damaged microstructure is likely responsible for the reduced joint  $I_c$  compared to the wires. This makes spot welding hard to make reliable as a jointing technique.

The original patent for spot welded joints made directly between Nb-Zr monofilaments was filed by Karvonen in 1970 [96]. In his report, Karvonen notes that

joints made directly between the monofilaments exhibit poor performance, achieving only about 10% of the wire's critical current ( $I_c$ ) at 4.2K and 3T. Although the underlying cause is not explicitly discussed in the patent, it is hypothesized that the poor performance might be attributed to heat damage sustained by the material in the joint region. Such damage could potentially reduce the upper critical field ( $B_{c2}$ ) and/or the critical current density ( $J_c$ ) of the material.

Karvonen further reports a significant improvement in performance when the monofilaments are laid side by side on a suitably thick NbTi foil. By spot welding each filament to the foil at multiple locations along their length, the performance increases to more than 80%, even in magnetic fields of up to 6 T [97]. This method is visually represented in a sketch shown in Fig.3.5. The precise mechanism by which this technique improves performance is not fully understood. However, it is speculated that the NbTi foil might provide a better heat sink during the welding process, thereby minimizing heat damage to the monofilaments. Additionally, the foil could potentially offer structural support and reduce stress concentrations at the joints, further enhancing the overall performance of the welded connections.

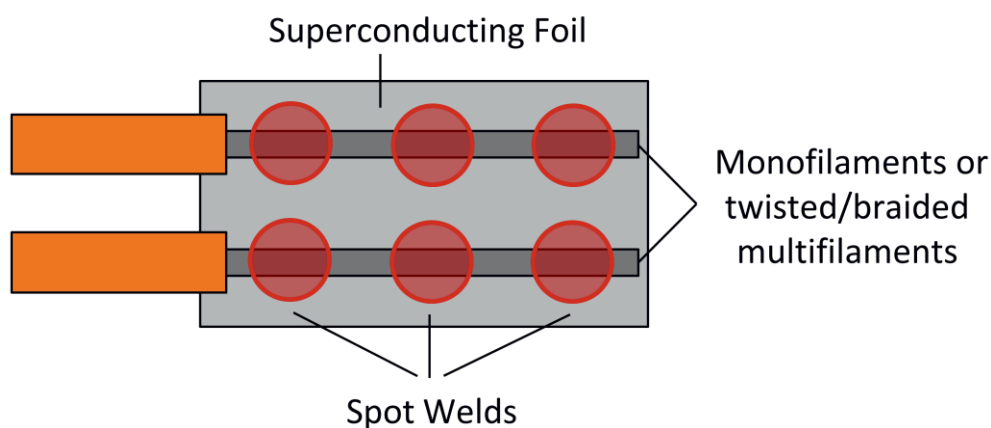


Figure 3.5 Schematic of typical NbTi spot welded joint with NbTi filaments spot welded to a Nb-NbTi foil. The filaments of each wire can be twisted prior to spot welding if desired for ease of handling. [50, 97]

Considering the various factors discussed in the previous section, the unpredictability of performance associated with the cold press and the spot-welding methods is highly undesirable for industrial applications. Therefore, from an industrial perspective, the solder matrix replacement method emerges as the best option for creating superconducting joints.

### 3.4.3 Soldering

Soldering is the most often used industrial jointing technique for superconducting wires. In this method, the copper matrix of the superconducting wire is removed by dipping the wire into the molten tin bath. Or else the copper can be removed by using nitric acid but as mentioned above the NbTi alloy gets oxidized immediately when it comes in contact with the air so to remove the oxidation layer it needs to deep into the hydrofluoric acid (HF) and needs to be tinned using low melting superconducting alloy.

To eliminate this major problem of oxidation in 1986 Roy F. Thornton first time described how to prepare superconducting joints with NbTi filamentary wire in his patent. This patent is the base reference for the solder matrix method of the superconducting joint. Due to the oxidation problem discussed, poor wetting reportedly prevents soldering to bare NbTi filaments, and common fluxes are unable to remedy this [39]. This method has proven to be extremely effective, with PbBi/NbTi joints demonstrated to carry 1000A at 4.2K and 1T, exhibiting resistances in the range of  $10^{-13}$  to  $10^{-14}$  ohms [98]. The performance of these joints is significantly influenced by the superconducting properties of the solder, making a discussion on the superconductivity of PbBi particularly valuable at this stage.



### 3.5 Superconducting solders

#### 3.5.1 Lead-based solder materials

For most industrial applications, such as MRI, lead-bismuth (PbBi) or lead-bismuth-tin (PbBiSn) alloys are used as solder for superconducting joints. Specifically, references [52, 48, 99,39] indicate the use of PbBi alloys, while [45, 101, 90,100,] report the use of PbBiSn alloys. In a few early cases, Wood's metal (PbBiSnCd) was also utilized [100].

The binary phase diagram of the PbBi system, depicted in Fig.3.6, shows two lead-rich solid solutions: the  $\alpha$  and  $\epsilon$  phases. According to source [90, 102], the  $\epsilon$  phase exhibits superior superconducting properties. Both the critical temperature and the critical field of the  $\epsilon$  phase increase with the bismuth content within this phase field. Sources [103-104] highlight the critical temperature improvements, while [105] focus on the critical field enhancements.

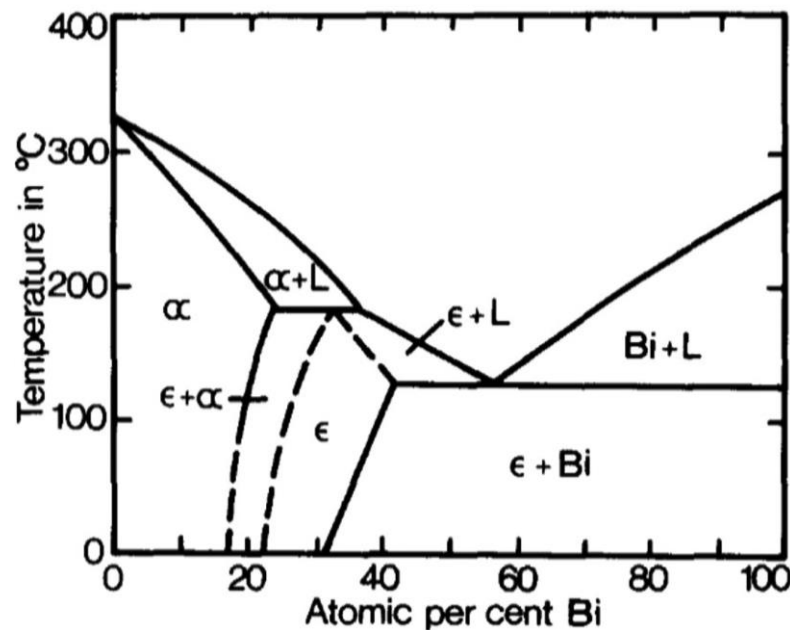


Figure 3.6 Binary phase diagram of the PbBi system. [102, 90]

Most PbBi alloys employed in joint manufacturing are either  $Pb_{60}Bi_{40}$  or eutectic  $Pb_{45}Bi_{55}$  by atomic percent. The exact composition of the alloys used in many reports is often unspecified, complicating direct comparisons. However, Campbell et

al. and Kodama et al. have reported that the critical current is higher in the eutectic alloy. This improvement is attributed to a greater specific surface area of normal-phase bismuth particles within the eutectic composition, which provides more effective flux pinning, thereby enhancing the overall superconducting performance [106].

Table 3.1 Lead-based solder materials. [90]

Composition	Tc\ K	Bc2\T	Reference
Pb <sub>60</sub> Bi <sub>40</sub>	8.4	1.77 (at 4.2 K)	[107]
Pb <sub>32</sub> Bi <sub>53</sub> Sn <sub>15</sub>	8.68	1.98 (at 1.3 K)	[108]
Pb <sub>50</sub> Sn <sub>50</sub>	7.75	0.20 (at 1.3 K)	[108]
Pb <sub>50</sub> In <sub>50</sub>	6.35	0.48 (at 1.3 K)	[108]
Pb <sub>60</sub> Bi <sub>40</sub>	8.4	1.77 (at 4.2 K)	[108]

### 3.5.2 Lead free solder materials

EU legislation currently allows an exemption for diagnostic medical devices regarding the use of high-temperature leaded solders, but this exemption is scheduled for review in 2023 [90]. Consequently, there is significant interest in identifying lead-free alternative solders. Ideally, the industry seeks a direct replacement for lead-bismuth solder that offers similar or improved superconducting properties. However, as indicated in Table 3.2., most lead-free systems exhibit much lower critical fields and temperatures.

Among the potential alternatives, the indium-tin (InSn) binary system stands out as the next best option. This system has been extensively studied, both in the 1960s and more recently, specifically for its application in superconducting joints. Despite these investigations, other potential candidates, such as cadmium, mercury, and thallium, are unsuitable due to their toxicity. Therefore, while InSn remains the most promising lead-free alternative, the search for an optimal replacement for lead-bismuth solder continues to be a critical focus for the industry.

While the critical current is sufficiently high for joint manufacture at very low magnetic fields, with even quenched samples exhibiting a critical field of only 0.15 T

at 4.2 K, this low critical field would necessitate extensive shielding for industrial applications. Currently, even the best lead-free solders are unable to meet the stringent requirements of the MRI industry, which demands a background field of 1.0 T at 4.2 K and the capability to carry current over 1000 A. Consequently, further advancements are essential to develop a viable lead-free alternative that can fulfill these industry standards.

Table 3.2 Lead-free solder materials. [90]

Composition	T <sub>c</sub> \ K	B <sub>c2</sub> \ T	Reference
In <sub>50</sub> Sn <sub>50</sub>	7.45	0.64 (at 1.3 K)	[108]
In <sub>50</sub> Sn <sub>50</sub> Quenched	6.7	0.14 (at 4.2 K)	[109]
In <sub>50</sub> Sn <sub>50</sub> Air cooled	5.6	0.04 (at 4.2 K)	[109]
In <sub>50</sub> Sn <sub>50</sub> Quenched and aged	6.1	0.08 (at 4.2 K)	[109]
Sn <sub>35</sub> In <sub>50</sub> Bi <sub>15</sub> Air cooled	6.9	0.18 (at 4.2 K)	[109]
In <sub>78</sub> Bi <sub>22</sub>	-	0.22 (at 0 K)	[110]
Sn <sub>85</sub> Zn <sub>15</sub>	-	0.10 (at 0 K)	[110]

### 3.6 Conductor used for MRI magnet winding

For the main magnet, many MRI manufacturers use WIC conductor for winding the magnet coils. In WIC, the NbTi wire is inserted in a copper channel filled with solder. WIC is then insulated with polyester braid. For MRI magnets a higher Cu/NbTi ratio of 5:1 to 20:1 is preferred for achieving high conductor stability. The typical dimensions of the wire marketed by OST are 2.286 x 1.524 mm, filament dia. 82 μm, no. of filaments 55, J<sub>c</sub> is 1210 A (4.2 K, 3 T), Cu: NbTi is 10.5. Fig.3.7 shows the cross-sections of a WIC conductor used for MRI magnets.

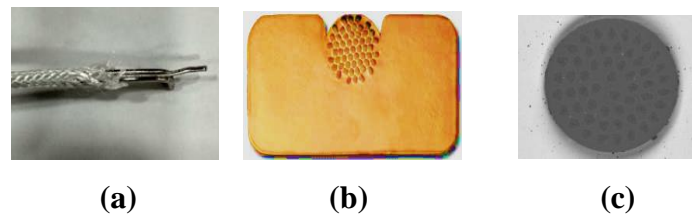


Figure 3.7 (a) WIC conductor (b) Cross section of the WIC conductor. (c) NbTi Filaments.

### 3.7 Superconducting joint making using solder matrix replacement method

The process of the joint making is shown in Fig.3.8 below. This involves removing any metallic stabilizer immersing the filaments in molten superconducting solder alloy and then placing the wires in the liquid tin at about 300°C to 350°C to dissolve the copper and substitute it with tin without exposing the filaments to air – a process is generically known as tinning although it is possible to use other molten metals/alloys.

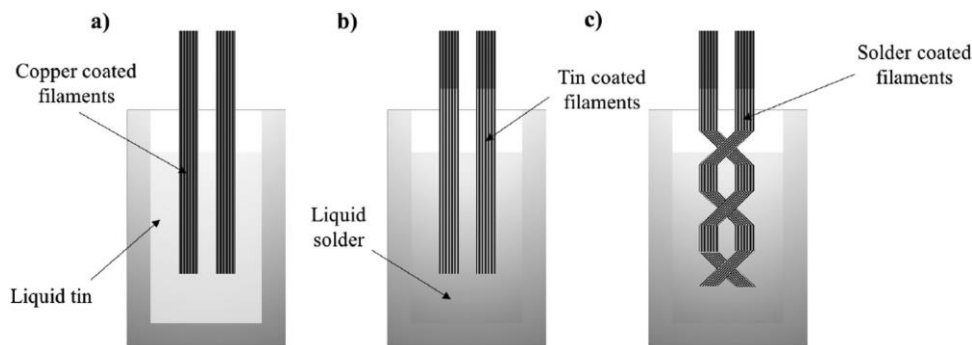


Figure 3.8 A schematic of the Thornton matrix replacement method. [90]

Considering the drawbacks of other methods, we decided to use the solder matrix replacement method for making superconducting joints and began preparing for it. Even in the solder matrix replacement method, numerous factors such as soldering and tinning temperatures and times must be considered, but no comprehensive studies have been published. Reported tinning periods for the initial step alone range from ten minutes [97] to more than two hours [48], with the ideal conditions depending on the wire diameter and the copper thickness around the NbTi filaments. Recent studies on the formation of reaction layers between molten tin or solder and niobium-titanium alloy [97] suggest that the performance of the joint may depend on reaction time.

To gain a comprehensive understanding of the solder matrix replacement method for making superconducting joints, more than 30 superconducting joints were prepared and analyzed. This method involves several critical factors that influence the performance of the joints. Each of these factors was carefully examined to determine

their impact on joint performance. The detailed analysis of these factors is explained below:

j) Soldering and tinning temperatures:

The temperature at which soldering and tinning are performed is crucial. The optimal temperatures ensure proper bonding between the solder and the superconducting wire material while minimizing the risk. If the temperature is too low, the solder may not properly melt and flow, resulting in weak joints with poor electrical conductivity. Conversely, excessively high temperatures can damage the delicate superconducting filaments, particularly NbTi, by causing unwanted diffusion of elements and degradation of superconducting properties. Precise control of temperature is thus vital to maintain the integrity of the superconducting wires and achieve strong, conductive joints.

k) Soldering and tinning times:

The duration for which soldering and tinning processes are carried out significantly affects the quality of the joint. Tinning periods can range from ten minutes to more than three hours, depending on specific conditions such as the type of solder, the nature of the materials being joined, and the desired thickness of the copper layer on the superconductor. Short tinning times might result in incomplete coverage, leading to areas of poor electrical contact. On the other hand, excessively long tinning time can cause overheating and potential degradation of the superconducting material. Finding the ideal tinning time for a given set of conditions ensures thorough and even solder coverage without compromising the material properties.

l) Background atmosphere near the joint:

The atmosphere surrounding the joint during soldering and tinning can impact the quality of the bond. A controlled atmosphere, often an inert gas like argon or nitrogen, helps prevent oxidation and contamination of the solder and superconducting materials. Oxidation can introduce impurities that degrade the electrical and thermal conductivity of the joint. By maintaining a clean, controlled atmosphere, it is possible

to minimize the introduction of defects and impurities, leading to higher-quality joints with improved performance and reliability. The figure below shows the argon hood designed to maintain an inert atmosphere during the preparation of the joint.

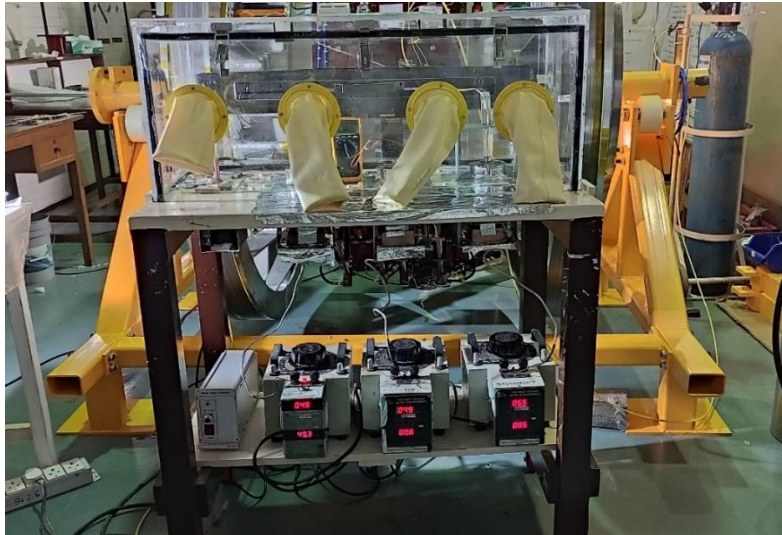


Figure 3.9 superconducting joint-making setup with argon hood and solder bath.

m) Length and formation of the joint:

The length and formation of the joint are critical parameters that influence its mechanical strength and electrical performance. Longer joints provide more contact area, which can reduce electrical resistance and improve current-carrying capacity. However, excessively long joints may introduce unnecessary complexity and potential points of failure. The formation, or geometric configuration, of the joint should be designed to maximize contact area while maintaining structural integrity. Proper alignment and uniformity in the joint formation ensure consistent performance across different joints and reduce the likelihood of localized weak points. The joints shown in the first figure are somewhat complex during the tinning process due to the unpredictable dissolution of copper over time. This inconsistency in copper dissolution has led to varying joint resistances, as the tinning was not always perfectly implemented, even with the same time duration. To address this issue, we developed a straight joint design shown in Fig.3.10(b), allowing the solder to flow more easily around the conductor. This new approach ensures a smoother and more consistent tinning process, thereby improving the reliability of joint resistance.

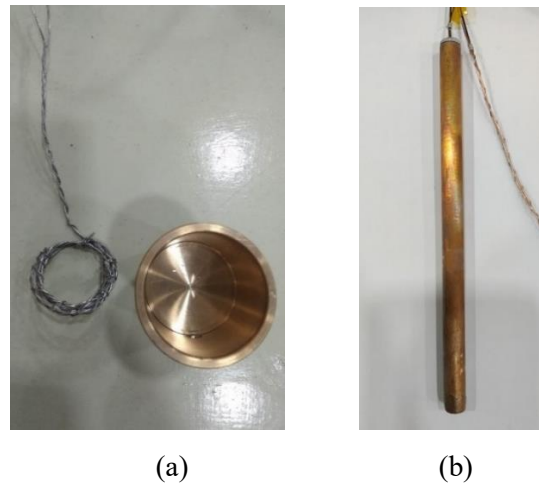


Figure 3.10 (a) A photograph of the spiral joint and (b) a photograph of the straight joint.

n) Solder purity:

The purity of the solder used in forming the joint has a direct impact on its electrical and mechanical properties. Impurities in the solder can introduce resistance and reduce the joint's conductivity, compromising the performance of the superconducting connection. High-purity solder ensures a clean bond with minimal resistance, maintaining the superconducting pathway's efficiency. It is essential to source and utilize solder materials with the highest possible purity to achieve optimal joint performance. To eliminate impurities, the solder was placed in a glass tube and heated by radiation, rather than being immersed in the stainless-steel solder bath, ensuring a contamination-free environment and maintaining the purity of the solder throughout the process.

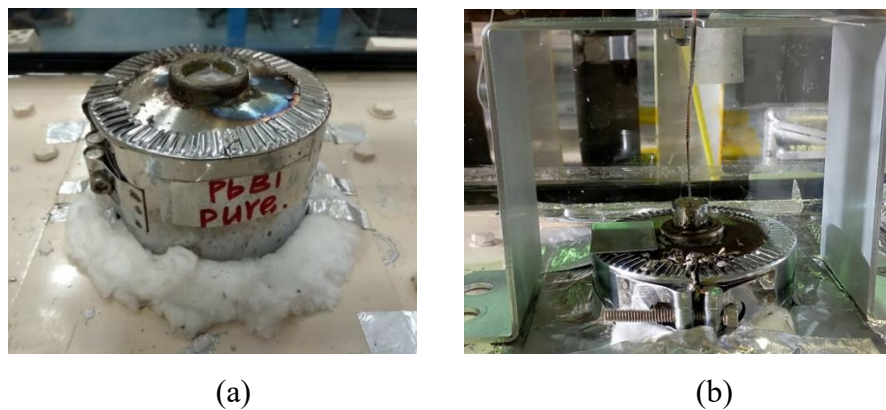


Figure 3.11 PbBi solder bath without glass tube (b) PbBi solder bath with glass tube.

o) Cleanliness:

Maintaining cleanliness throughout the soldering and tinning processes is paramount. Contaminants such as dust, oils, and residues can significantly affect the quality of the joint. These contaminants can create barriers to proper solder adhesion and introduce defects that compromise the joint's integrity. Thorough cleaning of the wires and soldering equipment, as well as working in a clean environment, helps prevent the introduction of contaminants. Ensuring all surfaces are free from impurities before and during the soldering process leads to stronger, more reliable joints.

By meticulously analyzing these factors, we aimed to optimize the solder matrix replacement method and improve the performance of superconducting joints. The insights gained from preparing and studying these 30 joints provide valuable guidance for refining the process and achieving more reliable and efficient superconducting connections. The process that followed to prepare the final superconducting joints for the MRI magnet is explained in detail in the 3.8.4 section.

### **3.8 Procedure for building superconducting joints**

#### **3.8.1 Solder: PbBi**

As mentioned in the previous section there is no lead-free solder till the date which meet the requirement of the MRI magnet, a background field in the range of 0.6 to 1.0 T at 4.2 K temperature to carry more than 500 A of current. The best suitable solder is PbBi. The details specification of PbBi is given in the lead-based solder section. The binary phase diagram of the PbBi system, as depicted in Fig.3.6, reveals the existence of two lead-rich solid solutions: the  $\alpha$  phase and the  $\epsilon$  phase. Among these, the  $\epsilon$  phase is recognized as the superior superconductor. In the context of superconducting joint fabrication, most PbBi alloys utilized are either  $\text{Pb}_{60}\text{Bi}_{40}$  or eutectic  $\text{Pb}_{45}\text{Bi}_{55}$  by atomic percent. In our study, we utilized the  $\text{Pb}_{60}\text{Bi}_{40}$  alloy combination. To verify the purity of the solder, Energy Dispersive X-ray Spectroscopy (EDX) analysis was conducted at IUAC. The results of the EDX analysis are presented in Table 3.3.



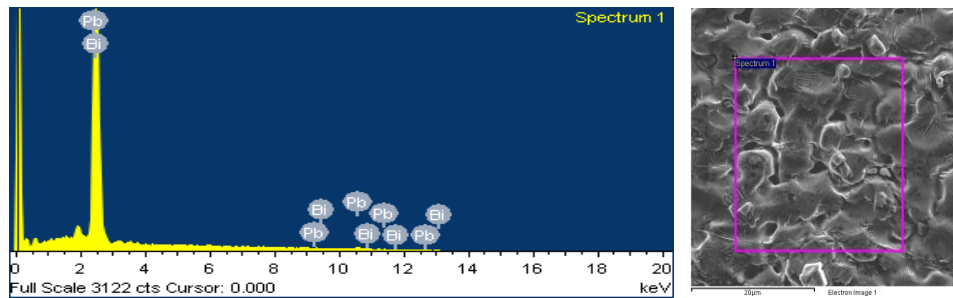


Figure 3.12 The EDS analysis of the PbBi solder.

Table 3.3 EDX analysis of PbBi solder.

Element	Weight%	Atomic %
Pb	59.75	59.96
Bi	40.25	40.04
Total		100

### 3.8.2 Solder: Tin

In the solder matrix replacement method, the tinning process is employed to remove the copper section present on the filaments. During this process, the copper dissolves in the molten solder at a specific temperature and time. Here also to verify the purity of the solder, EDX analysis was conducted. The results of the EDX analysis are presented in Table 3.4.

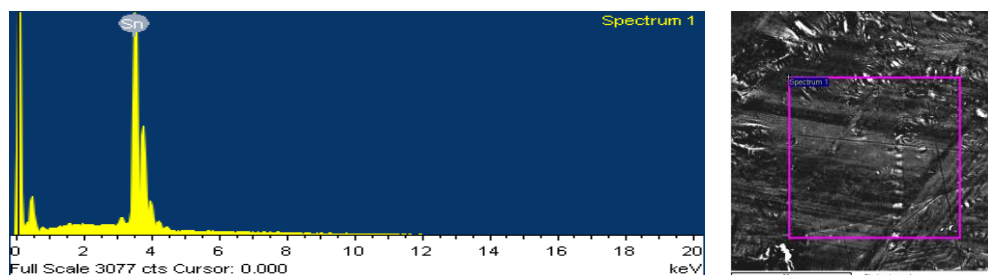


Figure 3.13 The EDS analysis of the Tin solder.

Table 3.4 EDX analysis of Tin Solder.

Element	Weight%	Atomic %
Sn	100	100
Total		100

### 3.8.3 Joint making setup

For NbTi filaments, it is crucial to perform the joint process in an argon atmosphere to avoid oxidation. To achieve this, an argon hood was prepared. The joint-making station is equipped with both a molten Tin bath and a PbBi solder bath. These baths are covered by an argon hood, allowing argon gas to flow continuously to maintain positive pressure inside the hood. Each bath has a depth of 16 cm and a diameter of 2 cm. The argon gas flow turned on after the joint dipped into the tin bath. No precise pressure value is specified. Inside the bath, positive pressure is maintained. The photograph of the joint-making station is shown below in Fig.3.14.

The joint-making station consists of two solder baths: one for Tin and another for PbBi. The section shown in Fig.3.15 is the joint cup, which is clamped with a clamp heater. Once the tinning process is completed, the joint is placed in this cup containing molten PbBi. The clamp heater is used to melt the PbBi in the joint cup.

The joint-making station consists of two solder baths and one clamp heater to heat up the joint cup. The temperature of each bath is controlled by using a variable ac source. To maintain the purity of both solders, the molten solder is kept in glass tubes measuring 15 cm in length and 1.5 cm in diameter. Initially, the glass tubes, placed inside the solder baths as shown in Figure 3.15, are heated to the desired temperature. Then the solder rods are cut into small pieces and placed inside the glass tubes. Tin solder begins to melt at 256°C, while PbBi solder starts melting at 134°C. To ensure a consistent temperature throughout the length of the molten solder, the glass tubes are heated at a constant voltage for approximately one hour. Once the molten solder reaches a stable temperature, the tinning process can begin.



Figure 3.14 Joint-making station with argon hood.



Figure 3.15 A photograph of the PbBi and Tin solder baths.

### 3.8.4 Process

Careful attention must be paid to the specifics of making the superconducting joints, as previously discussed in section 3.7. In the case of an MRI magnet, two different types of conductors are used: a WIC (Wire-in-Channel) conductor for the magnet and CuNi-NbTi conductor for the PCS. As explained in section 3.6, there are two types of joints formed in the MRI system: the WIC-to-WIC/coil to coil conductor joint and the coil-to-PCS conductor joint. The detailed process for each type of joint is outlined below.

## a) WIC- WIC joint (J1-J7)

For the WIC-to-WIC conductor joint, the process begins by preparing the ends of both WIC conductors. This involves cleaning and tinning the conductor ends to ensure good electrical contact between the filaments and to remove any oxidation. After tinning and soldering with PbBi the joint will be placed in the joint cup, which contains molten PbBi solder. The joint is heated using a clamp heater to ensure the solder flows around the conductors, creating a strong, reliable joint. Once the solder is cooled and solidified, the joint is inspected for continuity and mechanical stability. The process of creating a joint for WIC-to-WIC wire is illustrated in the flow chart shown in Fig.3.16.

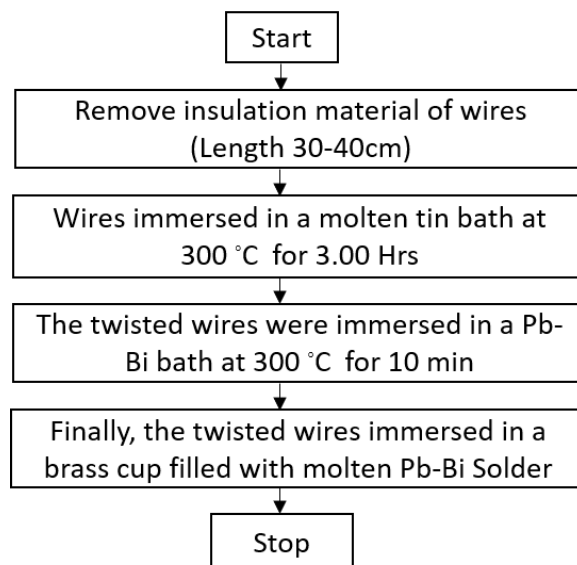


Figure 3.16 Flow chart for WIC-WIC joint.

## b) WIC to PCS wire joint (J8-J9)

For the WIC-to-PCS conductor joint, the process differs slightly due to the different conductor involved. First, the CuNi-NbTi conductor end is prepared by stripping the insulation layer. The exposed wire is then aligned and twisted together before being dipped into a molten tin bath for the tinning process. Once the tinning process is complete, the joint is dipped into a PbBi bath. Subsequently, it is placed in the joint cup with molten PbBi solder and heated with a clamp heater to create the final joint.

The detailed process of creating a joint for WIC-to-PCS wire is illustrated in the flow chart shown in Fig.3.17.

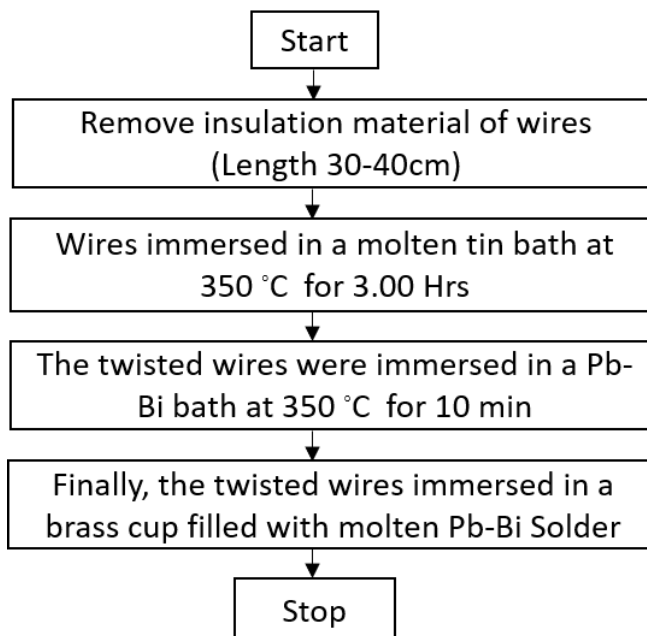


Figure 3.17 Flow chart for WIC to PCS joint.

Throughout both the processes, maintaining an inert atmosphere using an Argon hood is crucial to prevent oxidation. The entire joint-making station is equipped with this feature, ensuring high-quality joints are formed without contamination. This attention to detail in the preparation and joining processes ensures the reliable performance of the MRI magnet system.

### 3.9 Characterization of superconducting joint

The development of superconducting joints with electrical resistance in the range  $10^{-13}$ – $10^{-15}$   $\Omega$  not only poses a big technological challenge, but precise measurements are also a challenging task. The superconducting joint in the MRI magnet experiences a significant amount of background field; therefore, it is necessary to characterize the joint in the presence of a background magnetic field. The two most common methods of measuring the resistance of the superconducting joints are the four-probe method and the current or field-decay method.

The four-probe technique is limited by the voltage measurement up to  $\sim 10^{-9}$  V, thereby limiting the measurement up to  $10^{-11}$   $\Omega$  of the electrical resistance. Whereas, the field-decay method has a good sensitivity until  $10^{-15}$   $\Omega$  of the electrical resistance [50-56]. Although the field decay method cannot measure the resistance of an individual joint if two or more joints are connected in series; a longer duration is also needed to achieve a steady state. It is possible to reduce the duration of the measurement by reducing the self-inductance of the test loop, but it may reduce the overall accuracy. The overall measurement accuracy can be improved by increasing the induced current in the test coil; therefore, a higher induced field needs to be generated. This field decay technique measures the decaying magnetic field generated by an induced current into the sample coil or the test coil closed by the joints. The effective resistance is then calculated from the field-decay curve, thereby making it a direct measurement method. The superconducting quantum interference device (SQUID) [90] based commercial magnetic property measurement system (MPMS) is also used for the measurement of electrical joint resistance.

The MPMS-based commercial measurement system, although it uses an indirect method to measure resistance, provides similar accuracy. Although the measurement time is substantially reduced in the SQUID-based system, it has a limitation in the size of the joint sample. In addition, all commercial measurement systems, i.e., MPMS, do not allow for measuring the electrical resistance of the joints between two different conductors, which is necessary to characterize the coil-to-PCS joint, i.e., between the conductor Cu-NbTi of the magnet and the conductor CuNi-NbTi of the PCS.

### 3.10 Joint resistance measurement principle

Fig.3.18 shows the simple schematic of the 4 K insert. A large amount of the current is induced into a small superconducting coil acting as the secondary coil of a superconducting transformer by another superconducting coil acting as the primary

coil of the same transformer. Any change in flux in the primary coil will be conserved by Lenz's law of flux conservation, which is given by the following equation:

$$\int (B_p + B_s) dA = 0. \quad (3.5)$$

When a shorted superconducting coil, i.e., the secondary coil, experiences a varying magnetic field (either during ramping up or ramping down of the primary coil), the current will be induced in the secondary coil to maintain the total magnetic flux because of their inductive coupling. Therefore, an induced field is generated by the secondary coil, which will slowly decay over time following Eq. (3.5).

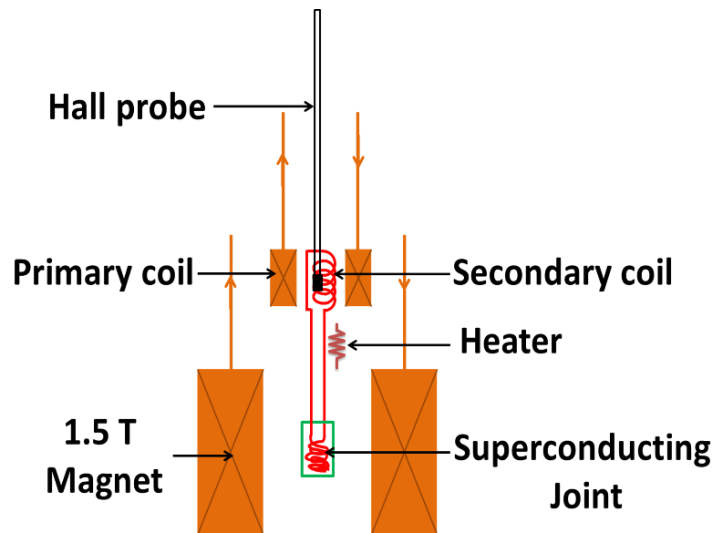


Figure 3.18 Schematic representation of basic components of the 4 K insert.

### 3.11 Experimental test rig

Fig.3.19 (b) and (c) respectively show the 3D model of the 4 K insert and the experimental dewar integrated with the 4 K insert. Fig. 3.19(a) shows the photograph of the 4 K insert. It consists of the following major components.

- a. Superconducting primary coil
- b. Superconducting secondary coil i.e. test loop having joint(s)
- c. 1.5 T superconducting solenoid magnet
- d. Two pairs of vapour-cooled current leads (VCCL)

The insert has a top lid that is used to mount the helium dewar. There is a 1.5 T superconducting solenoid magnet at the bottom of the insert as shown in Fig.3.19 (b) which generates the background field for the superconducting joint. The magnet is supported by three GFRP rods that are fixed at the top lid of the insert. There is a small superconducting coil acting as the primary coil mounted at a certain height from the magnet as shown in Fig. 3.19(a). The primary coil is positioned at the minimum background field. The secondary coil which is part of the test coil is placed concentrically and coaxially inside the primary coil. Whereas the test joint of the secondary coil is placed at the center of the superconducting magnet. There is a pair of vapour-cooled current leads connected to the leads of the primary coil. Another pair of vapor-cooled current leads is connected to the 1.5 T solenoid magnet. A manganin wire heater (36 AWG) of resistance of  $30 \Omega$  is wound on the secondary coil to quench the test coil whenever necessary during the measurement. The GE - varnish is used to make thermal contact between the manganin wire heater and the secondary coil. The heater is fed 250 mA of excitation current to quench the secondary coil using a Keithley source meter (model 2400). It will dissipate 3.7 J of energy to the liquid helium bath in 2 s of quenching time. Both pairs of current lead have the capacity to carry 150 A of current. A liquid helium level sensor is fixed to the 4 K insert to measure the helium level during the experiment. However, the liquid helium level sensor is not essential as most of the commercial helium dewar has differential-pressure-based helium level meter.

The developed versatile 4 K insert-type test rig that does not need any specialized experimental dewar. It can be inserted into any helium dewar with a neck diameter of more than 90 mm. This 4 K insert allows testing longer joint samples, i.e. up to 150 mm in length, either in straight configuration or even much longer in spiral configuration. It also allows for measuring the electrical resistance of joints between two different conductors. It has the capacity to induce a higher amplitude of current (>600 A) into the sample coil, thereby generating a higher amplitude of field. A superconducting solenoid magnet at the bottom of the insert allows us to characterize the joint at the background field up to 1.5 T.



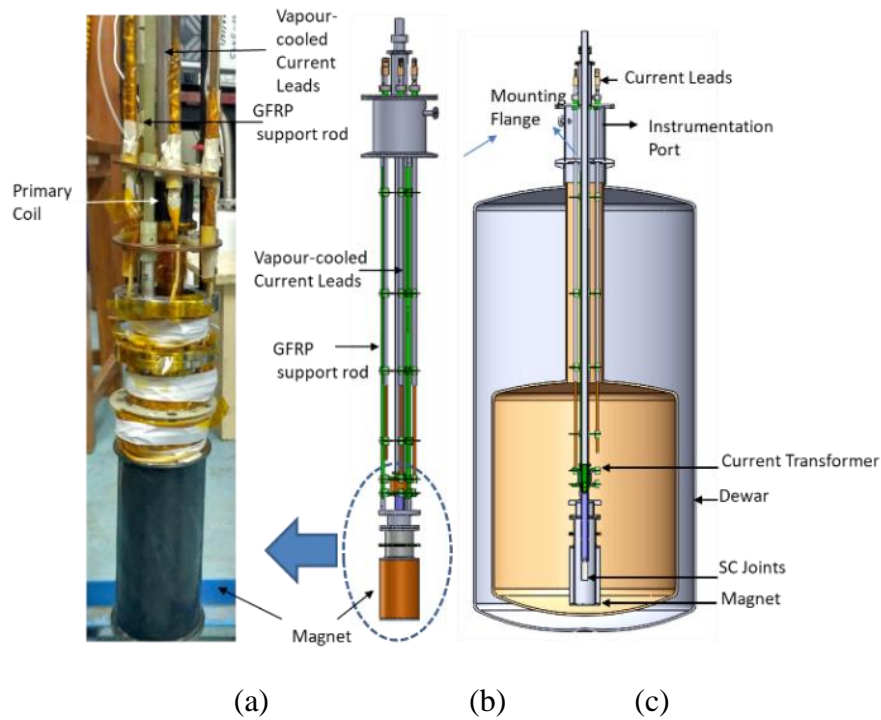


Figure 3.19 (a) Photograph of the partial section of the 4K insert, (b) the 3D model of the 4K insert, and (c), the insert mounted into the 4K dewar.

The design parameters of the primary coil are given in Table 3.5. It is made up of Cu- NbTi conductor having a 1:1.35 superconductor to copper ratio. A total 150 number of turns are wound on a glass fiber-reinforced plastic (GFRP) former of the primary coil which is impregnated with the Stycast 2850FT epoxy. Fig.3.20 (a) and Fig.3.20 (b) respectively show the photograph and the schematic of the superconducting primary coil of the 4 K insert. The secondary coil is made up of the same superconducting wire that is used for the magnet as the joint behaviour needs to be studied for the same conductor using the 4 K insert. Typically, 12-15 turns are wound on a small GRRP or tufnol bobbin having a diameter less than the inner diameter of the former of the primary coil thereby, makes it possible to place the secondary coil inside the primary coil.

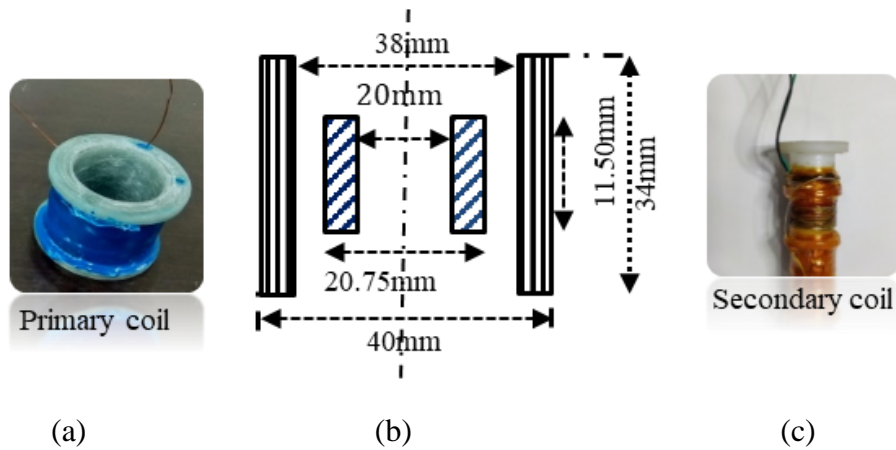


Figure 3.20 (a) The photograph of the superconducting primary coil, (b) the dimensional schematic of the superconducting primary and the secondary coil, and, (c) the photograph of the superconducting secondary coil i.e. tests coil of the 4 K insert.

Table 3.5 Parameters of the primary coil.

Description	Values
Winding length	30 mm
Total no. of turns	150
No. of layers	3
Inductance ( $L_p$ )	0.75mH
Conductor	Cu-NbTi (dia-0.54mm)
Field at 100A	0.31 T

The turns ratio between the primary and the secondary is in the range of 10-12.5 :1. The ratio of the cross-sectional areas between the primary and the secondary coil is 3.4 :1. Hence the secondary coil will experience 66 % of the flux of the primary coil. The secondary coil needs to be changed every time for the new test sample. Fig.3.21 (a) shows the schematic representation of the straight single joint between two ends of a single superconducting wire (conductor -1). Fig.3.21(b) shows the schematic representation of the two straight joints between each pair of ends of two different superconducting wires (conductor -1 and 2). Fig.3.21 (c) shows the schematic representation of the spiral joint between two ends of a single superconducting wire (conductor -1). The inductance of the secondary coil was calculated using Eq. (3.6) because the insulation was not used in the closed-loop coil [111].

Table 3.6 Parameters of the secondary coil.

<b>Description</b>	<b>Values</b>
Winding length	12 mm
Total no. of turns	12
No of layer	1
Inductance (Ls)	5 uH
Conductor	Cu-NbTi

$$L = \mu_0 a_1 N^2 \left(\frac{\alpha+1}{2}\right) \left\{ \ln \left[ \frac{2(\alpha+1)}{\beta} \right] - 0.5 \right\} \quad (3.6)$$

In the case of a single conductor, both configurations shown in Figs.3.21(a) and 3.21(c) can be used. These configurations can be used for the inter-coil joining of the magnet. In the case of two conductors, the configuration shown in Fig.3.15(b) can be used. The configuration shown in Fig.3.21(b) is primarily for the coil-to-PCS joining. Any of the configurations shown in Fig.3.21. can be used in the 4 K insert. For the straight joint as shown in Fig.3.21(a) and 3.21(b), a copper or brass tube having an inner diameter in the range of 6-10 mm is used to hold the joint at the centre of the magnet as shown in Fig.3.22 (c). Similarly, for the spiral joint as shown in Fig. 3.21(c), a copper or brass cup having an inner diameter in the range of 30-40 mm is used to hold the joint at the centre of the magnet at the bottom of the 4 K insert. The parameters of the solenoid magnet are given in Table 3.7. The magnet will generate a 1.5 T magnet field at 53 A of the operating current. The diameter of the magnet bore is more than 60 mm sufficient to place a maximum of two joint tubes side by side for straight joints (as shown in Fig.3.21b) or the joint cup for the spiral joint (as shown in Fig.3.21c). The length of the magnet is also decided to accommodate joint tube of having straight joint of maximum length up to 150 mm.

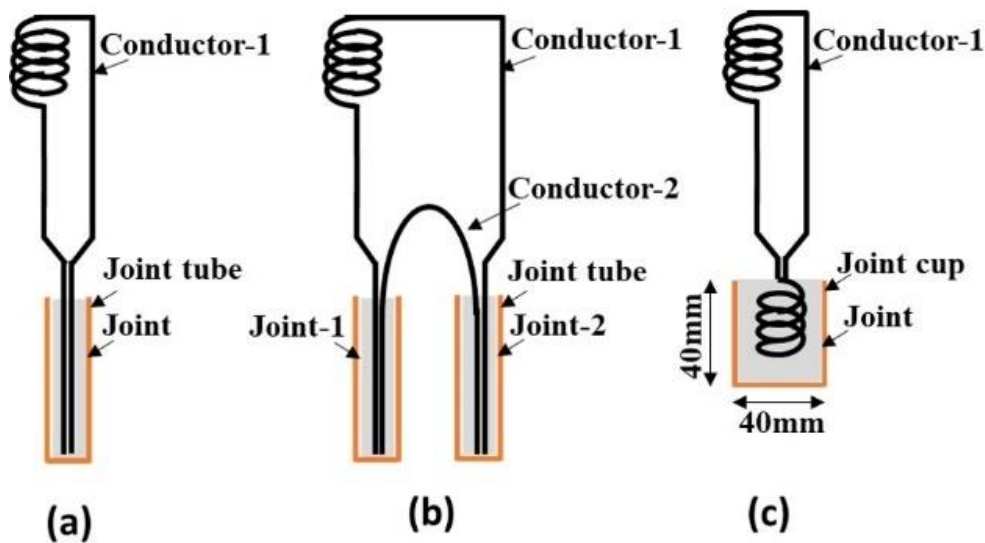


Figure 3.21 Schematic representation of the configuration of (a) a single straight joint between two ends of the secondary coil or the test coil, (b) two straight joints between two pairs of ends of two different conductors, and, (c) spiral joint between two ends of a single conductor of the secondary coil.

Table 3.7 Parameters of the superconducting magnet.

Items	Value
Total No. of turns	3704
Wire Dia	0.55mm
Cu: NbTi	2:1
Inductance (L)	0.32 H
Room Temp. Resistance	12 $\Omega$
Magnetic Field at 53A	1.5 T
The diameter of the magnet bore	61mm
The outer diameter of the magnet	76mm
Length of the magnet	150mm

The outer diameter of the solenoid magnet is restricted by the inner diameter of the neck of the helium dewar. Fig.3.22 (b) shows the position of the magnet in the 4 K insert and the field profile of the magnet along the vertical axis of the magnet.

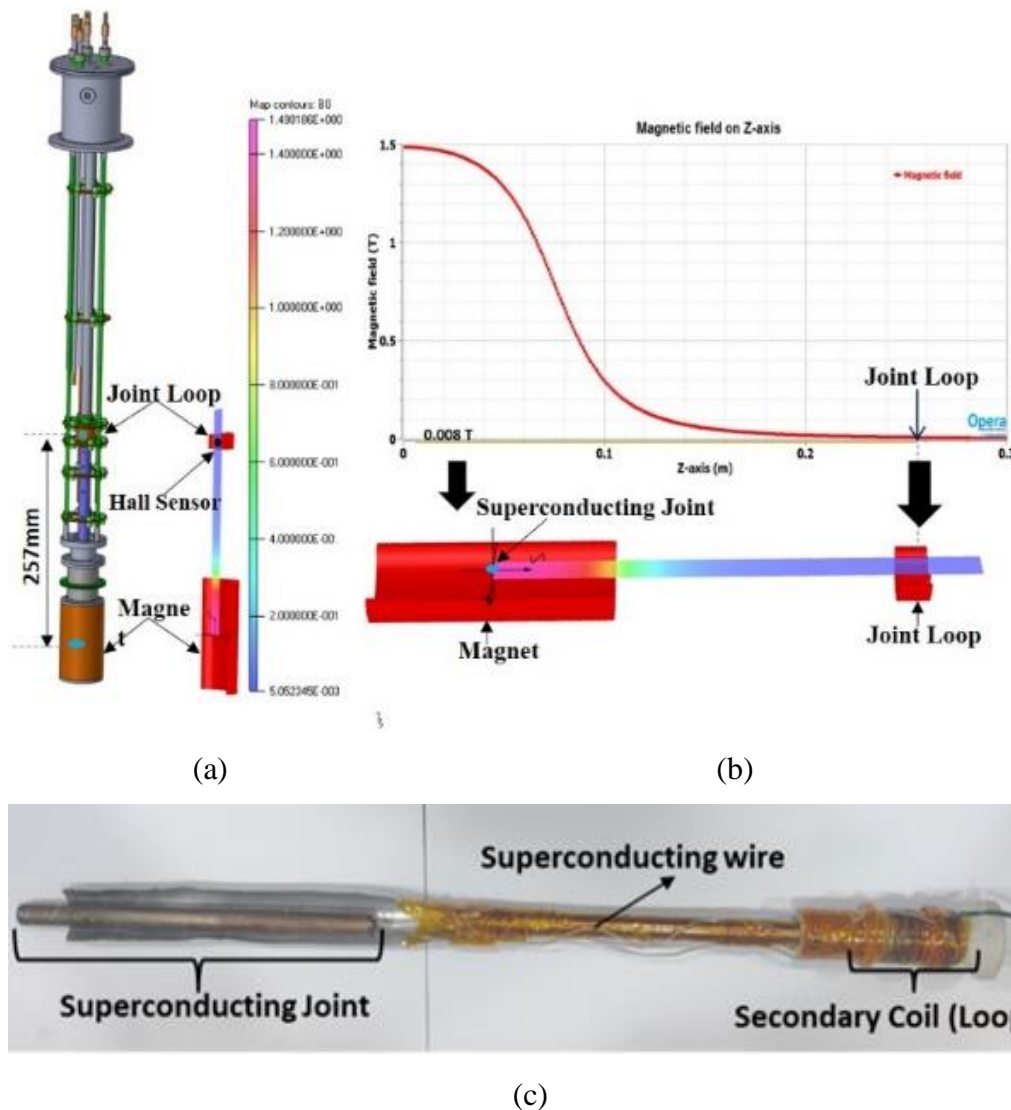


Figure 3.22 (a) The 3D model of the 4K insert along with the relative position of the 1.5 T solenoid magnet with respect to the secondary coil and, (b) the axial field profile of the 1.5 T solenoid magnet of the 4K insert, (c) the photograph of the sample joint having straight configuration.

The centre of the joint (straight or spiral) is placed at the center of the magnet to have the maximum background field during the testing. Whereas the joint loop or the secondary loop is located far apart ( $\sim 257$  mm) from the centre of the magnet thereby minimizing the effect of the stray field at the centre of the secondary coil or the test coil where the induced field is measured. At the 1.5 T background field, the stray field is 8 mT at the centre of the test coil. The magnet generates the background

field parallel to the axis of the magnet. Each joint is placed at the center of the magnet axially parallel to that background field. The primary coil and the magnet are connected to two separate magnet power supplies having the capacity to feed 160 A and 100 A current respectively. However, a single power supply having a capacity of 160 A can also be used for both the secondary coil and the magnet. A cryogenic hall probe with a Gaussmeter (Cryomagnetic, model LM-700) is placed at the centre of the primary coil to measure the decay of the induced field [12]. The inner diameter of the former of the secondary coil is sufficient to place the axial hall probe at the centre of the secondary coil. The Gaussmeter is connected to a laptop through the RS232 interface for the recording of the magnetic field data.

Fig.3.23 shows the picture of the top lid of the helium dewar with the vapor-cooled current leads, the instrumentation port, and the liquid filling port. The cryogenic heat inleak through the 4 K insert along with the heat flow through the neck tube of the dewar will determine the rate of evaporation of the liquid helium thereby determining the duration of the experimental measurement. Hence, the heat inleak needs to be minimized to have longer duration of the experiment without any refilling during the measurement. There is a vent port on the top lid of the dewar to vent the evaporated helium gas. The evaporated helium gas through the VCCL is also connected to the same vent port of the dewar. To minimize the heat inleak to the liquid helium, the heat flow to the liquid helium has been analyzed. The solid conduction through various components of the 4 K insert is the major contributor to the heat inleak. The conduction heat transfer through the GFRP support rods, the SS tube to hold the secondary coil in position inside the insert, the SS tube of the hall sensor, and the instrumentation leads (for the heater and the level sensor) will primarily be responsible for the heat conduction to 4.2 K. The governing equation for the heat conduction through each component is given the Eq. (3.7).

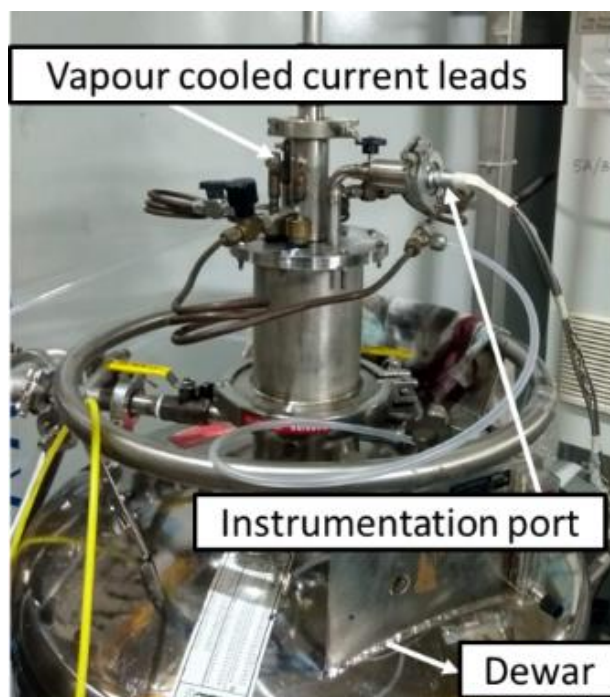


Figure 3.23 The photograph of the top lid of the helium dewar with the 4 K insert.

$$Q_{i,c} = \frac{A_i}{L_i} \int_{4.2}^{300} K_i(T) dT \quad (3.7)$$

Where  $Q$  (in W) is the heat conduction through the  $i^{\text{th}}$  component,  $A$  (in  $\text{m}^2$ ) and  $L$  (in m) are respectively the cross-sectional area of the  $i^{\text{th}}$  component through which solid head conduction takes place and length between 300 K and 4.2 K of the  $i^{\text{th}}$  component  $\int_{4.2}^{300} K_i(T) dT$  is the thermal conductivity integral of the  $i^{\text{th}}$  component between 300 K and 4 K. The cross-sectional area and the length of each component are calculated as per their dimensions summarized in Table 3.8. The thermal conductivity integral values of the GFRP, SS-304, and the sensor leads are taken from the references [112-113]. The estimated heat inleak is summarized in Table 3.8.

The heat inleak through the vapor-cooled current lead is calculated based on the optimized value of the heat flow i.e.,  $1\text{mW/A}$  [114]. The radiation heat inleak through the neck is negligible as there are multiple baffles at different heights of the 4 K insert. Hence, the total heat inleak to 4.2 K is 0.8 W which will evaporate 1.2 L of

liquid helium per hour. The helium dewar has its inherent heat evaporation of 1% liquid per day which is 0.042 L /hr. Hence, the total rate of evaporation of the liquid is ~ 1.25 L/hr. The heat inleak due to the energy dissipation through the heater during quenching of the secondary coil is not considered as it dissipates a momentary energy of 3.8 J. Such quenching is done only once during a single set of measurements. The static heat flow through the leads of the heater has been considered in the overall heat inleak calculation.

Table 3.8 Heat inleak to 4.2K through the 4K insert.

S/N	Item	Length(mm),Dia (mm)	Heatload (W)
1	GFRP rods (3)	606, $\phi$ 8	0.067
2	Hall probe sensor tube	800, OD-12.5/ID-10	0.168
3	SS tube	907, OD-19/ID-16.5	0.204
4	VCCL leads (2) of the primary coil (2),135A	-	0.27
5	VCCL leads (2) of the magnet (2). 25 A	-	0.05
6	Instrumentation leads.	-	0.05
	<b>Total Heat Inleak</b>	-	<b>0.809</b>

Fig.3.18 shows the complete test rig for the measurement of the electrical resistance of the superconducting joint. A safety relief valve is fixed at the neck of the helium dewar. During measurement, if the pressure of the helium bath increases beyond 5 psi due to the quenching of the magnet or the excessive energy dissipation from the current leads, and heaters, the helium vapour will be released into the atmosphere through the safety valve.



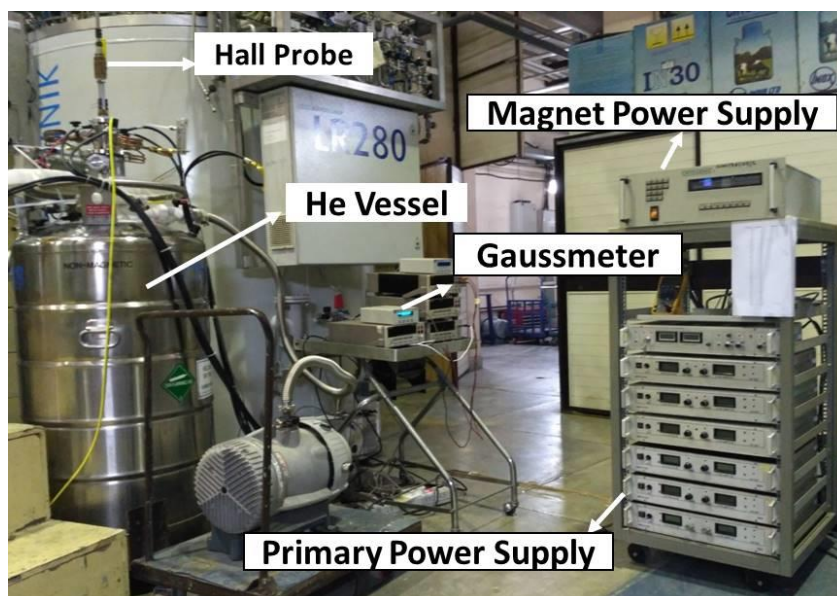


Figure 3.24 The photograph of the test rig for the measurement of the joint resistance using a 4 K insert probe.

### 3.12 Joint sample

As described in the section 3.11, the secondary coil is made of Cu-NbTi wire. In the case of a single conductor, two ends of the conductor of the secondary coil are joined using thornton's matrix replacement method. The joint is then embedded in a copper tube or cup filled with the superconducting solder as shown in Fig. 3.21(a) and Fig. 3.21(c). In the case of two different conductors, two joints are made which are then embedded in two separate copper tubes filled with superconducting solder as shown in Fig. 3.21(b). The superconducting joints made by using any other standard techniques; ultrasonic welding, diffusion welding, cold-pressing, and spot welding can be characterized using this 4 K insert. The shorted secondary coil is then mounted on the 4 K insert by placing it concentrically and coaxially to the superconducting primary coil.

### 3.13 Measurement process

The measurement process is started once the 4 K insert with the test coils is cooled to 4.2 K using liquid helium inside the dewar. It has various intermediate steps prior to starting the measurement of the field decay. Fig.3.25 shows the schematic representation of each step. There are five major steps described below:

1. Ramp up the superconducting primary coil at a certain ramp rate up to the desired current ( $I_p$ ) which will generate the primary field ( $B_p$ ). The change in magnetic flux in the primary coil will induce the current ( $I_s$ ) into the secondary coil or the test coil in the opposite direction to generate a secondary field ( $B_s$ ).
2. The cryogenic hall probe measures the resultant field ( $B_p + B_s$ ) at the centre of the secondary coil. A heat pulse of  $\sim 1.9$  W is given to the secondary coil for 2s through the heater wire ( $I_h = 0.25$ A) to quench. Thereby, the induced current reduces to zero ( $I_s = 0$ ) as shown in Fig.8. The hall probe measures the primary field ( $B_p$ ).
3. Ramp down the primary coil to zero ( $I_p = 0$ ) at a certain ramp rate. The change in the magnetic flux by the primary coil will again induce the current ( $I_s$ ) into the secondary coil or the test coil in the opposite direction to generate the secondary field ( $B_s$ ).
4. The primary field ( $B_p$ ) is reduced to zero whereas the secondary field ( $B_s$ ) is generated. The hall probe measures the secondary field ( $B_s$ ).
5. Measure the decay of the secondary field ( $B_s$ ) using the hall probe. Initially, the decay is measured at the zero-field (ZF). Once the decay rate is stabilized at ZF, the magnet at the bottom is energized to measure the decay rate in the presence of the background field.

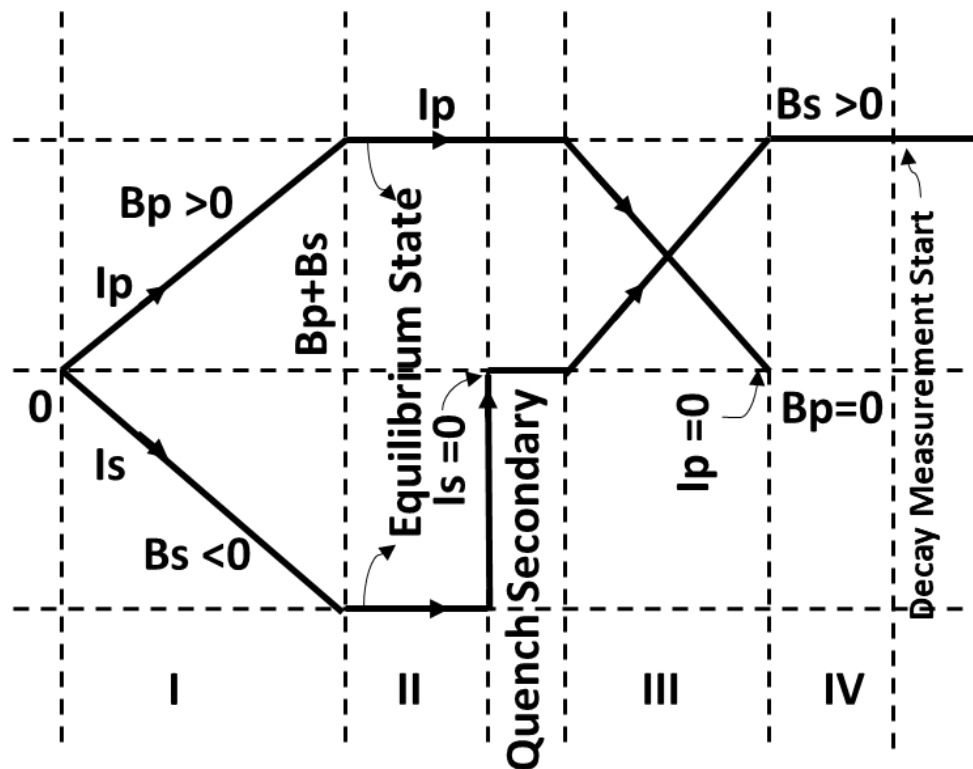


Figure 3.25 The schematic representation of the major steps for the measurement of the joint resistance using a 4 K insert probe.

### 3.14 Results and discussion

Fig.3.26 shows the variation of the magnetic field at the centre of the primary and the secondary coil during the process of current induction in one of the test coils or the secondary coil using the 4 K insert. Table 3.9 shows the various parameters during the testing of two separate joints. In set-1, the joints have been made between two conductors; Cu-NbTi and CuNi-NbTi using the configuration shown in Fig.3.21(b). In set 2, the joint has been made using a single conductor. The primary coil in set-1 is ramped up to 135 A of current. At the steady state, the resultant field, ( $B_p + B_s$ ) is measured to be  $\sim 54.5$  mT. At the ideal condition i.e. with the 100% coupling of the flux between the primary and the secondary coil, the total field will be zero. The non-zero resultant field signifies the partial coupling which is discussed in section 3.11. The secondary coil is then quenched by 0.25 A of current to the wire heater as indicated

in Fig.3.26. After quenching of the secondary coil, the field at the centre is only due to the primary coil which is 0.43872 T. The current through the primary coil is then ramped down to zero to again induce the current into the secondary coil. When the primary current reaches to zero, the field measured at the centre is only due to the secondary coil which is 0.38510 T. The secondary field slowly decays over the time which is measured for calculating the joint resistance. The secondary field corresponds to the 525 A of the induced current in it which signifies 3.9 times higher current induction than the primary coil. At 160 A of primary current, almost 620 A current can be induced into the secondary coil. It almost takes  $\sim 1000$  s to complete one cycle of current induction into the secondary coil. The decay measurement can be started after that.

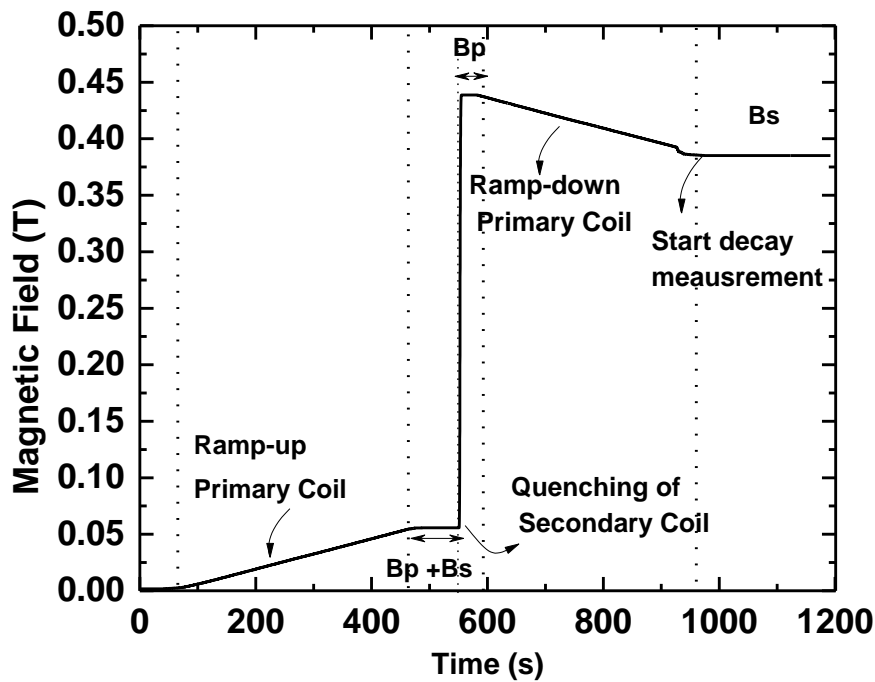


Figure 3.26 The variation of the magnetic field with the time during the process of current induction into the secondary coil using the 4 K insert.

Table 3.9 Parameters of the two sets of measurement.

<b>Parameter</b>	<b>Set-1 Cu-(NbTi)-CuNi-(NbTi)</b>	<b>Set-2, Cu-(NbTi)-Cu-(NbTi)</b>
$I_P$	135 A	135 A
$B_p + B_s$	54.72 mT	60.1 mT
$I_H$	250 mA	250 mA
$B_p$	0.43872 T	0.44143 T
$B_s$	0.38510 T	0.38143 T
$I_s$	~525 A	~520 A

In the beginning, the field decay is faster due to the transient settling phenomenon to redistribute the current over the superconducting filaments. The decay measurement is continued till the steady state value of joint resistance is reached. It takes almost an hour to reach the steady state value. However, any long-term measurement if needed can be done using this 4 K insert without any refilling of the liquid helium Fig.3.26 shows one such long-term measurement of the secondary field for a different joint sample. The measurement was continued for 450 min till it was quenched intentionally using the heat pulse through the wire heater.

After reaching the steady state value of the joint resistance at the zero background field (ZF), the solenoid magnet is energized up to the desired current to generate the background field that is parallel to the joint. In the beginning, the field decay is again faster due to the transient settling phenomenon to redistribute the current over the superconducting filaments in the presence of the background field. The background field is maintained at a constant value till the field decay reaches the steady state value. Once the joint resistance reaches the steady state value at that background field, the current to the magnet is increased to the next higher level. Fig.3.27 shows the steady state values of resistance of a superconducting joint at the different background magnetic fields. At zero field, the electrical resistance is  $\sim 8 \times 10^{-15} \Omega$ . The steady-state values of the electrical resistance have been measured at 0.5 T, 0.7 T, 1.0 T, and 1.2 T background field as shown in Fig.3.28. It is observed that the resistance of the joint deteriorates at the higher field. The electrical resistances are  $1 \times 10^{-14} \Omega$  and  $3.5 \times 10^{-14} \Omega$  respectively at 0.5 T and 1 T of background field.

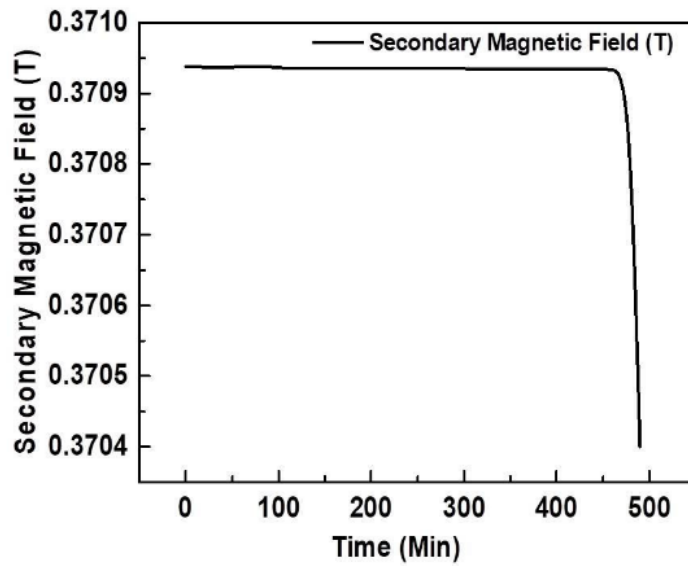


Figure 3.27 The long-term measurement of the decay of the secondary field using the 4K insert.

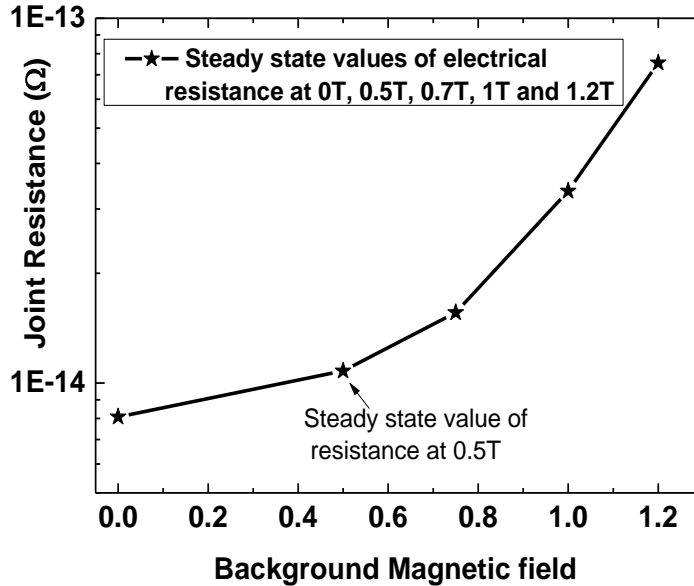


Figure 3.28 The steady-state values of the joint resistance were calculated from the field decay at various background fields using the 4 K insert.

### 3.15 Characterization techniques

In this thesis work, scanning electron microscopy (SEM) and energy-dispersive X-ray spectroscopy (EDX) techniques were utilized for sample characterization. These techniques provide valuable insights into the structural and elemental composition of the samples under investigation. The tools used for these characterizations are presented in the following subsections.

#### a) Scanning Electron Microscopy (SEM)

SEM is a powerful imaging technique used to observe the surface morphology of materials at high magnification. It works by scanning a focused beam of electrons across the sample's surface, generating signals that can be used to produce images with exceptional detail. The electron beam interacts with the atoms in the sample, resulting in various signals such as secondary electrons, backscattered electrons, and characteristic X-rays, which are detected and used to construct the image. SEM allows researchers to visualize surface features, topography, and even internal structures of samples with nanometer-scale resolution.

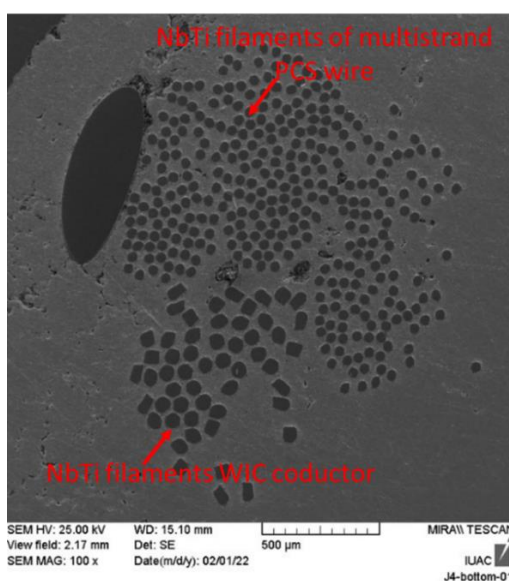


Figure 3.29 SEM image of the failed WIC to PCS wire joint.

To investigate the structure within the joint, several images of the failed joint were taken to determine the cause of the failure. Figure 3.29 shows one of the images of the failed WIC to PCS wire joint. Upon examining the image, we can observe that there is a significant gap between each filament. This gap indicates that the filaments are not properly connected. The increased spacing between the filaments leads to a longer current transfer path. This extended path can result in higher resistance values, which may contribute to the overall degradation of the joint over time. Furthermore, the image clearly shows that the WIC and PCS wire filaments are completely separated from each other. This separation is the main reason for the joint failure, as it prevents the proper transfer of current and compromises the structural integrity of the joint.

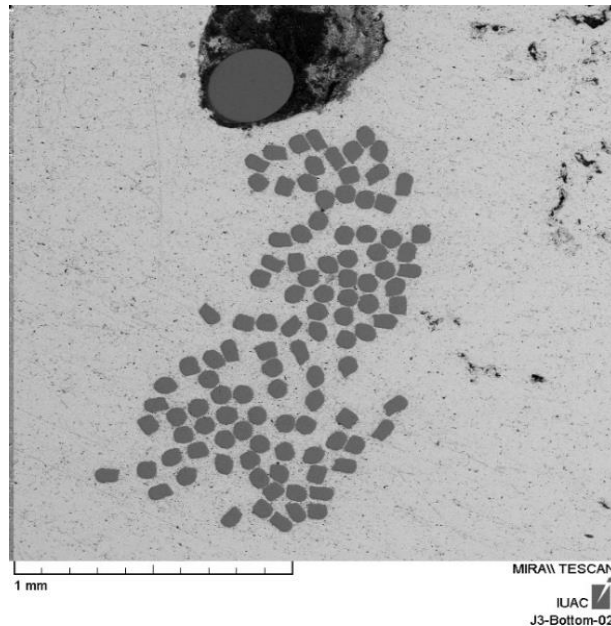


Figure 3.30 SEM image of the failed WIC to WIC wire joint.

Fig. 3.30 clearly shows that the WIC and WIC wire filaments are completely separated from each other. This separation is the primary reason for the joint failure, as it hinders the proper transfer of current and compromises the structural integrity of the joint.

In Fig. 3.31, it can be seen that one strand of the PCS wire has a copper section that is not completely tinned. This strand, located at the center of the bunch, did not



receive sufficient tin solder. As a result, the copper did not dissolve into the tin, affecting the overall joint resistance. Therefore, it is crucial to meticulously check the tinning process and duration when implementing the WIC and PCS joint. Additionally, it is essential to change the joint location and frequently shake the joint during the tinning process to ensure proper tin distribution throughout the joint.

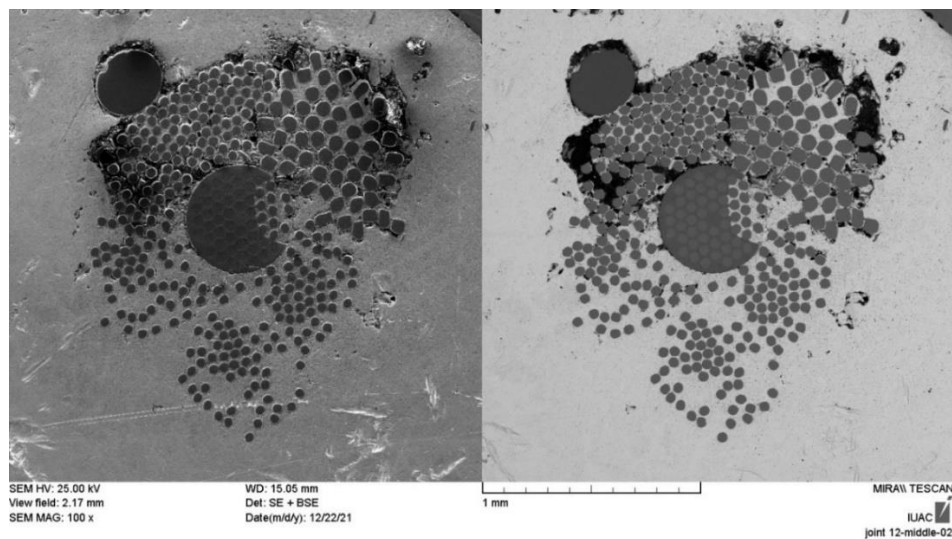


Figure 3.31 SEM image of the failed WIC to PCS wire joint.

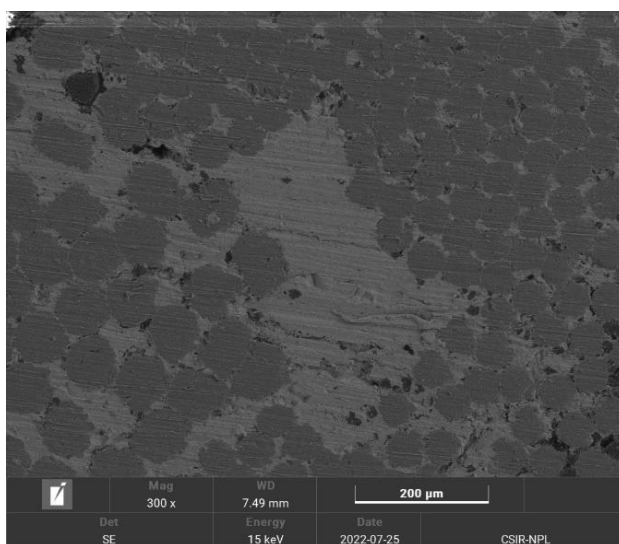


Figure 3.32 SEM image of the successful WIC to PCS wire joint.

Fig. 3.32 shows a successful WIC to PCS joint. By comparing Fig. 3.32 with other Fig. 3.29 - 3.31, the reason behind the joint failure becomes clear. The closer the filaments are to each other, the better the joint resistance will be.

b) Energy-dispersive X-ray Spectroscopy (EDX):

Energy Dispersive X-ray Spectroscopy (EDX) is an analytical technique often coupled with Scanning Electron Microscopy (SEM) to provide elemental composition analysis of materials. The technique operates by detecting characteristic X-rays emitted from a sample when it is bombarded with high-energy electrons from the SEM. Each element emits X-rays at specific energies, which allows for the identification and quantification of the elements present in the sample. EDX offers valuable information about the elemental composition, distribution, and concentration of elements within the sample.

c) Analysis of Failed Joints

In our study, EDX was utilized to analyze failed joints to understand the underlying reasons for their failure. Fig.3.33 presents the EDX analysis of one such failed joint. The analysis was conducted on both the filament and solder sections, each covering half of the area under examination. The Table 3.10 accompanying Fig. 3.33 reveals the presence of various impurities within the solder (Like Cu and AL). However, the exact source of these impurities remains unclear.

One possible explanation for the impurities is the use of a stainless steel (SS) solder bath. It is hypothesized that excessive heating of the SS bath may have introduced contaminants into the solder, leading to the observed impurities. This initial observation suggests that these contaminants significantly affected the joint's performance, resulting in failure. Further supporting this 3.34 also depict failed joints, each exhibiting different impurities. The consistency of impurity presence across multiple samples implies the need to address this issue to enhance joint performance and reliability.

#### d) Innovative Solution for Maintaining Solder Purity

To mitigate the contamination problem, we implemented a solution focused on maintaining the purity of the solder. As illustrated in Fig. 3.15, a glass tube was employed to contain the solder during the heating process. This glass tube was then placed in the SS bath, ensuring that the solder did not come into direct contact with the bath itself. By isolating the solder within the glass tube, the introduction of contaminants from the SS bath was effectively prevented.

#### e) Results of the Glass Tube Method

The results of implementing the glass tube method are demonstrated in Fig. 3.35. The table associated with this figure shows that there are no impurities present in the joint, aside from the filament and solder materials. This absence of impurities can be directly attributed to the use of the glass tube, which maintained the purity of the solder during the heating process.

The impact of this method on joint performance is significant. As a result of eliminating impurities, the joint resistance increased to the expected value, indicating a substantial improvement in performance. This outcome highlights the effectiveness of isolating the solder from potential contaminants in the SS bath, ensuring a cleaner and more reliable joint.

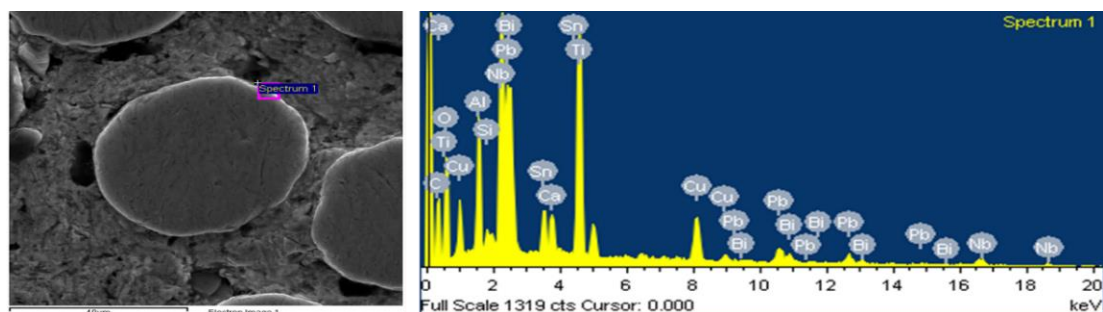


Figure 3.33 SEM image of the failed WIC to PCS wire joint.

Table 3.10 Details of the material present in the WIC to PCS joint.

Element	Weight%	Atomic %
Ti K	11.30	6.06
Cu K	5.71	2.85
Nb L	42.37	48.78
Sn L	4.22	0.91
Pb M	25.47	36.79
Bi M	10.62	4.77
<b>Total</b>	<b>100.00</b>	

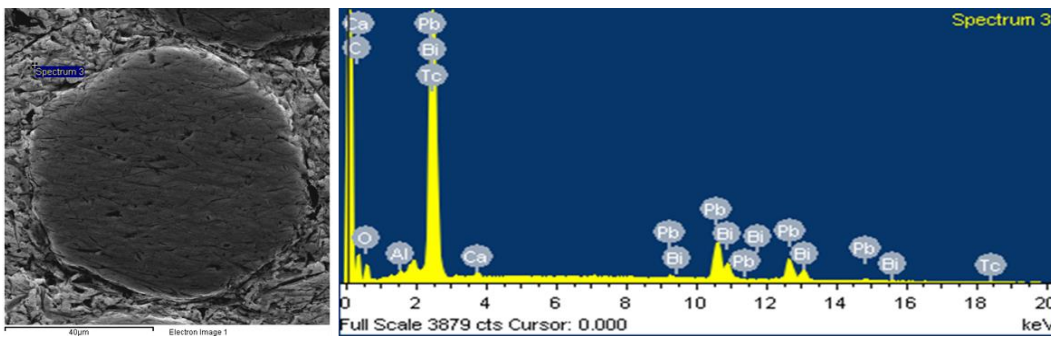


Figure 3.34 SEM image of the failed WIC to WIC wire joint.

Table 3.11 Details of the material present in the WIC to WIC joint.

Element	Weight%	Atomic %
C K	22.28	61.18
Ti L	22.92	28.60
Pb M	40.14	6.39
Bi M	14.22	3.11
<b>Totals</b>	<b>100.00</b>	

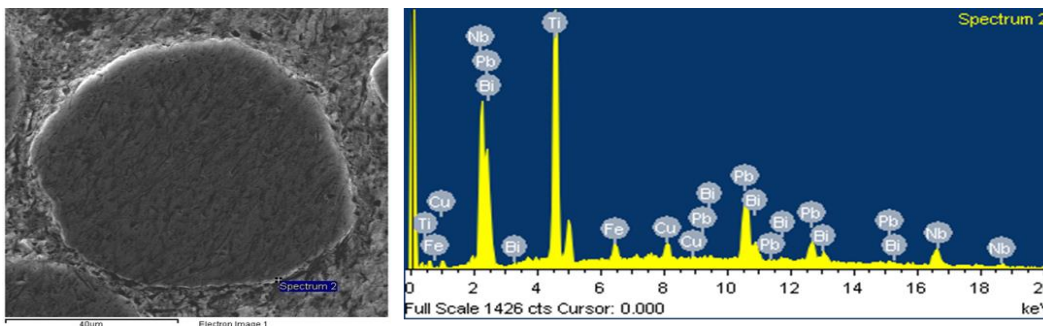


Figure 3.35. SEM image of the successful WIC to WIC wire joint.

Table 3.12 Details of the material present in the WIC to WIC joint.

Element	Weight%	Atomic %
Ti K	42.35	60.23
Fe K	4.34	5.30
Nb L	36.85	27.05
Pb M	14.49	4.76
Bi M	1.96	0.64
<b>Totals</b>	<b>100.00</b>	

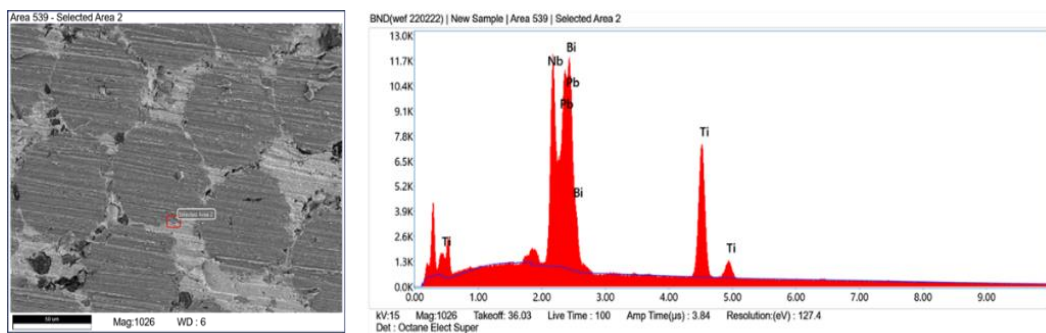


Figure 3.36 SEM image of the successful WIC to PCS wire joint.

Table 3.13 Details of the material present in the WIC to PCS joint.

Element	Weight%	Atomic %
Ti K	20.57	45.11
Nb L	23.61	26.69
Pb M	32.82	16.64
Bi M	23.01	11.56
<b>Totals</b>	<b>100.00</b>	

Through EDX analysis, the time required for the tinning process was determined by examining the copper content in the joint cup. EDX was performed on different joints where tinning was applied at approximately 300°C for varying time spans. The analysis led to the conclusion that tinning at 300°C for three hours is sufficient to remove all copper from the surface of the filaments.

### 3.16 Summary

This chapter provides an in-depth discussion of the joint-making process for superconducting joints, with a focus on critical parameters and techniques to ensure high quality. The development of a versatile 4 K insert for characterizing superconducting joints, achieving the lowest electrical resistance of  $8 \times 10^{-15} \Omega$  at zero field and the ability to induce up to 525 A in the secondary coil. SEM and EDX analyses identified impurities from excessive heating of the SS solder bath as a major cause of joint failure. To address this, an innovative glass tube method was implemented to maintain solder purity, significantly improving joint performance and resistance. The chapter discusses the importance of material purity, precise process control, and innovative problem-solving in achieving reliable and efficient superconducting joints, laying the groundwork for further advancements in this field.

## CHAPTER 4

### PERSISTANT CURRENT SWITCH

#### 4.1 Introduction

The superconducting magnets generate a strong magnetic field, which would otherwise be impossible with conventional, normal electromagnets. The practical application of superconductors in MRI stands as one of the most significant contributions to mankind. The whole-body clinical MRI scanners need a highly homogeneous magnetic field and a highly stable field in the imaging volume. Any deviation in the magnetic field can alter the resonance frequency of hydrogen ions undergoing resonance, consequently introducing artifacts into the resulting image. The magnet needs to provide a temporal field stability better than 0.1 ppm/hr, i.e., 15  $\mu\text{T/hr}$  for a 1.5 T magnet, which is only possible through a persistent circulation of the current through the coils of the magnet shorted through a PCS. Because such high temporal field stability is difficult to achieve by any commercially available power supply employing a direct current (DC). This difficulty stems from the presence of minute alternating current (AC) ripples within the DC current and their fluctuations. Moreover, the continuous supply of current can incur substantial operational costs due

to the joule heating on the current leads, potentially leading to LHe evaporation. To circumvent these issues, superconducting magnets in MRI systems operate in persistent mode, where the current flows in a closed-loop configuration [48, 62 - 64]. The PCS across the superconducting coils makes it possible to operate in the persistent mode to achieve the desired temporal field stability of the MRI magnet [62 – 64].

In this chapter, the design parameters of the PCS are discussed in detail along with its analytical calculation of total energy dissipation. Thermo-foil heaters are used at various intermediate layers of the winding pack of the epoxy-impregnated switch to study the thermal behavior in correlation with the location of heaters inside the winding layer. Also, a comparative analysis of the temperature profile along with its switching behavior is discussed for the thermo-foil resistors located at the various layers of the PCS. The normal resistance has been measured across the PCS at various temperatures.

## **4.2 Operation of a PCS**

The PCS has two essential elements:

- a). A superconducting link, to complete the circuit after removing the power supply.
- b). A method of rendering the link unusable

The link needs to be a superconductor in parallel with, or in place of, the power supply. The means of destroying the link could be mechanical (a physical breaking of the link) but mechanical systems can have many complications due to the cryogenic conditions. It is more usual to have the link fixed in place and to force the superconductor into a normal resistive state. The current will, to a high degree, ‘ignore’ the resistive path, and hence the link will essentially be ‘broken’. A superconductor can be made normal by exceeding any of its critical parameters. A sufficiently large magnetic field, current density, or temperature will revert the superconductor to its



normal state. For a PCS used in a superconducting magnet system, it is usually the temperature that is the control used in the operation of the PCS.

In the magnet circuit, the PCS is connected electrically in parallel with both the superconducting magnet and the ramping power supply. Fig.4.1 provides a schematic diagram of the circuit where the arrow's direction represents the current flow's positive direction.

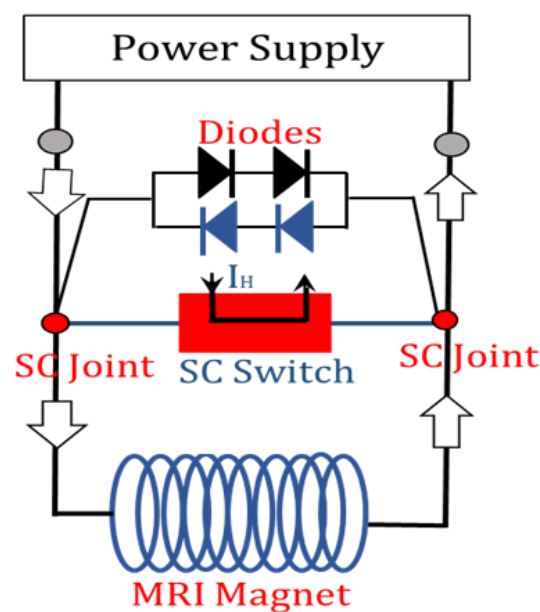


Figure 4.1 Persistent mode operation of MRI magnet

The superconducting magnet is initially charged to the required operating current using a high-current power supply. After achieving the desired magnetic field, the magnet terminals are shorted using the PCS. The PCS is responsible for maintaining the resistive state or OFF state during the ramping process. Once the magnet reaches its desired field strength for operation in the persistent mode, the PCS is switched to the superconducting state or ON state by switching OFF the Film heater. This allows the operating current to circulate through the superconducting electrical circuit the flow chart shown in Fig.4.2 summarizes the operational sequences of the MRI magnet before parking the magnet at a desired field. [115]

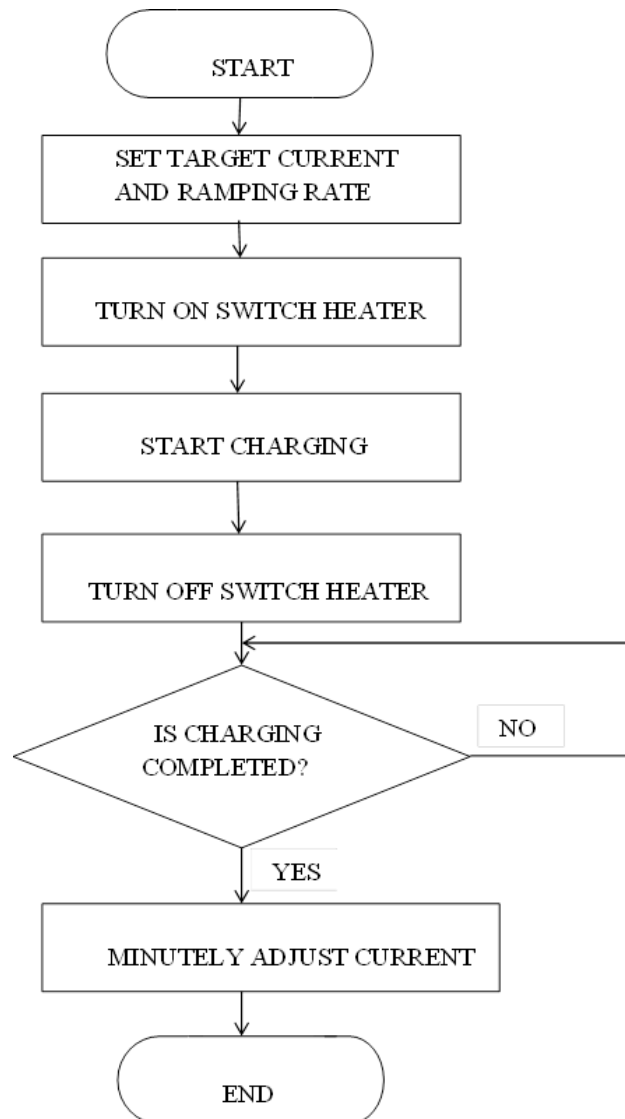


Figure 4.2 Algorithm for the operation of the PCS and power supply.

### 4.3 Issues with the PCS

a) PCS testing: PCSs are typically tested for current capacity and inductance. However, it's been observed that soldering the PCS wires into the test insert can harden them, leading to a failure rate of about 1 in 10 when installed in a magnet.

b) PCS instability: PCSs can break open spontaneously, thought to be due to flux jumping. This could be due to poor manufacturing quality of the PCSs, the background field or the lower stability of the CuNi matrix.

c) Response time: The response time for the PCS to open and close isn't critically important, but it should occur within seconds, rather than minutes or hours. However, in the case of a magnet quench, it's crucial for the PCS to transition to a resistive state as quickly as possible. This allows the protection resistors to offer a lower-resistance path and absorb the majority of the energy. Achieving both rapid opening and closing presents a challenge due to conflicting thermal insulation requirements. A compromise must be made, or alternatively, an active cooling system or adjustable insulation could be used. Prioritizing fast opening is likely more essential.

d) PCS positioning: The positioning and orientation of the PCS need to be considered because the PCS will produce an unwanted magnetic field and also the background field in which it is situated will affect the current capacity and critical temperature of the PCS wire.

e) Number of heaters: Some PCSs are designed with two heaters, although only one is typically used during normal operation. The redundant heater introduces additional mass, which acts as a heat sink, absorbing heat that is meant to warm the PCS wire.

f) Heater positioning: The heater consists of several layers of windings. It is positioned in the middle layer and is surrounded by many layers of PCS wire. This situation is not optimal for heat transfer from the heater to the PCS wire.

g) The Bobbin: It is a cylindrical on which the wire is wound. Due to the magnet and the PCS being in cryostat containing liquid helium, the bobbin should made up of insulation materials such as glass fiber reinforced plastic (GFRP), Bakelite, polytetrafluoroethylene (PTFE), and so on. Bobbin made of SS can also be because of the lower conductivity of heat at low temperatures (4.2 K). In order to generate a small amount of heat during the ramp, the PCS should have high normal state resistance. The bobbin made of copper cannot be used because due to higher conductivity, a large amount of power needed to make the PCS OFF, and also heat

transfer by copper bobbin will boil off the liquid helium in large quantities. The thermal conductivity of copper is high at a lower temperature, Thus the time taken by the PCS to transform from normal state to superconducting state will be larger. Thus, slow recovery into the superconducting state and this slow recovery decreases the magnet's stored energy.

h) Normal state resistance: To minimize heat loss, the resistance of the PCS should be higher. This means that the normal state resistance needs to be large enough to limit the current passing through the resistive PCS. Essentially, there are two conditions that a PCS must meet [59]:

- The product of  $V_{ch}$  (charging voltage) and the reciprocal of  $R_{pcs}$  (PCS resistance) should not exceed 0.1 times the operating current ( $I_{op}$ ).
- The power dissipated by the PCS ( $V_{ch}^2/R_{pcs}$ ) should ideally be no more than 1 watt, or at most, a few watts.

i) Thermal insulation: The heat injected into the PCS to make the PCS resistive will act as a cryogenic load to the cryocooler. The recovery time and high efficiency in insulation layer thickness are fundamentally at odds with one another. On the one hand, a thin layer is ideal for quick recuperation and experiencing higher loss because it takes more energy to keep the PCS in a resistive state. To provide thermal insulation between the winding and liquid helium and prevent direct contact, we wrapped a few layers of glass cloth tape around the last layer of the PCS. The glass cloth tape is a suitable material for this purpose due to its insulating properties and ability to withstand high temperatures.

j) Stability and protection: The PCS are the essential component of the MRI magnet. If a PCS is damaged, it simply needs to be replaced. A serious problem happens if the PCS quench and magnet are in the superconducting state. In this case, the entire energy will be dumped into the PCS, which may cause burn out the PCS. To safeguard the PCS from such events, the diode bank will be connected across the PCS for protection.

#### 4.4 Design of the PCS

The PCS is made of the NbTi-Cu-30%Ni conductor having six strands with an overall diameter of 1.6 m [116]. Fig.4.3 shows the critical current curve of the CuNi-NbTi conductor with a different number of strands. The conductor has a critical current of more than 2 kA at 1 T. In the final application, the PCS will be placed at  $\sim 0.6$  T of the background field of the magnet.

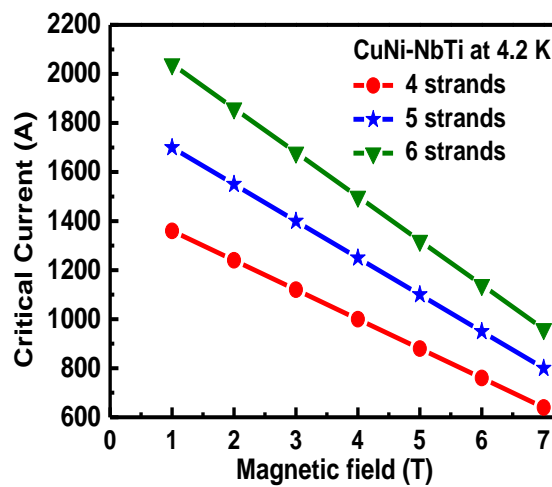


Figure 4.3 The critical current curve of the multi-strand CuNi-NbTi conductor [Bruker OST] [116].

The critical current of the conductor with four strands is 1.35 kA at 1T. The overall normal resistances per strand ( $R_{strand}$ ) of the conductor are  $2.49 \Omega/m$  and  $2.21 \Omega/m$  respectively at 300 K and 15 K. The strands of the conductor behave as parallel resistors as shown in Fig.4.4. The normal resistance ( $R_{PCS}$ ) of the PCS is estimated using Eq. (4.1);

$$R_{PCS} = \frac{R_{strand}}{n} \quad (4.1)$$

where,  $n$  is the number of strands.

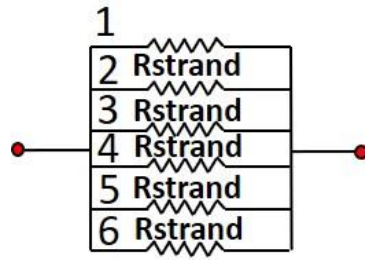


Figure 4.4 The equivalent resistance diagram of the six-strands CuNi-NbTi conductor where  $R_{strand}$  is the normal resistance of each strand.

Using Eq. (4.1), the resistance of the PCS conductor with 4, 5, and 6 strands are respectively estimated to be  $0.553 \Omega/m$ ,  $0.442 \Omega/m$ , and  $0.368 \Omega/m$  at 15 K. The critical current of the conductor used in the PCS at its background field needs to be at least 1.5 times higher than the operating current of the magnet to take care of any eventuality. Hence, the critical current and its associated normal resistance can be chosen by selecting an appropriate number of strands that to be used for connecting the magnet for its persistent operation.

During the ramp-up of the magnet, the PCS will be at the resistive state until the magnet reaches the desired field. A finite amount of current would flow through the PCS during the ramp-up of the magnet. Hence, there will be an energy dissipation into the PCS during the ramp up of the magnet which would eventually result in evaporating the liquid helium. The total energy ( $Q_T$ ) dissipated into the PCS is calculated by using Eq. (4.2);

$$Q_T = Q_H + Q_C \quad (4.2)$$

Where,  $Q_H$  is the dissipated energy into the PCS heater and,  $Q_C$  is the dissipated energy into the PCS at its *OFF* state due to the charging voltage of the magnet,  $V_C$ . Eq.(4.3) can be expressed as;

$$Q_T = I_H^2 R_H + \frac{V_C^2}{R_{PCS}} \quad (4.3)$$

Where,  $I_H$  is the current to the PCS heater,  $R_H$  is the value of the electrical resistance of the heater, and  $R_{PCS}$  is the value of normal resistance of the PCS at its resistive state i.e. *OFF* state. The relation between the normal resistance of PCS and the energy losses is defined in Eqs. (4.4)-(4.6) [60 – 70].

$$E_R = \frac{2E_0L}{Rt} \quad (4.4)$$

$$P_{loss} = \frac{E_R}{E_0} \times 100 \% \quad (4.5)$$

$$R_{PCS} \geq \frac{200L}{P_{loss} \times t} \quad (4.6)$$

where,  $E_R$  is the total energy losses in the PCS,  $E_0$  is the total stored energy of the magnet,  $L$  is the self-inductance of the magnet which is 42H in our case, and  $P_{loss}$  is the percentage of energy loss in the PCS during the ramp-up of the magnet.

At the time of ramping of the MRI magnet, as soon as the PCS becomes resistive (*OFF* state), the power supply is activated, and the magnet is ramped using voltage  $V_c$ . The voltage magnitude is dependent on the magnet's inductance ( $L$ ) and ramp rate as shown in the Fig. 4.7

$$V_c = L \frac{dI}{dt} \quad (4.7)$$

If the charging voltage is 6 V, and the magnet has an inductance of 42 H and a current of 450 A, it would take approximately 2940 seconds (49 minutes) to ramp up to the desired field of 1.5 T. A finite amount of current would flow through the PCS during the ramp-up of the magnet, even when it is in its *OFF* state. Hence, there will be an energy dissipation into the PCS during the magnet's ramp-up, eventually evaporating the liquid helium.

The energy loss,  $E_s$ , is generated in the PCS at the time of magnet ramping. Hence, to charge the superconducting magnet up to the target energy,  $E_0$ , we must apply the energy  $E_0+E_s$ . The ratio of energy loss is represented as [63]:

$$\frac{E_S}{E_0} = \frac{R_S \times I_S^2 \times t}{\frac{1}{2} \times L \times I_0^2} = \frac{2 \times L}{R_S \times t} \quad (4.8)$$

To reduce the liquid helium boiloff at the time of charging, it is important to minimize the sources of energy loss as much as possible. The optimal length of PCS to limit the energy loss below the  $x\%$  value will be calculated using the following equation.

$$l_S = \frac{200 \times L \times A_S}{x \times t \times \rho_S} \quad (4.9)$$

$$\frac{E_S}{E_0} \times 100 = x\% \quad (4.10)$$

Where  $l_S$  is the length of PCS,  $A_S$  is the cross-section area of PCS wire,  $I_0$  is the operating current of the magnet,  $I_S$  is the current through PCS at OFF state, and  $\rho_S$  is the normal resistivity of PCS conductor.

Fig.4.5 depicts the relationship between the energy loss ratio and wire length. A conductor with a diameter of roughly 1.70 mm is used for PCS design. The conductor has an area of  $2.26 \times 10^{-6} \text{ m}^2$ , and its room-temperature resistivity is  $9.26 \times 10^{-7} \text{ } \Omega \cdot \text{m}$ . According to eq. (4.5)- (4.9) in our situation, the PCS's 40-meter length showed a 0.17% energy loss ratio.

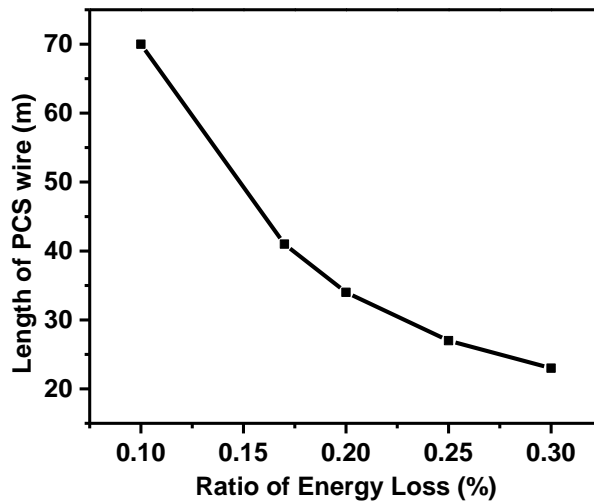


Figure 4.5 The length of the PCS wire vs the ratio of the energy loss.



Fig.4.6 shows the photograph of the PCS. The bobbin of the PCS is made of insulating material. The total length of the conductor used in the bifilar winding is 40 m. The normal resistance of the PCS with the six-strand conductor is 16.6  $\Omega$  and 14.6  $\Omega$  respectively at 300 K and 15 K. For this experimental study, all the six strands of the conductor were used to generate the design parameters for the final PCS. The bifilar winding technique is utilized to achieve the low inductance ( $\sim 6.6 \mu\text{H}$ ) necessary to have minimum field perturbation. The parameters of the PCS are summarized in Table I. The winding pack of the PCS is impregnated with Sytcast 2850 FT epoxy mixed using catalyst 24. Two thermo-foil polyimide heaters having electrical resistance of 90  $\Omega$  each were placed between the layers of the winding of the PCS.

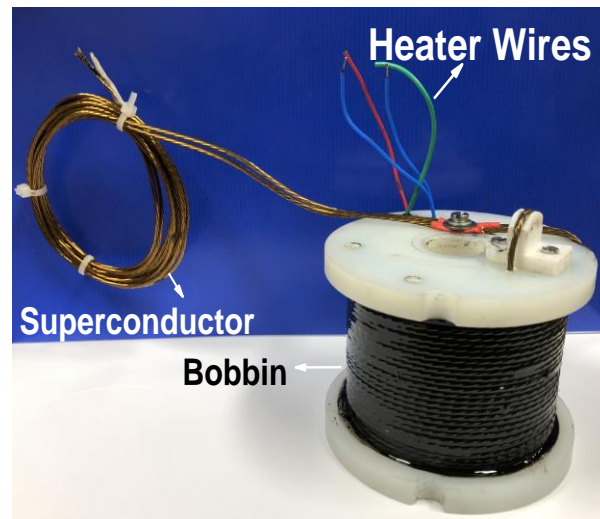


Figure 4.6 The prototype PCS developed for the 1.5T MRI magnet.

Table 4.1 Design parameters of the PCS.

<b>Parameter</b>	<b>Value</b>
No. of layer	8
Total no of turns	264
Turns per layer	33
Total wire length (m)	40
Normal Resistance ( $\Omega$ ) at 300K	16.6
Inductance ( $\mu\text{H}$ )	6.6

#### 4.5 Experimental test setup

Fig.4.7(b) shows the simplified of the experimental test setup. The thermo-foil polyimide heaters (FH1 and FH2) were connected to the heater power supply (Keithley 2450). During the ramp-up of the MRI magnet as shown in Fig. 4.7(a), at the charging voltage ( $V_c$ ) of 6 V, the current through PCS, ( $I_{PCS}$ ) is 0.41 A if the normal resistance of the PCS is  $14.6 \Omega$  at 15 K. Hereinafter, the current through the PCS during ramp-up will be referred to as ‘PCS current’. Hence, during the testing, the PCS is energized with 100-500 mA current ( $I_{PCS}$ ) at its OFF state i.e., resistive state using a power supply (Kepco, 72V/6A). The voltage and the temperature of the PCS were respectively measured using a digital voltmeter (Keithley 2000) and a temperature monitor (Model 218, Lakeshore Cryotronics Inc.). The temperature and the corresponding voltage profile were recorded using a laptop for analysis of the behavior.

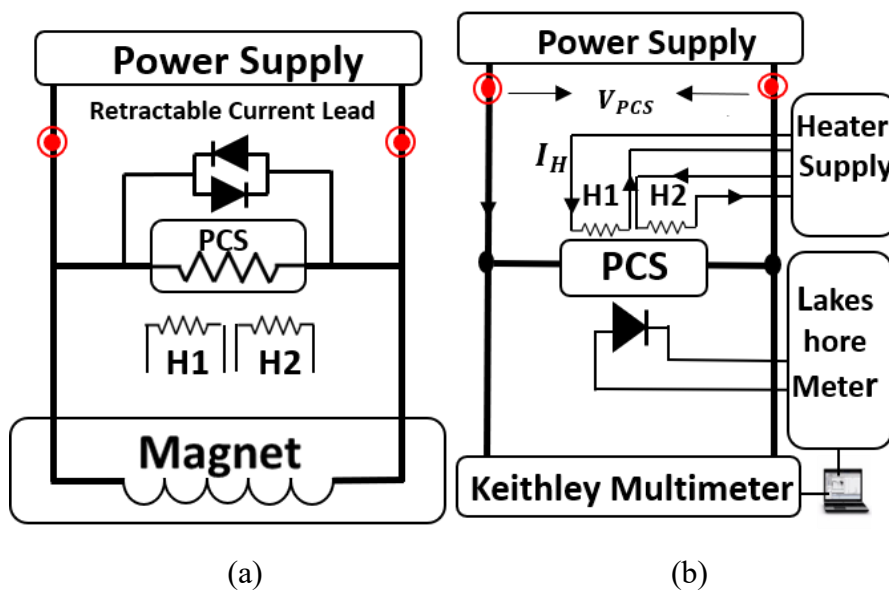


Figure 4.7 (a) A simplified electrical schematic of the superconducting magnet with the PCS and, (b) the schematic of the measurement test setup.

The film heater-1 (FH1) is placed between the 2<sup>nd</sup> and 3<sup>rd</sup> layer and the film heater-2 (FH2) is placed between the 5<sup>th</sup> and 6<sup>th</sup> layer. A few layers of fiberglass cloth were wrapped on the last layer of the PCS to thermally insulate the winding from direct

contact with the liquid helium. A calibrated silicon diode (DT-670, Lakeshore Cryotronics Inc.) temperature sensor is fixed onto the intermediate layers of the PCS to monitor its temperature. Fig. 4.6(a) shows the simplified schematic of the electrical connection of the superconducting magnet with the PCS. During the ramp-up of the magnet, the PCS must be “open” i.e., *OFF* state which is achieved by making the PCS resistive. It must be “closed” i.e., *ON* state for persistence operation which is achieved by making the switch superconducting.

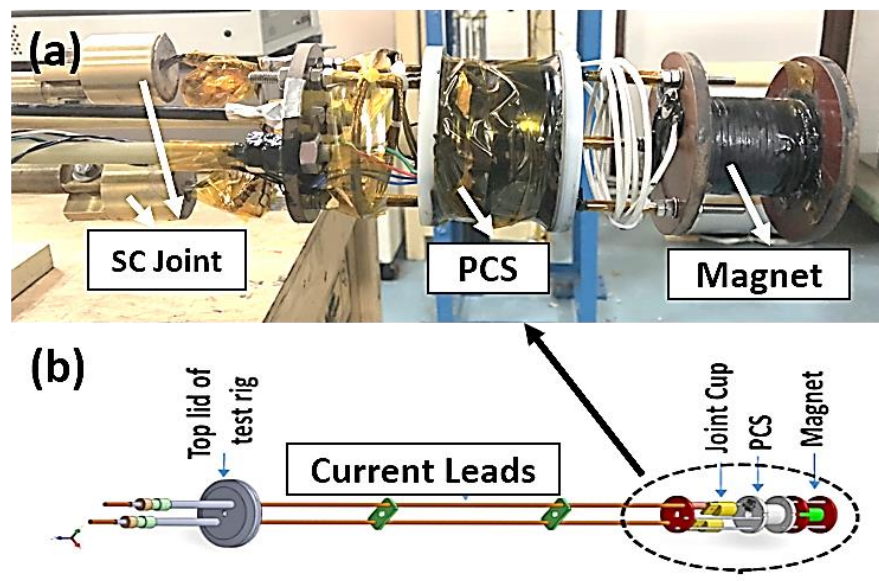


Figure 4.8 (a) The 4K rig for testing the PCS and, (b) the schematic representation of the 4 K rig used for the thermal and electrical characterization of the PCS.

Fig.4.8 (a)-(b) respectively show the photograph and the schematic of the 4 K test rig developed for characterizing the thermal and electrical behavior of the PCS. It consists of a pair of current leads, two joint cups, and the PCS. The terminals of the current leads are connected to the PCS through the joint cups. The 4 K rig as shown in Fig.4.8(a) is inserted into a helium dewar for its testing at 4.2 K. During the testing of the PCS, the temperature and voltage of the PCS is initially measured at a certain value of heater power without energizing the PCS i.e. without sending any current through the PCS ( $I_{PCS}=0$ ) at its resistive state. This is referred to as the 1<sup>st</sup> cycle of each set of measurements. Similarly, in the 2<sup>nd</sup> cycle, the temperature and the

corresponding voltage of the PCS were measured at a certain value of heater power while energizing the PCS by sending a current ( $I_{PCS} > 0$ ) equivalent to the PCS current during the ramp-up of the magnet. The normal resistance ( $R_{PCS}$ ) of the PCS could be measured at the 2<sup>nd</sup> cycle of each measurement by measuring the voltage drop ( $V_{PCS}$ ) across it using Eq.(4.11).

$$R_{PCS} = \frac{V_{PCS}}{I_{PCS}} \quad (4.11)$$

## 4.6 Results and Discussion

### 4.6.1 Performance Analysis

The amount of heat required to increase the temperature of the PCS from 4.2 K to >10 K depends on the specific heat capacity, the mass of the material, and the thermal insulation between the PCS and the helium bath. The equation for calculating the amount of heat required to raise the temperature of the PCS is given by Eq.4.12 if the PCS is [70]:

$$Q_H = \int_{4.2}^{10} V C_V dT \quad (4.12)$$

$$C_V = \lambda_{NbTi} C_{NbTi} + \lambda_{CuNi} C_{CuNi} + \lambda_{insulation} C_{insulation} \quad (4.13)$$

$V$  is the volume of the PCS superconductor,  $C_V$  is the specific heat of the PCS superconductor. The  $C_{NbTi}$ ,  $C_{CuNi}$ , and  $C_{insulation}$  are the specific heat of NbTi, CuNi, and insulation materials, respectively, and  $\lambda_{NbTi}$ ,  $\lambda_{CuNi}$ ,  $\lambda_{insulation}$  is the volume fraction of NbTi, CuNi, and insulation materials occupying the total volume.

#### 4.6.2 Test Results

Fig.4.9 illustrates how the normal state resistance of the PCS changes with the heater current. At a heater current of 100 mA, the PCS is normally in the "OFF" state, whereas at 500 mA, the PCS resistance becomes saturated in a thermal equilibrium state under adiabatic conditions. The PCS temperature also indicates whether it is in the "ON" or "OFF" state. Before ramping, current flows into the heater, and the resulting heating power increases the temperature of the PCS. The relationship between the heater current and the temperature of the PCS is shown in Fig.4.10. This can be seen in the fact that at the same heater current, the temperature of the PCS is higher for FH2 compared to FH1. Furthermore, as the heater current increases, the temperature difference between FH1 and FH2 also increases, with FH2 consistently having a higher temperature. This implies that FH2 is more effective than FH1 at transferring heat to the PCS.

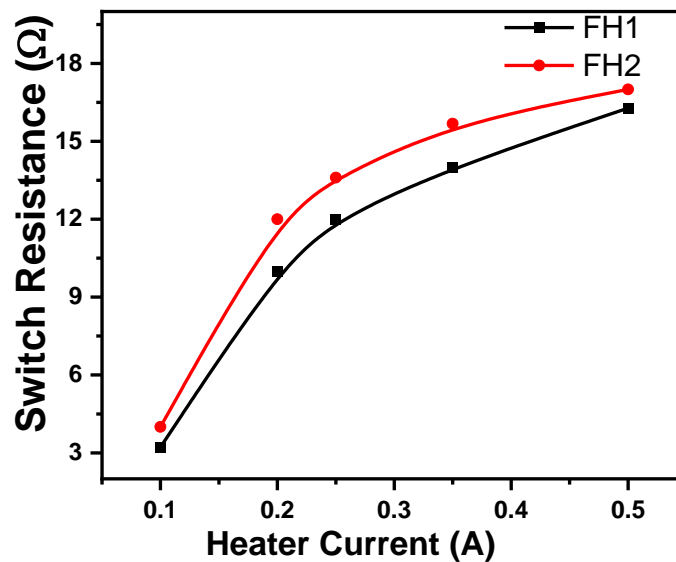


Figure 4.9 Normal resistance of the PCS for different heater currents.

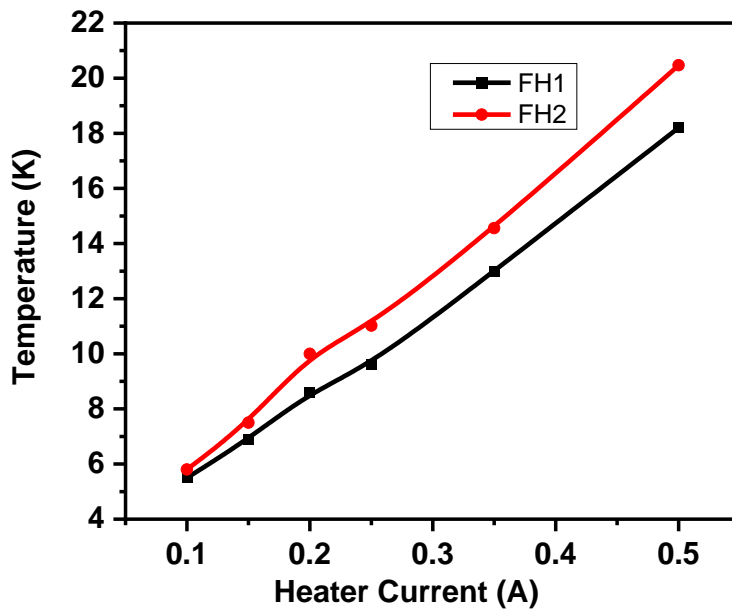


Figure 4.10 PCS temperature with respect to different currents.

Film heaters can offer certain advantages over wire heaters. Film heaters are typically made from a thin, flexible film that can be applied directly to a surface, making them easier to install. The film heaters also provide more uniform heating than wire heaters, as the heating element is distributed more evenly over the winding.

Fig. 4.11 and Fig.4.12 show the total heat dissipation in the PCS at various charging voltages respectively for FH1 and FH2. The dissipated heat in turn will be transferred to the liquid helium thereby will evaporate the liquid helium from the magnet vessel during the ramping of the magnet. The total power dissipation is calculated using Eq. (4.3) - (4.4).

Figs.4.11-4.12 shows a region with minimum heat dissipation for each of the ramping voltages. The ramping voltage is varied from a higher value at the beginning of the ramping to a lower value at the end of the ramping before parking the magnet at the desired field. It is to be noted that the PCS should have substantial normal state resistance to break the PCS circuit during the ramping up of the magnet. The minimum heat dissipation in the PCS at 10 K is about  $\sim 4$  W at 4 V of the charging voltage. This

can easily be achieved by applying a 250-mA current to the heater. At 250 mA of heater current with 6 V charging voltage, the overall power dissipation is  $\sim 6.5$  W. The PCS needs to be operated at the minimum region of the graphs shown in Fig.4.11 and Fig.4.12.

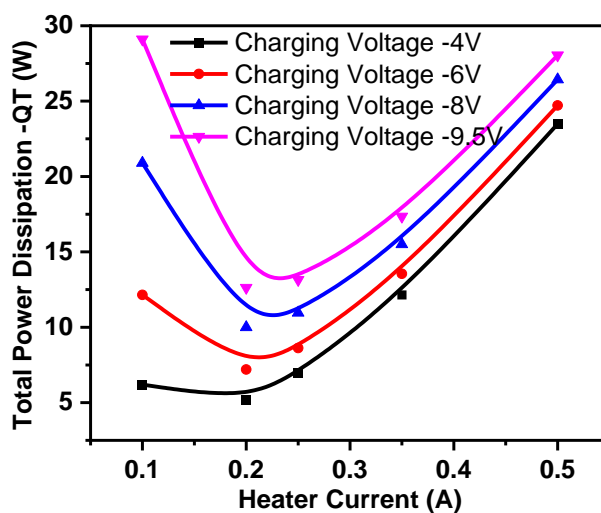


Figure 4.11 The total dissipation of heat in the PCS during the ramp-up of the magnet with the different heater currents through the FH1.

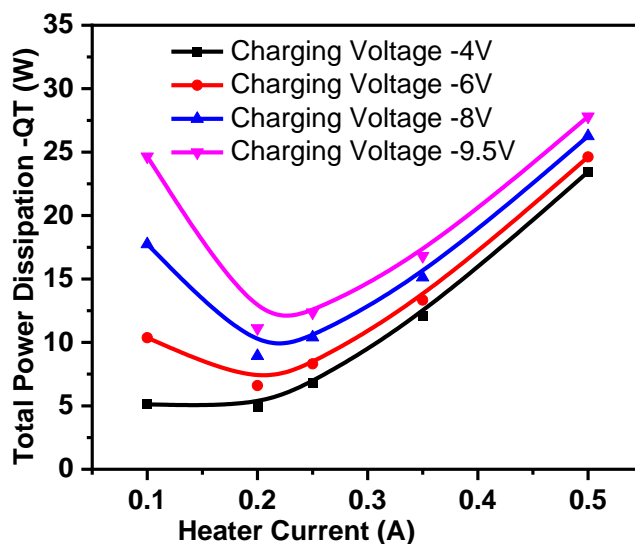


Figure 4.12 The total dissipation of heat in the PCS during the ramp-up of the magnet with the different heater currents through the FH2.

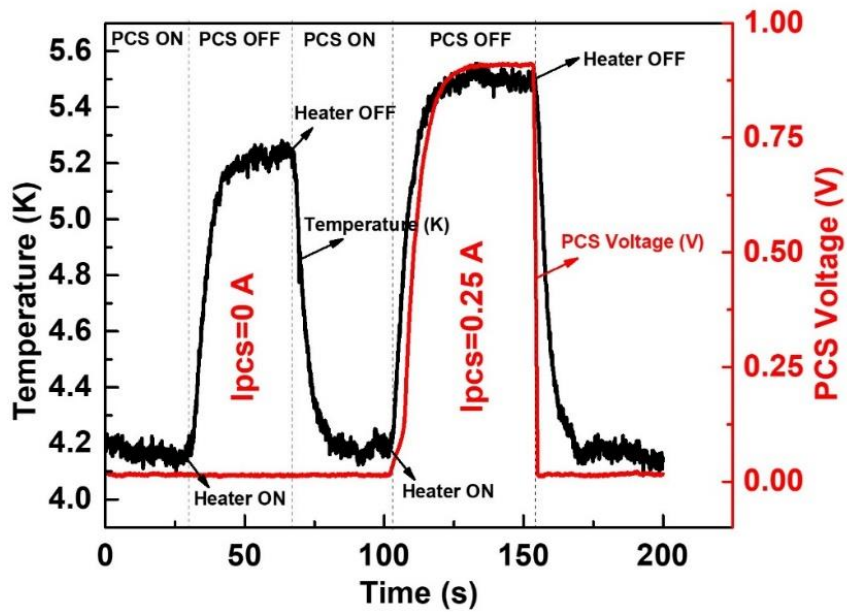


Figure 4.13 The temperature and voltage profile of the PCS with 100mA of current through the FH1 heater and 250 mA through the PCS.

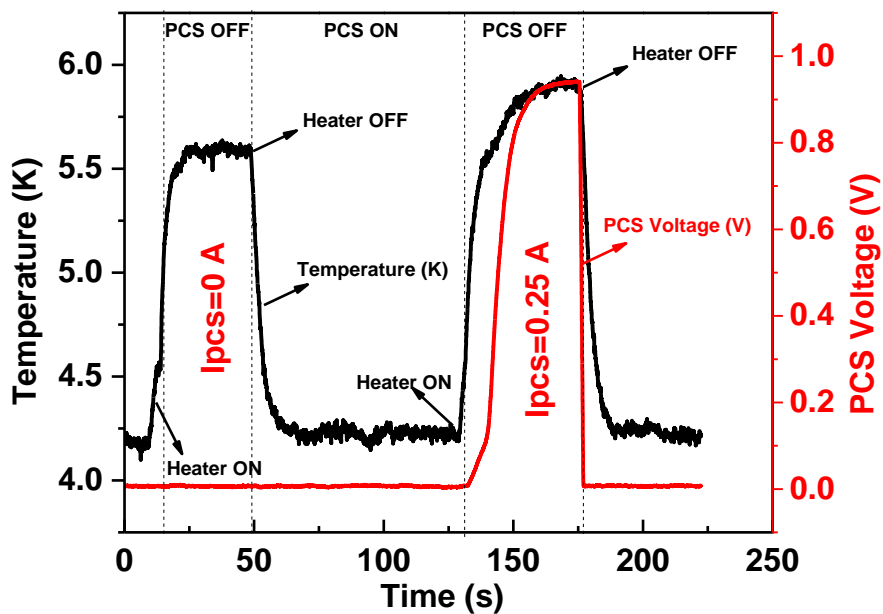


Figure 4.14 The temperature and voltage profile of the PCS with 100mA of current through the FH2 heater and 250 mA through the PCS.



The Fig.4.13 and 4.14 show the thermal and electrical behaviour of the PCS with 100 mA current through the film heaters. At the first cycle with FH1, when  $I_{PCS} = 0$ , the temperature of the PCS reaches 5.3 K still below the critical temperature of the NbTi. It needs a higher current to raise the temperature of the PCS. There are two cycles of the temperature and the voltage in each curve as shown in Fig.4.13 and Fig.4.14. The first thermal peaks shown in Fig.4.13 and Fig.4.14 are due to the current through the heater ( $I_H = 100$  mA) respectively for FH1 and FH2 with no current through the PCS circuit ( $I_{PCS} = 0$ ). The second thermal peaks as shown in Fig.4.13 and Fig.4.14 are due to the current through the heater ( $I_H = 100$  mA) respectively for FH1 and FH2 and 250 mA current through the PCS circuit ( $I_{PCS} = 250$  mA). The current through the PCS signifies the condition of the ramping of the magnet. In the second cycle, as shown in Fig.4.13, the temperature of the PCS is increased from 5.2 K to 5.5 K when the current (250 mA) is sent through the PCS. Similarly, as shown in Fig.4.14, the temperature of the PCS increases from 5.5 K to 5.9 K when the 250 mA of current is sent through the PCS. The voltage across the PCS in both cases as shown in Fig.4.13 and Fig.4.14 remains less than 1 V. This increment of temperature in the second cycle signifies the localized quenching thereby generation of small normal resistance in the PCS with 100 mA of the heater current. At 250 mA current through the PCS, an additional amount of heat is generated in the PCS due to the small resistance which thereby increases the temperature of the PCS.

Fig.4.15 illustrates the temperature, voltage profile, and switching characteristics of the PCS when the heater current is set to 100 mA, with FH1 and FH2 connected in parallel (45  $\Omega$ ). When a current of 100 mA is applied to the parallel combination of FH1 and FH2 heaters, the temperature rises to 4.9 K. However, there is no voltage across the PCS because it remains at the superconducting state due to the low resistance value of the film heater due to the parallel connection.

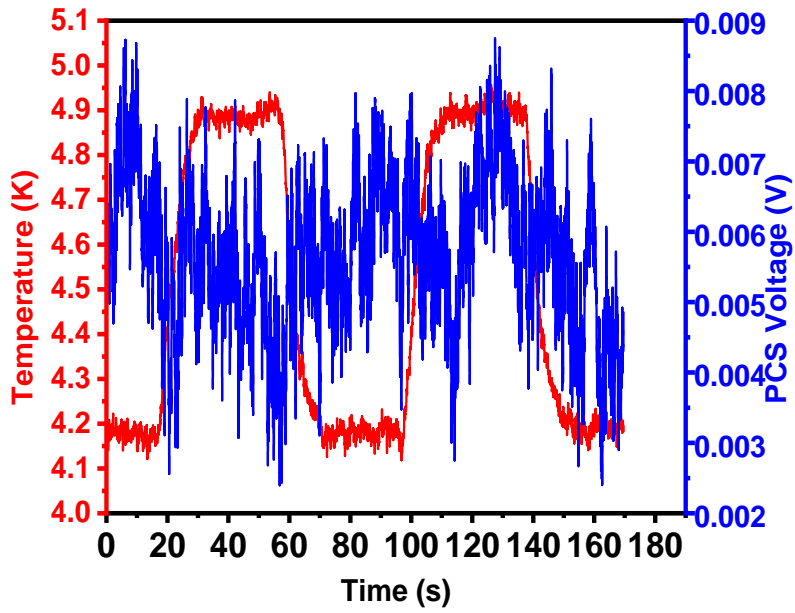


Figure 4.15 The temperature and voltage profile of the PCS with 100mA of current through the FH1||FH2 heater and 250 mA through the PCS.

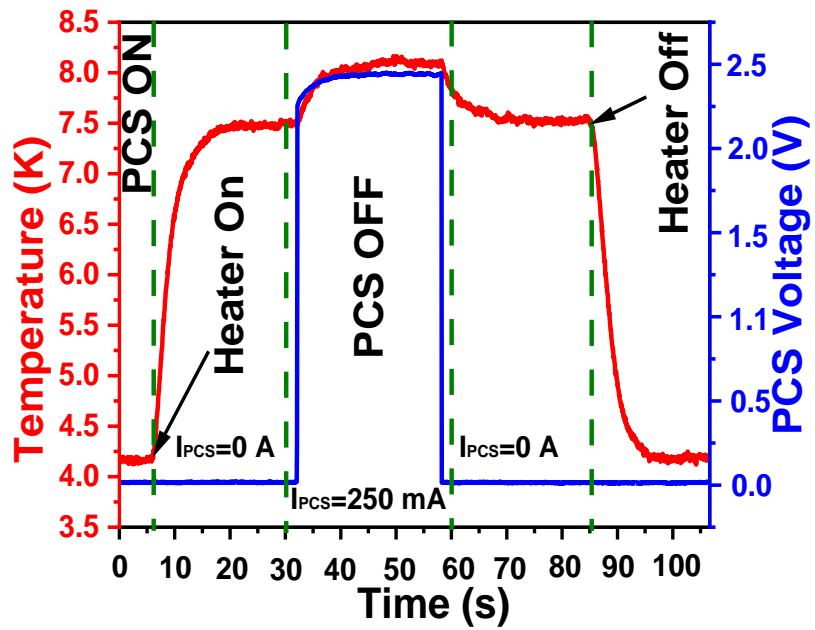


Figure 4.16 The temperature and voltage profile of the PCS with 200mA of current through the FH1 heater and 250 mA through the PCS.

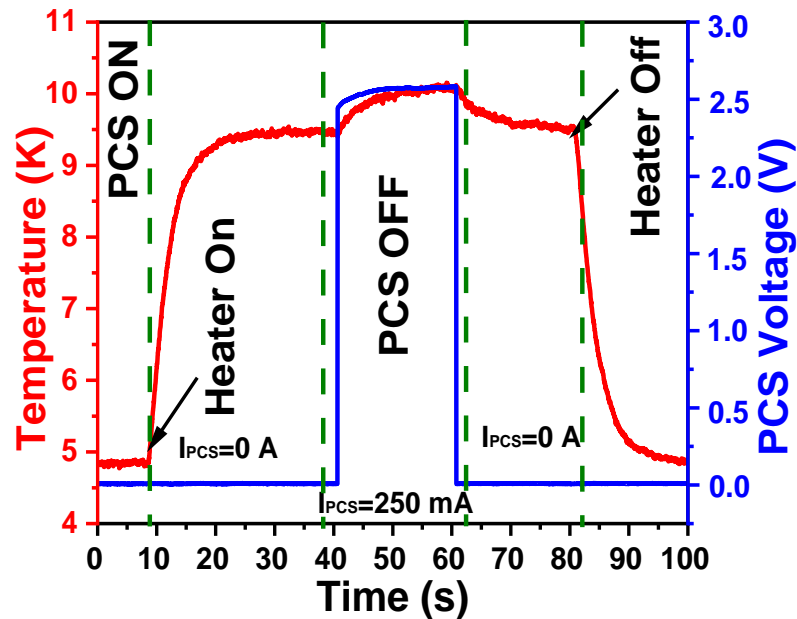


Figure 4.17 The temperature and voltage profile of the PCS with 200mA of current through the FH2 heater and 250 mA through the PCS.

Similarly, Fig.4.16 and Fig.4.17 show the temperature, the voltage profile, and the switching characteristics of the PCS at 200 mA of the heater current respectively for the FH1 and FH2 heaters. The first thermal peaks shown in Fig.4.16 and Fig.4.17 are due to the current through the heater ( $I_H = 200$  mA) respectively for FH1 and FH2 with no current through the PCS circuit ( $I_{PCS} = 0$ ). The second thermal peaks shown in Fig.4.16 and Fig.4.17 are due to the current through the heater ( $I_H = 200$  mA) respectively for FH1 and FH2 and 250 mA current through the PCS circuit ( $I_{PCS} = 250$  mA). As shown in Fig.4.16, the maximum temperature of the PCS is measured to be  $\sim 8.2$  K corresponding to the voltage of 2.5 V across the PCS at  $I_{PCS} = 250$  mA indicating a normal resistance of  $10 \Omega$ . The normal resistance of the PCS at 200mA of current FH1 signifies the partial quenching of the PCS. The temperature of the PCS is increased by 0.7 K from 7.5 K to 8.2 K when the 250 mA of current is sent to the PCS at normal state as shown in Fig.4.16.

Similarly, Fig.4.17 shows the temperature and voltage profile of the PCS at 200 mA current through the FH2 heater and 250 mA through the PCS. The temperature of the PCS is increased by 1 K from 9.5 K to 10.5 K once the 250mA of current is fed to the PCS at a normal state as shown in Fig.4.17. The corresponding voltage of the PCS is 2.75 V thereby, indicating a normal state resistance of  $11 \Omega$  which is sufficient to break the PCS circuit during the ramping up of the magnet. The switching time from the superconducting state i.e. the *ON state* to the normal conducting state i.e. the *OFF state* is measured (from Fig.4.16 and Fig.4.17) to be  $\sim 10$ s. Whereas, the switching time from the normal conducting state i.e. the *OFF state* to the superconducting state i.e. the *ON state* is also measured (from Fig.4.16 and Fig.4.17) to be  $\sim 10$ s as shown in Fig.4.16.

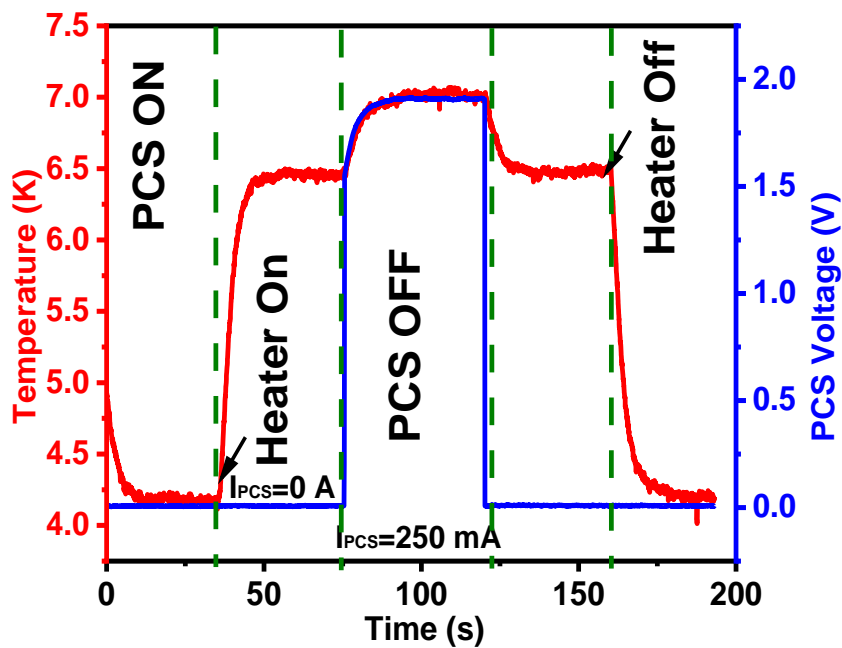
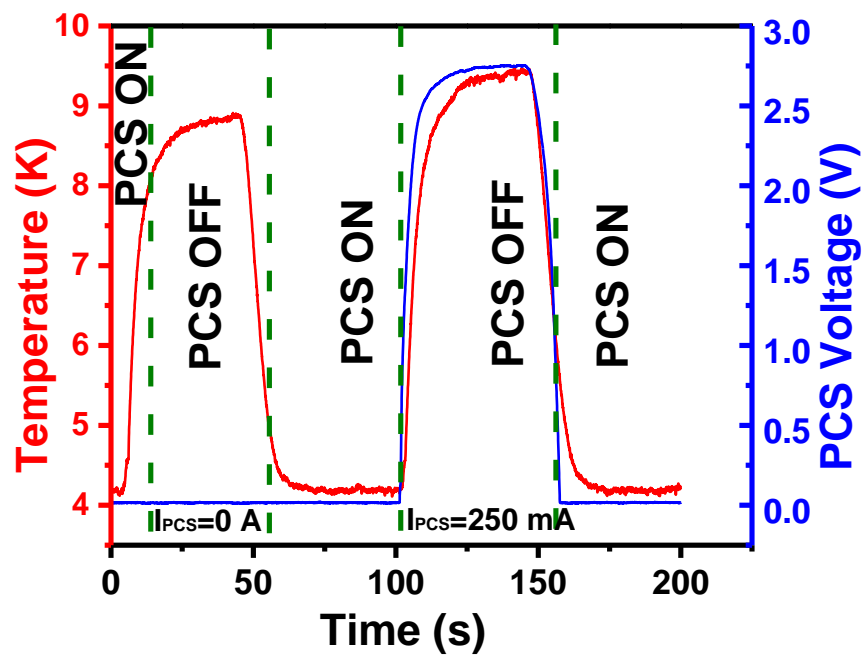


Figure 4.18 The temperature and voltage profile of the PCS with 200mA of current through the FH1||FH2 heater and 250 mA through the PCS.

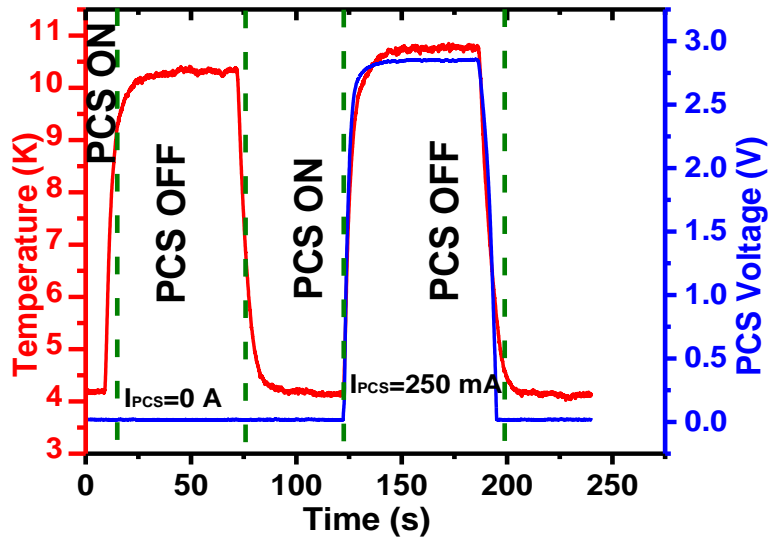
Fig.4.18 illustrates the temperature, voltage profile, and switching characteristics of the PCS when the heater current is set to 200 mA, with FH1 and FH2 connected in parallel, presenting a combined resistance of  $45 \Omega$ . When a current of

200 mA is applied to the heater, the temperature increases to 6.5 K. At this temperature, the voltage across the PCS is observed to be 1.9 V, indicating that the PCS has a resistance of approximately  $7.5 \Omega$ .

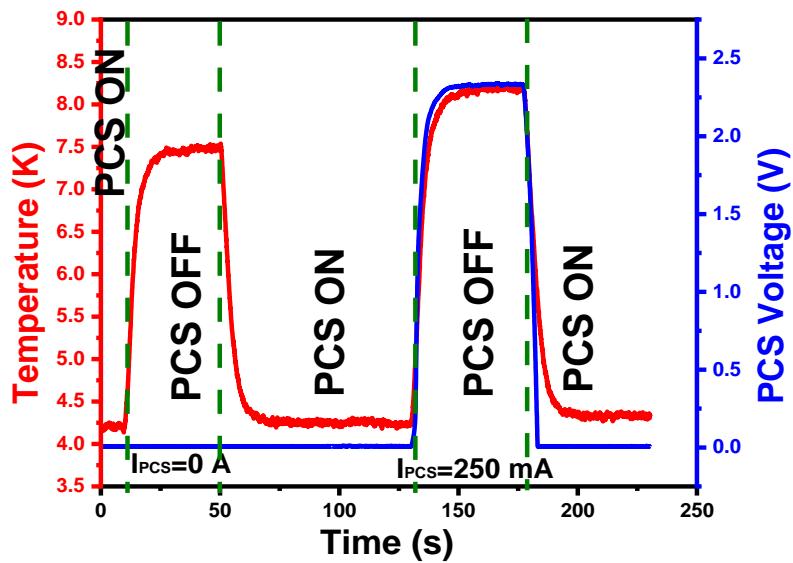
Despite the increase in temperature and the presence of a significant voltage across the PCS, the low resistance value of the film heater, combined with its parallel connection to the PCS, impacts the system's behaviour. This configuration restricts the PCS from fully transitioning to the resistive state, preventing it from achieving a complete turn-on. Instead, the PCS remains in a partially on state, characterized by its intermediate resistance and voltage values. This phenomenon highlights the influence of the parallel connection and the heater's resistance on the switching dynamics of the PCS.



(a)



(b)



(c)

Fig. 4.19 (a) The temperature and the voltage profile of the PCS (a) with 250 mA of current through the FH1 heater and 250mA of current through the PCS at the resistive state and, (b) with 250 mA of current through the heater FH2 and 250 mA of current through the PCS at its resistive state. (c) with 250 mA of current through the heaters FH1||FH2 and 250 mA of current through the PCS at its resistive state.

Fig.4.19(a) shows the temperature profile of the PCS and the corresponding voltage profile with 250 mA of current through the FH1 heater. At the 1<sup>st</sup> cycle ( $I_{PCS}=0$ ), the temperature of PCS reached 9 K as shown in Fig.4.19. The temperature reached 9.5 K when the PCS is energized with 250 mA of current at its normal state as shown in the 2<sup>nd</sup> cycle in Fig.4.19 (a). The current of 250 mA mimics the PCS current during the ramping of the magnet. The temperature of the PCS is increased by 0.6 K due to the current flow through its resistive state. The voltage drop across the PCS is measured to be 2.75 V which signified a normal resistance of 11  $\Omega$  of the PCS.

As soon as the FH1 thermo-foil heater is energized, the transition time from its ON state to OFF state happens within 15 s. Similarly, Fig.4.19(b) shows the temperature profile of the PCS and the corresponding voltage profile of the PCS with 250 mA of current through the FH2 heater and the PCS. The temperature of the PCS stabilized at 10.5 K. The corresponding voltage across the PCS is 2.9 V, corresponding to 11.6  $\Omega$  of the normal resistance of the PCS. With the FH2 heater, the equilibrium temperature of the PCS is 1 K higher than its equilibrium temperature with the heater FH1 at the same heater power.

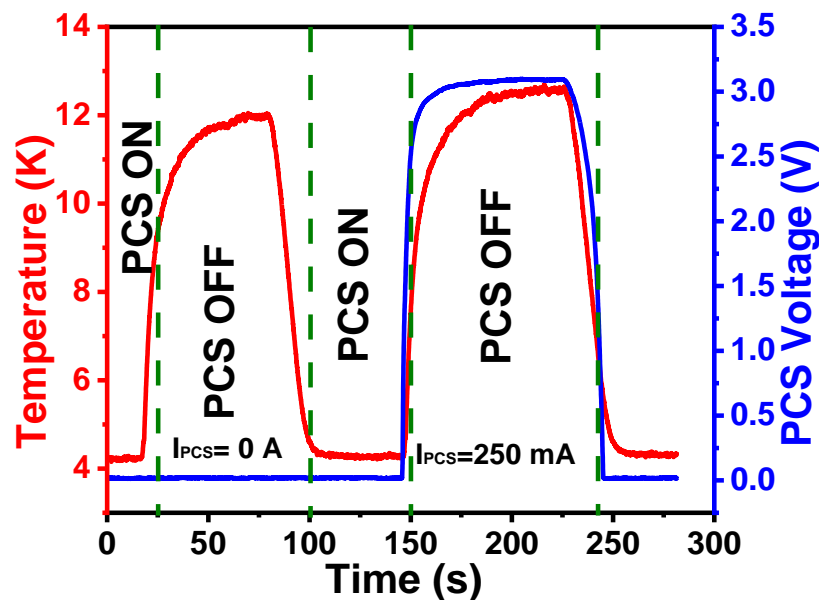


Figure 4.20 The temperature and voltage profile of the PCS with 350mA of current through the FH1 heater and 250 mA through the PCS.

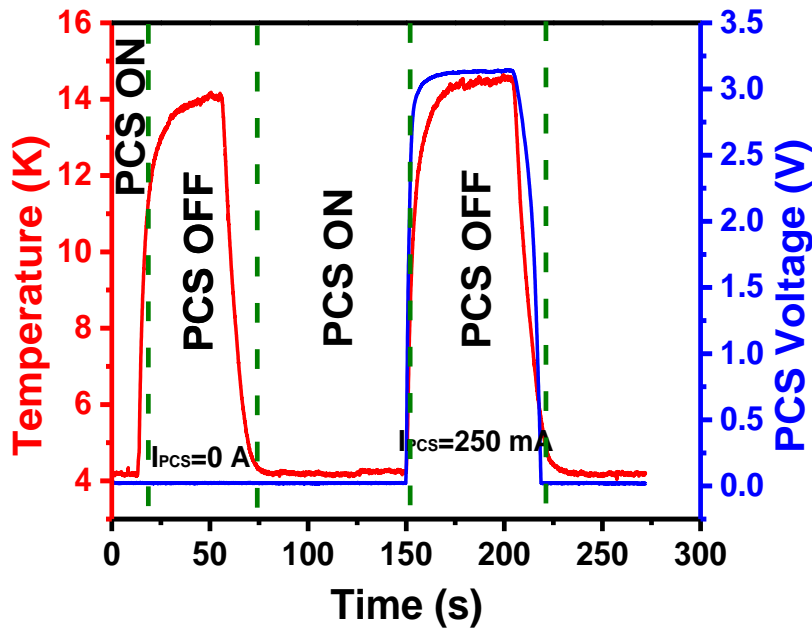


Figure 4.21 The temperature and voltage profile of the PCS with 350mA of current through the FH2 heater and 250 mA through the PCS.

Fig.4.21 shows the temperature profile of the PCS and the corresponding voltage profile with 350 mA of current through the FH2 heater. The equilibrium temperature of the PCS reached 15 K shown in Fig.4.20. The corresponding voltage across the PCS is 3.25 V which corresponds to a normal resistance of 13  $\Omega$ . The normal resistance per meter measured is 0.325  $\Omega$  /m which is 12 % less than that of the actual value of the normal resistance at 15 K. This signifies a non-uniform temperature distribution inside the winding of the PCS at its resistive state. Hence, the PCS needs much better thermal isolation to have uniform temperature distribution. However, the higher degree of thermal isolation would increase the transition time from the normal conducting state to the superconducting state.

Fig.4.22 illustrates the temperature, voltage profile, and switching characteristics of the PCS when the heater current is set to 350 mA, with FH1 and FH2 connected in parallel, presenting a combined resistance of 45  $\Omega$ . When a current of 350 mA is applied to the heater, the temperature increases to 9.5 K. At this temperature,



the voltage across the PCS is observed to be 2.75 V, indicating that the PCS has a resistance of approximately 11  $\Omega$ .

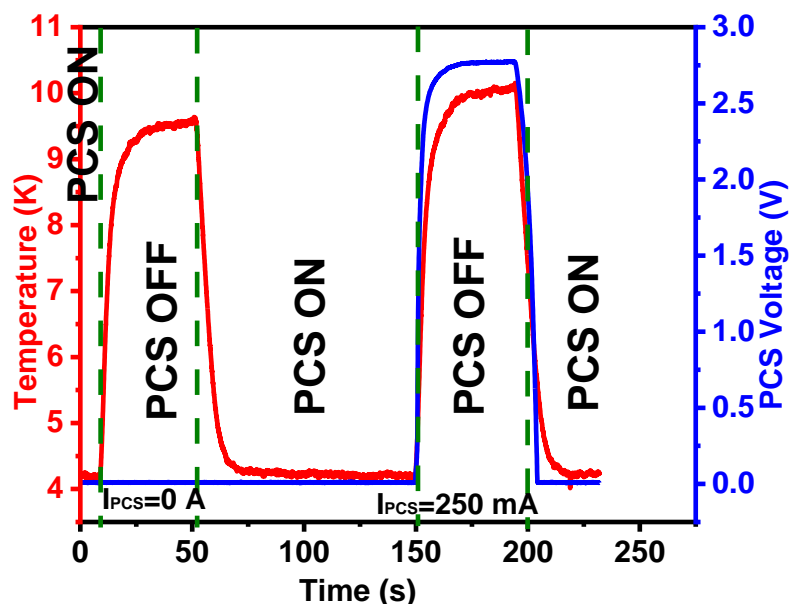


Figure 4.22 The temperature and voltage profile of the PCS with 350mA of current through the FH1||FH2 heater and 250 mA through the PCS.

Fig.4.23 shows the temperature profile of the PCS and the corresponding voltage profile with 500 mA of current through the FH1 heater. At the 1<sup>st</sup> cycle ( $I_{PCS}=0$ ), the temperature of PCS reached 17 K as shown in Fig.4.19. The temperature reached 18 K when the PCS is energized with 250 mA of current at its normal state as shown in the 2<sup>nd</sup> cycle in Fig.4.23 The current of 250 mA mimics the PCS current during the ramping of the magnet. The temperature of the PCS is increased by 1 K due to the current flow through its resistive state. The voltage drop across the PCS is measured to be 3.25 V which signified a normal resistance of 13  $\Omega$  of the PCS.

Fig.4.24 shows the temperature profile of the PCS and the corresponding voltage profile of the PCS with 500 mA of current through the FH2 heater and the PCS. The temperature of the PCS stabilized at 20 K. The corresponding voltage across the PCS is 3.35 V, corresponding to 13.4  $\Omega$  of the normal resistance of the PCS.

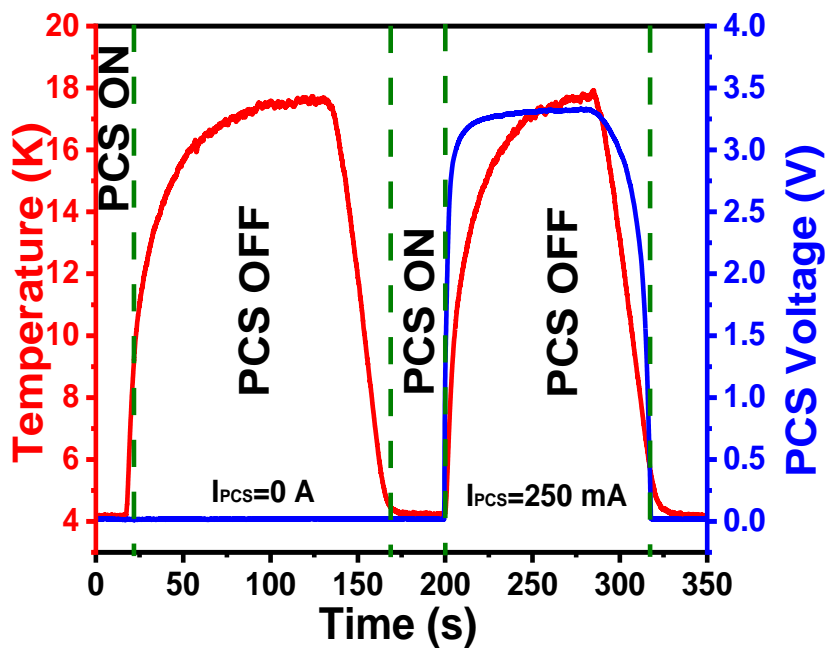


Figure 4.23 The temperature and voltage profile of the PCS with 500mA of current through the FH1 heater and 250 mA through the PCS.

Fig.4.25 illustrates the temperature, voltage profile, and switching characteristics of the PCS when the heater current is set to 500 mA, with FH1 and FH2 connected in parallel, presenting a combined resistance of  $45\Omega$ . When a current of 500 mA is applied to the heater, the temperature increases to 13 K. At this temperature, the voltage across the PCS is observed to be 3.1 V, indicating that the PCS has a resistance of approximately  $12.4\Omega$ .

When a current of 500 mA is applied, the total power dissipation needs to be considered, assuming a charging voltage of around 6 V. For FH1, the power dissipation is approximately 27 W, while for FH2, it is around 23 W. This combined power dissipation can boil off around 15 liters of liquid helium during the ramping process, even though the on-state resistance of the system is highly efficient. This highlights the importance of managing power dissipation in systems involving cryogenic liquids.

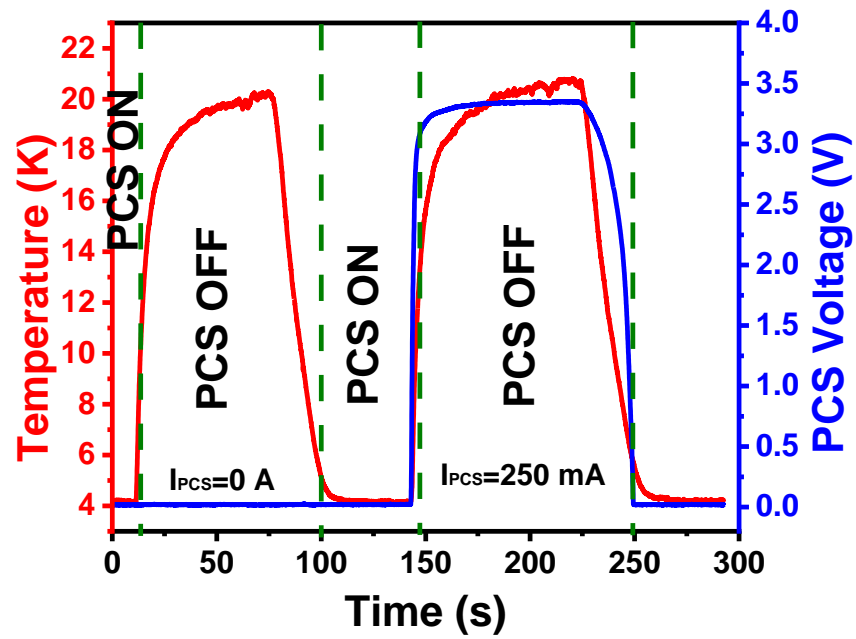


Figure 4.24 The temperature and voltage profile of the PCS with 500mA of current through the FH2 heater and 250 mA through the PCS

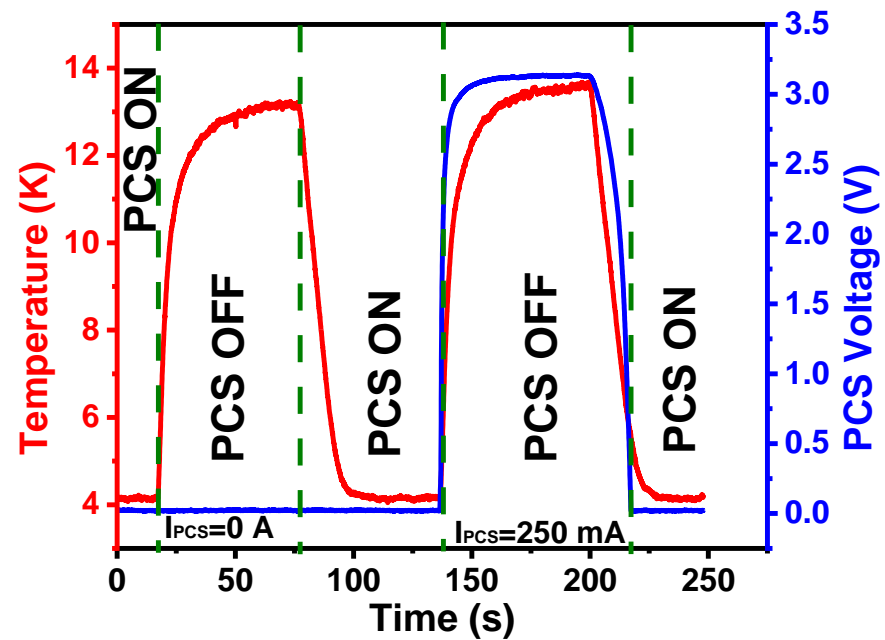


Figure 4.25 The temperature and voltage profile of the PCS with 500mA of current through the FH1||FH2 heater and 250 mA through the PCS.

Fig.4.26 shows the relation of the power loss ( $P_{\text{loss}}$ ) as defined in Eq. (4.5), with the normal resistance of the PCS during the ramp-up of the magnet at the various charging voltages. The point 'P' in Fig.4.26 indicates the power loss ( $P_{\text{loss}}$ ) of 0.23% in the PCS ( $\sim 13 \Omega$  normal resistance at 15K) while charging the magnet at 6 V. The percentage of energy losses into the PCS at  $17 \Omega$ ,  $20 \Omega$ ,  $25 \Omega$  of normal resistance will be 0.18%, 0.16%, and 0.12% as shown in Fig.4.26. Hence to reduce the energy loss on the PCS while charging the magnet at 6 V, the normal resistance needs to be increased. The normal resistance can be increased by improving the thermal isolation of the PCS which can be implemented in the final PCS.

The normal resistance of the same PCS can also be increased by using only four if operating current of the magnet is less. The estimated normal resistance of the same PCS would be  $\sim 22 \Omega$  with four strands of the conductor. Considering the 12 % reduction in actual normal resistance of the PCS, the effective normal resistance will be  $\sim 19.4 \Omega$  would eventually result in 0.16 % of energy loss during charging the magnet with 6 V of charging voltage.

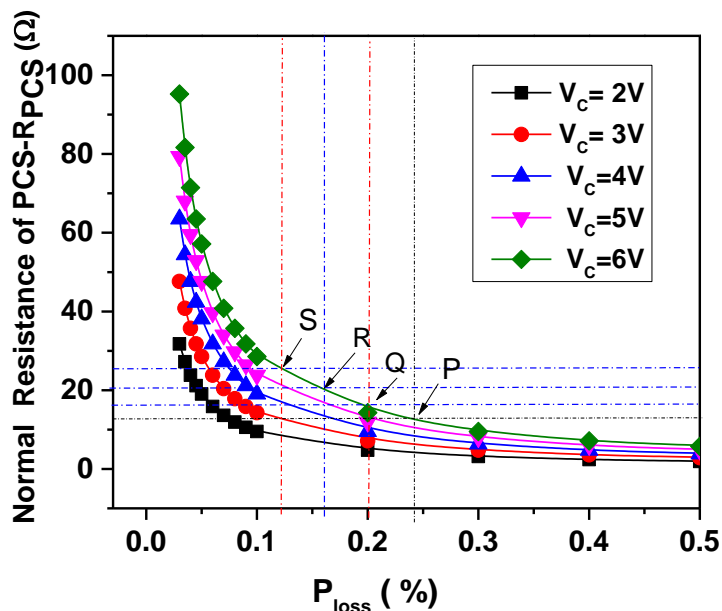


Figure 4.26 The estimated energy dissipation on PCS at various normal resistance during ramping of the MRI magnet.

## 4.7 Summary

A prototype PCS for a whole-body MRI magnet has been designed, fabricated, and tested in liquid helium. A comparative analysis of the temperature profile and switching behavior is analyzed for the various thermo-foil heaters located at the various layers of the PCS. Heater FH2 gives optimum performance by generating a better temperature profile dissipating a moderate amount of heat during the ramping process. Based on the measured normal resistance and the heat dissipation, the input parameters were generated for the final PCS.

The complete scheme of the main magnet coils and the EIS coils is shown in chapter 3. The two PCSs are linked in series with the coils, one for the main coil (PCS) and the other for the EIS coil (PCS). These PCSs enable the main magnet and EIS coils to run in the persistent mode. Two sets of back-to-back power diodes are connected in parallel with the MAIN PCS and the EIS PCS. These diodes protect the PCS coils against the excessive current built up during the magnet quench by providing an alternate parallel current path. The PCS is one of the most crucial components of an MRI magnet. If the PCS is damaged, the magnet operation is disruptive. The PCS has to be protected from any eventualities that arise during operation. In addition, the maximum allowable currents of the PCS at the normal state are lower than those at the superconducting state. Thus, it is necessary to protect the superconducting wire of the PCS. The details of the PCS protection are explained in the chapter 6.

## CHAPTER 5

### EXTERNAL INTERFERENCE SCREENING COIL

#### 5.1 Introduction

The whole-body clinical MRI scanners need a highly homogeneous magnetic field inside the field-of-view (FOV) at its imaging volume. The gyromagnetic frequency i.e., the characteristic frequency of the hydrogen ions or the protons, is proportional to the magnetic field. At the 1.5 T magnetic field, the gyromagnetic frequency of the hydrogen ions is 63.87 MHz. Any change in the magnetic field will lead to a change in the resonance frequency of the ions. The resonance frequency variation must be less than 6 Hz/hr for a 1.5 T magnet. Any external magnetic disturbances may change the central magnetic field ( $B_0$ ) at the iso-center and its homogeneity at the imaging volume. An actively shielded magnet is relatively sensitive to external disturbances as it is unable to compensate automatically for the external magnetic disturbances in its imaging volume. The high-frequency fluctuations in the ambience are shielded by the induced eddy current in the conductive layers of the thermal shield around the solenoid

magnet of the MRI. The low-frequency fluctuations in the ambient magnetic field may cause a significant change in the  $B_0$  field and its resonance frequency. The fluctuation in the ambient field varies between 10 nT to 100 nT depending on the solar activity or moving metal objects in the vicinity of the MRI magnet [76 – 77]. The imaging volume of the MRI magnet needs to be protected from any such external magnetic interferences. Various techniques are available for shielding such external disturbances in the presence of a low magnetic field, but it is difficult to shield the fluctuation using an iron or  $\mu$ -metal shield at the high field region. High-permeable materials like iron or  $\mu$ -metal will be saturated in the high-field region. Thus, the shielding is ineffective. The inductive method is the most widely used technique for eliminating external interference in MRI magnet [78 – 83]. The electric active compensation system is also used by some researchers [85]. In the inductive technique, a set of shorted superconducting coils known as the  $B_0$  compensation coil or the external interference screening (EIS) coil is symmetrically positioned radially from the axis and with respect to the midplane to achieve a shielding effect against any external magnetic interference. It is self-activated and works passively in the system. The configuration of the EIS coil will be determined by various competing designing parameters: mutual inductance ( $M_{sm}$ ) with the magnet, the coupling factor ( $K$ ), and the screening factor ( $S$ ). The screen factor must be 0.95 or 95 %. The original peak-to-peak homogeneity of the MRI magnet needs to be preserved or even improved by the inclusion of the EIS coil in the magnet system. In the case of deterioration, the peak-to-peak homogeneity must be limited to 10 ppm. It is better to have lower mutual inductance and coupling factor. Limited studies have been reported on how the characteristics of the EIS coil is affected by the various parameters and how these parameters need to be prioritized in generating the design inputs for the EIS coil. During a quench of the MRI magnet, a large amount of eddy current will be induced into the EIS coil due to the fast-decaying field in the background. There are limited studies available on the effect on the EIS coil during the quenching of the MRI magnet.

This chapter focuses on the design aspects of the EIS coil for a whole-body clinical MRI magnet by analyzing the homogeneity, mutual inductance, coupling

factor, and screening factor of four sets of EIS coils with varying turn ratios and radial gaps between the EIS coil and the corresponding magnet coil. Additionally, the chapter examines the current induction in the EIS coil during a quench of the main magnet and its consequential effects.

## 5.2 External magnetic interference

Magnetic field variations can occur in a wide range of frequencies. In MRI high-frequency fluctuations in the ambient magnetic field are shielded by an eddy current induced in the copper shield, while the low-frequency fluctuations in the ambient field generally cause significant changes in the central magnetic field, distorting the image quality.

These fluctuations may occur due to elevators, subways, cars moving in the vicinity, or other metallic movements near the MRI. Even when these manmade sources are absent, the earth's magnetic field can vary. Depending on different conditions these fields can vary from 10 nT to 10  $\mu$ T. Fig.5.2 shows the variation of magnetic field during different hours of day and night measured by a fluxgate magnetometer recorded at the Accelerator Laboratory, CERN [77].

As stated above, higher-frequency magnetic disturbances can be shielded using copper or aluminum screening but the low-frequency magnetic disturbances can't be shielded using these metals because these are non-magnetic materials and to achieve screening, the thickness of the material has to be high, which is not feasible. Another way to shield such low-frequency disturbance is to use high permeability material, but due to a larger range of frequency these materials will saturate easily.



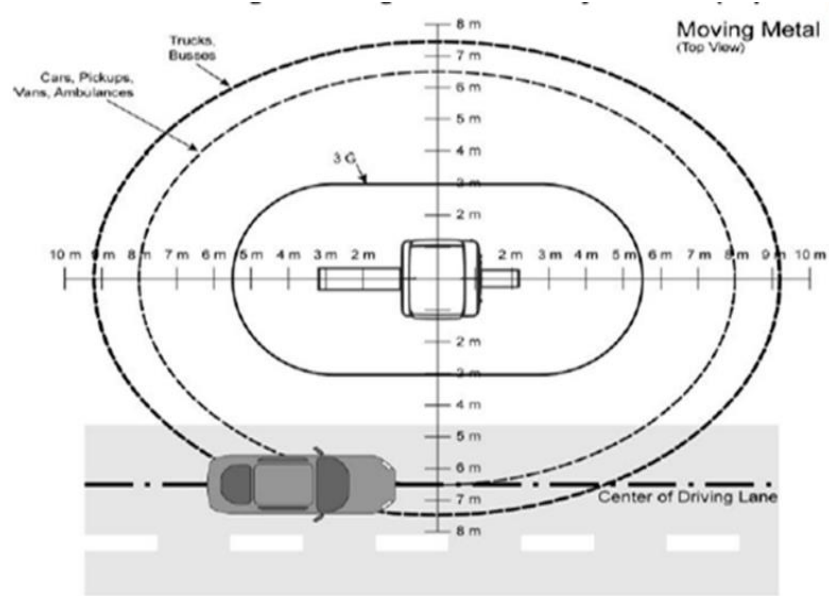


Figure 5.1 Fluctuation in the magnetic field in the environment outside the MRI.[77-78]

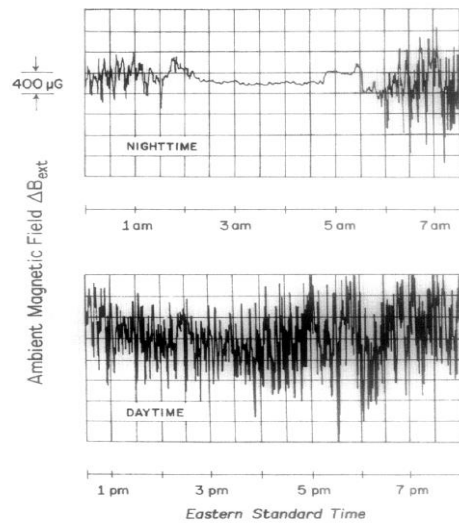


Figure 5.2 Fluctuation in magnetic field in the environment of Accelerator laboratory CERN, Geneva as measured using a fluxgate magnetometer and a detection bandwidth of 0.01 Hz.[77]

### 5.3 Working principle of EIS coil

EIS coil is made of superconducting wire. It contains a small no of turns as compared to the main magnet. It is located over each magnet coil and all the coils are connected in series. The location and number of turns can be calculated by an optimization method. The superconducting wire used for the EIS coil has a low critical current,  $I_c$  (~10Amp), because a current more than the prescribed value can disturb the homogeneity of main field. Due to a disturbance, if there is a variation in an ambient magnetic field, the EIS coil will have an induced current opposing the field disturbance. The field disturbance will thus not reach the imaging volume. Because these coils are made of superconductors, induced current can flow forever in a loop. So, it is necessary to quench the EIS circuit at some specified periodic intervals. For that, the circuit contains a PCS which can be turned on to quench the EIS circuit. During the charging and discharging of the magnet the EIS-PCS will be in ON state to protect the circuit from excessive induced currents which can damage the circuit. The arrangement of the EIS coil, primary coil, and shield coil is shown in the form of a block diagram in Fig.5.3.

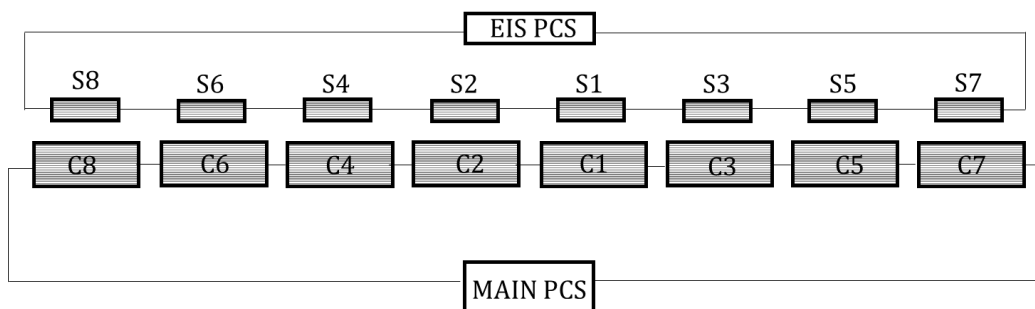


Figure 5.3 Schematic of EIS coils with main coils.

### 5.4 Design of EIS coil

The EIS coil of the MRI magnet is designed using the flux conservation principle in a coupled solenoid. By Lenz's law, any magnetic field produced by an induced current will be in the opposite direction to the change in the original field. When an external

magnetic field is applied in a shorted superconducting solenoid, a current is induced in the superconducting circuit to maintain the total magnetic flux constant. Hence, the EIS coil would inductively be coupled with external interference. The flux conservation is governed by the Eq.(5.1) [77],

$$\int_s^0 (B_s + B_e) dA = 0 \quad (5.1)$$

Where  $B_e$  is an external magnetic interference field that induces current  $I_s$  in the shorted solenoid or the EIS coil i.e the  $s$  coil, which in turn produces a magnetic field,  $B_s$ , and  $\int_s dA$  Signifies the integration over the area of the solenoids.

The induced current in the EIS coil persists as there is effectively no resistance in this superconducting circuit. If  $B_0$  is the central field of the MRI magnet, the screening factor ( $S$ ), defined by the variation of central magnetic field per unit variation of an external magnetic field, which is given by Eq.(5.2);

$$S = 1 - \frac{dB_0}{dB_e} \quad (5.2)$$

The screening factor ( $S$ ) becomes zero for a perfect screening that happens in case of zero couplings between  $\frac{dB_e}{dt}$  and  $\frac{dB_0}{dt}$ . In general,  $S$  is expressed by a fraction. But it can also be expressed in %.

For an external field,  $B_e$ , the circuit equations for the main coil of the magnet and the corresponding EIS coil can be written as Eq.(5.3) and Eq.(5.4)

$$L_m \frac{dI_m}{dt} + M_{sm} \frac{dI_s}{dt} + \frac{d}{dt} (\int B_e dA) = 0 \quad (5.3)$$

$$L_s \frac{dI_m}{dt} + M_{sm} \frac{dI_m}{dt} + \frac{d}{dt} (\int B_e dA) = 0 \quad (5.4)$$

Where  $L_s, L_m, M_{sm}$  are respectively the self-inductances of the EIS coil, the magnet coil, and the mutual inductance between them.  $I_m, I_s$  are respectively the current in the magnet coil and the induced current in the EIS coil.

The mutual inductance can be estimated by energy method using the TOSCA code of OPERA-3D program, where the magnet coil and the EIS coil are energized separately and then together to find out the stored energy in the magnet coil, the EIS coil and the total energy stored by the combination of magnet coil and the EIS coil. Eqs. (5) - (7) are the governing equations for the estimation of the stored energy. The mutual inductance can be calculated by using the energy method governed by Eq. (5.8).

$$E_s = \frac{L_s I_s^2}{2} \quad (5.5)$$

$$E_m = \frac{L_m I_m^2}{2} \quad (5.6)$$

$$E_T = \frac{L_s I_s^2}{2} + \frac{L_m I_m^2}{2} + M_{sm} I_s I_m \quad (5.7)$$

$$M_{sm} = \frac{E_T - (E_m + E_s)}{I_s I_m} \quad (5.8)$$

Where  $E_s, E_m$  are respectively the stored energies of the EIS and magnet coils, and  $E_T$  is the total stored energy of the coupled system.

One of the critical parameters for determining the dimension and the relative position of the EIS coil is the mutual coupling between the EIS coil and the magnet coil. Hence, their coupling factor ( $K$ ), defined by Eq. (5.9), plays an important role in designing the effective EIS coil [82-84].

$$K^2 = \frac{M_{sm}^2}{L_m L_s} \quad (5.9)$$

It signifies the fraction of magnetic field links due to currents induced in one coil due to field change in another coil. Though the EIS coil needs to be strongly coupled with the external interferences, it should have a very weak coupling with the magnet. However, the EIS coil shares the same space as the magnet. It would inevitably be coupled to the magnet coil to some extent.

The temporal change in the central field;  $\left(\frac{dB_0}{dt}\right)$  can be expressed by Eq. (5.10);

$$\frac{dB_0}{dt} = \frac{dB_m}{dt} + \frac{dB_e}{dt} + \frac{dB_s}{dt} \quad (5.10)$$

Eq. (5.10) can be expressed in terms of the geometrical factors of the main magnet ( $g_m$ ) and the EIS coil ( $g_s$ ) coil respectively;

$$\frac{dB_0}{dt} = g_m \frac{dI_m}{dt} + g_s \frac{dI_s}{dt} + \frac{dB_e}{dt} \quad (5.11)$$

The geometrical factor ( $g_i$ ) of each coil is defined by Eq.(5.12)

$$g_{i=m,s} = \frac{\mu_0 N_i}{2} \frac{r_i^2}{(r_i^2 + z_i^2)^{3/2}} \quad (5.12)$$

Where  $g_i$  is the geometrical factor in  $T/A$ ,  $\mu_0$  is  $4\pi \times 10^{-7}$  H/m,  $N_i$  is the total number of turns in the coil,  $r_i$  is the radius of each coil and  $Z_i$  is the axial distance from the center.

Using Eqs. (5.3) - (5.11), Eq. (5.10) can be expressed by Eq. (5.13),

$$\frac{dB_0}{dt} = \frac{dB_e}{dt} \left[ \left( \frac{Kg_m}{\sqrt{L_m}} - \frac{g_s}{\sqrt{L_s}} \right) \left( \frac{\pi \sum_{i=1}^{N_s} r_i^2}{\sqrt{L_s}(1-K^2)} \right) \right] \quad (5.13)$$

Hence, the screening factor;  $\left( \frac{dB_0}{dB_e} \right)$ , can be expressed by;

$$S = \left( \frac{Kg_m}{\sqrt{L_m}} - \frac{g_s}{\sqrt{L_s}} \right) \left( \frac{\pi \sum_{i=1}^{N_s} r_i^2}{\sqrt{L_s}(1-K^2)} \right) \quad (5.14)$$

Where  $N_s$  is the number of turns in each EIS coil and  $r_i$  is the radius of  $i^{\text{th}}$  turn of each EIS coil.

## 5.5 Design parameters

The following parameters are important for the design of the EIS coil:

### 5.5.1 Number of turns calculation

The calculations to determine the position of the EIS coils and the number of turns in these coils are very important to optimize various parameters. An optimized value is shown below which can be used in the designing of the EIS coil. Only the turns ratio can be used but position needs to be optimized according to the dimension of the main magnet. The turn ratio can vary according to main magnet design. The no of turns of EIS coil is different for each set of primary coil and shield coil. The ratio shows no. of turns in the EIS coil per 100 turns of the corresponding coil.

$$\frac{N_{s1}}{N_{m1}} = \frac{0.6}{100} \quad (5.13)$$

$$\frac{N_{s3}}{N_{m3}} = \frac{1.8}{100} \quad (5.14)$$

$$\frac{N_{s5}}{N_{m5}} = \frac{1.09}{100} \quad (5.15)$$

$$\frac{N_{s7}}{N_{m7}} = \frac{2.3}{100} \quad (5.16)$$

In this context,  $N_{m1}$  represents the number of turns in coil 1,  $N_{m3}$  denotes the number of turns in coil 3,  $N_{m5}$  signifies the number of turns in coil 5, and  $N_{m7}$  indicates the number of turns in coil 7. Correspondingly, the number of turns of the EIS coil corresponding to coil 1 is represented by  $N_{s1}$ , the number of turns of the EIS coil corresponding to coil 3 is denoted by  $N_{s3}$ , the number of turns of the EIS coil corresponding to coil 5 is indicated by  $N_{s5}$ , and the number of turns of the EIS coil corresponding to coil 7 is represented by  $N_{s7}$ . These parameters are essential for understanding the configurations and interactions within the electromagnetic induction system.

### 5.5.2 Geometrical factor

The geometric factor is a dimension-based value that gives the value of magnetic field due to one ampere of current. We can calculate the value of the geometric factor of the main magnet and EIS coil using the equation given below.

$$g = \frac{\mu_0 N}{2} \frac{r^2}{(r^2 + z^2)^{3/2}} \quad (5.17)$$

The geometric factor, denoted as  $g$ , is measured in Tesla per Ampere (T/A). The permeability of free space, represented by  $\mu_0$ , has a constant value of  $4\pi \times 10^{-7}$  henry per meter (H/m). The total number of turns in the coil is indicated by  $N$ , while  $r$  refers to the radius of the loop. Additionally,  $z$  represents the distance from the center. These parameters are crucial in determining the magnetic field characteristics in various electromagnetic applications.

### 5.5.3 Self-inductance

The self-inductance of a loop of wire with the radius  $R$  and circular cross-section of radius  $r_a$  can be calculated using the following equation.

$$L_{\text{self}} = \mu_0 N^2 R \ln \left( \frac{8R}{r_a} - \frac{7}{4} \right) \quad (5.18)$$

For rectangular wire

$$r_a = \sqrt{\frac{wh}{\pi}} \quad (5.19)$$

For the calculation of self-inductance, the following parameters are considered:  $R$ , which denotes the loop radius of the coil;  $r_a$ , representing the cross-section of the wire;  $N$ , indicating the number of turns;  $W$ , which stands for the width of the coil; and  $h$ , referring to the height of the coil. These factors collectively influence the self-inductance value, which is a crucial characteristic in determining the coil's ability to store magnetic energy.

#### 5.5.4 Coupling factor between main and screening coil

The coupling factor has an important role in the making of EIS coils; it gives the fraction of magnetic field links due to current induced in one coil due to field change in another coil. The value of the coupling factor lies between -1 & 1. The value of  $K$  is selected such that the EIS coil should have minimum coupling with the main coil, since during the quench of the main coil minimum current should be induced in EIS coil otherwise it can be damaged. The coupling factor can be calculated using the following formula.

$$K = \frac{M_{sm}}{\sqrt{L_m L_s}} \quad (5.20)$$

In the context of electromagnetic systems, the coupling factor, denoted as  $K$ , is a crucial parameter that measures the degree of coupling between two coils. This factor is influenced by several other parameters:  $M_{sm}$ , which represents the mutual inductance between the main magnet and the EIS coil;  $L_m$ , indicating the total



inductance of the main magnet; and  $L_s$ , referring to the total inductance of the EIS coil. The coupling factor  $K$  is essential for understanding the efficiency and effectiveness of the energy transfer between the main magnet and the EIS coil, with higher values indicating stronger coupling.

### 5.5.5 Mutual-inductance calculation

The mutual inductance can be obtained by the energy method in OPERA-TOSCA, where the Main coil and EIS coil are energized separately and then together, to find stored energy in the main coil, EIS coil, and total energy stored by the combination of both coils. Mutual inductance can be calculated using the energy method which is given below.

$$E_s = \frac{L_s I_s^2}{2} \quad (5.21)$$

$$E_m = \frac{L_m I_m^2}{2} \quad (5.22)$$

$$E_T = \frac{L_s I_s^2}{2} + \frac{L_m I_m^2}{2} + M_{sm} I_s I_m \quad (5.23)$$

$$M_{sm} = \frac{E_T - (E_m + E_s)}{I_s I_m} \quad (5.24)$$

Where,  $E_s$  is the stored magnetic energy of the EIS coil,  $E_m$  is the stored magnetic energy of the main magnet,  $E_T$  is the total stored energy,  $M_{sm}$  is the mutual inductance between the two coils,  $L_s$  is the self-inductance of the EIS coil,  $L_m$  is the self-inductance of the main magnet,  $I_s$  is the current in the EIS coil,  $I_m$  is the current in the main magnet

### 5.5.6 Screening factor

The screening factor gives the value of change in the main field ( $B_0$ ) due to disturbing field ( $B_d$ ). This can be calculated using the following formula. For ideal screening the value of screening should be zero means there is no field change of the main magnet due to any disturbance.

$$S = 1 - \frac{dB_0}{dB_d} \quad (5.25)$$

$$S = 1 + \left( \frac{kg_m}{\sqrt{L_m}} - \frac{g_s}{\sqrt{L_s}} \right) \left( \frac{\pi \sum_{i=1}^{N_s} r_i^2}{\sqrt{L_s}(1-k^2)} \right) \quad (5.26)$$

In the context of electromagnetic systems, several key parameters play a crucial role in determining the system's performance. The screening factor, denoted as  $S$ , is important for assessing the effectiveness of shielding in the system. The coupling factor, represented by  $K$ , measures the degree of coupling between the coils. The total inductance of the main magnet is indicated by  $L_m$ , while  $L_s$  denotes the total inductance of the EIS coil. Additionally, the geometric factor of the main magnet, denoted as  $g_m$ , and the geometric factor of the EIS coil, represented by  $g_s$ , are critical for understanding the spatial configuration and field distribution. The radius of the EIS coil is indicated by  $r$ . These parameters collectively influence the efficiency and functionality of the electromagnetic system.

### 5.5.7 Homogeneity of EIS coil

The field generated by the EIS coil is in the range of microtesla but this field in turn can affect the homogeneity of the MRI magnet thus the selection of the EIS coil should be such that the central homogeneity (usually in a 45 cm DSV) is unaffected. In this case, the limit of allowable perturbations inhomogeneity of the EIS coil is set to be 1% or less in the 45cm DSV so that the MRI magnet homogeneity stays unaffected.

## 5.6 Configuration of 1.5 T magnet

We have designed a multi-coil superconducting solenoid magnet for an MRI scanner that has four pairs of symmetrical coils: 1-2, 3-4, 5-6, and 7-8 placed in an axial symmetrical position to generate a 1.5 T central field with 5 ppm peak-to-peak homogeneity in the FOV of 45 cm at its iso-center as shown in Fig.5.5. There are three pairs (C1- C6) of the primary coil and one pair (C7 -C8) of the active shield coil. The current in the shield coils (C7 to C8) flows in opposite to the current in the primary coils (C1-C6). The parameters of the 1.5 T MRI magnet are summarized in Table 5.2.

Table 5.1 The parameters of the whole-body 1.5 T MRI magnet.

<b>Description</b>	<b>Value</b>
Central field	1.5 T
Operating current	450 A
Field of View	45 cm
Homogeneity (peak-to-peak)	10 ppm
Number of Superconducting coils	8
Number of primary coils	6
Number of active shield coils	2

## 5.7 Configuration of EIS coil

A set of superconducting EIS coils needs to be designed for the whole-body MRI magnet to shield the influence of an external magnetic field. The configuration of the EIS coil will be determined by various competing designing parameters: mutual inductance ( $M_{sm}$ ) with the magnet, the coupling factor ( $K$ ), and the screening factor ( $S$ ). The overall homogeneity in the imaging volume of the magnet produced by the induced current ( $I_s$ ) in the EIS coil is also a crucial design parameter. The EIS coil shares the same space as the main magnet inside the MRI cryostat. They remain in close proximity and outward of each coil of the magnet.

To design the EIS coil, there are a few input variables to begin with: the position of the EIS coil relative to each coil of the magnet, the size, or number of turns

in each EIS coil, the number of the EIS coils, and winding sense. The size of the EIS coil and its relative position are crucial in determining the screening factor and the coupling factor with the magnet. We have considered eight EIS coils, one each for each magnet coil, symmetrically positioned radially from the axis and with respect to the mid-plane in close proximity to each magnet coil and outward of each magnet coil. The iso-centers for the magnet and EIS coils are the same.

The schematic representation of the cross-section of one of the EIS coils and its relative position (axial and radial) with respect to its corresponding magnet coil is shown in Fig.5.4. In Fig.5.4,  $\Delta r$  signifies the radial separation between the EIS coil and the last layer of the corresponding magnet coil. It also signifies the radial position relative to its magnet coil. In Fig.5.4,  $OM$  is the axial symmetric line for an EIS coil and its corresponding magnet coil.

The winding width of the EIS coil is represented by  $(l_1 + l_2)$ . The relative values of  $l_1$  and  $l_2$  with respect to the  $Z_1$  and  $Z_2$  will define the axial positioning of each EIS coil. The axial dimension;  $(l_1 + l_2)$  eventually determines the number of turns in the EIS coil wound using a particular type of conductor. There is a single layer of conductor considered for each EIS coil in this present design. The WIC conductor used for the magnet coils is considered for the winding of each EIS coil.

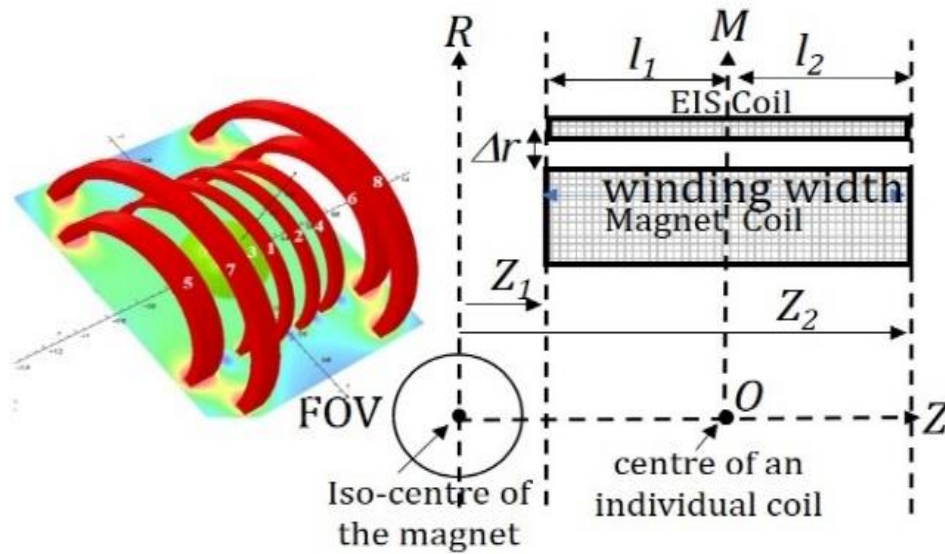


Figure 5.4 The schematic representation of the axial and radial position of one of the EIS coils relative to its associated magnet coil. Due to the axis symmetry configuration, one-half of the EIS coil and the associated magnet coil have been shown.

In the case of a superconducting magnet, an enormous amount of axial and radial stresses will be generated due to the Lorentz force. The over-binding layers are used on top of the primary coils to limit the radial movement of the coils due to the Lorentz forces. The EIS coil is wound on top of the over-binding layers. There are also intermediate layers of mylar for the electrical insulation. Hence the EIS coil is separated by a certain radial distance from the corresponding primary coil.

## 5.8 Design of EIS coil

To calculate the geometrical factor of the main magnet, it is essential to have all the relevant parameters of the magnet. The geometrical factor, which influences the magnetic field distribution, is determined using equation 5.17. Detailed parameters of the main magnet, including dimensions, and coil configurations, are provided in Table 5.3.

Table 5.2 Main magnet Configuration.

Coil	Center axial distance, Z (m)	Center radial distance, R (m)	Geometric factor, $g_m$ (T/A)
1	0.0956	0.5546	0.00091
2	0.0956	0.5546	0.00091
3	0.3020	0.5315	0.00077
4	0.3020	0.5315	0.00077
5	0.6392	0.5314	0.00084
6	0.6392	0.5314	0.00084
7	0.5848	0.8657	0.00073
8	0.5848	0.8657	0.00073
$g_m$			0.003591549

Table 5.3 Main magnet parameters.

Parameters	Values
Self-inductance	37.60 H
Geometric factor	3.6 mT/A
Stored energy	3.30 MJ

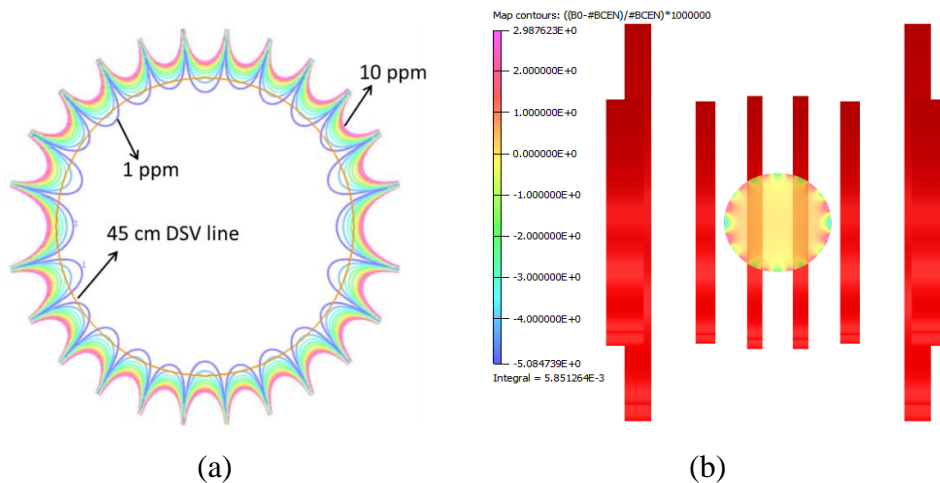


Figure 5.5 (a) Homogeneity in the FOV. (b) Homogeneity of the main magnet.

The homogeneity of the main magnet is a critical performance metric, indicating how uniform the magnetic field is within a specified volume. For the main

magnet in question, the homogeneity is around 10 ppm peak to peak within a 45 cm FOV. This means that the variation in the magnetic field strength is minimal, ensuring high precision for applications requiring a stable magnetic environment.

A contour plot visually represents this homogeneity. In the contour plot:

- The blue colour (In Fig. 5.5 (a)) indicates regions where the magnetic field deviation is within 2 ppm.
- The pink colour (In Fig. 5.5 (a)) marks areas where the deviation is within 10 ppm.
- The yellow circle delineates the 45 cm FOV, within which the main magnet maintains the specified homogeneity.

This plot provides a clear visual representation of the magnetic field's uniformity, highlighting areas with different levels of precision. The 45 cm FOV outlined by the yellow circle is particularly important as it represents the effective operational area where the magnetic field is sufficiently uniform for precise applications. Understanding these details is crucial for optimizing the performance and application of the main magnet in various scientific and industrial settings

## **5.9 Different EIS coil configurations and screening factor calculations**

Fig.5.6 illustrates the mounting arrangement of the EIS coil alongside the main magnet. In this set: C1, C2, C3, C4, C5, and C6 are the primary coils, responsible for generating the primary magnetic field. C7 and C8 are the shield coils, which are designed to reduce the stray magnetic fields. Each of these primary and shield coils has corresponding EIS coils, labeled as follows: S1, S2, S3, S4, S5, S6, S7, and S8 are the corresponding EIS coils that interact with the respective primary and shield coils.

The different configurations of these EIS coils and the calculated parameters for each configuration are shown in detail below. These configurations include the number of turns, the physical dimensions, the placement, and the inductance values.

The calculated parameters help in understanding the performance characteristics of each coil, such as the mutual inductance between the coils, the self-inductance of individual coils, and the coupling factors. This detailed information is crucial for optimizing the electromagnetic system for its intended applications, ensuring maintaining the field homogeneity.

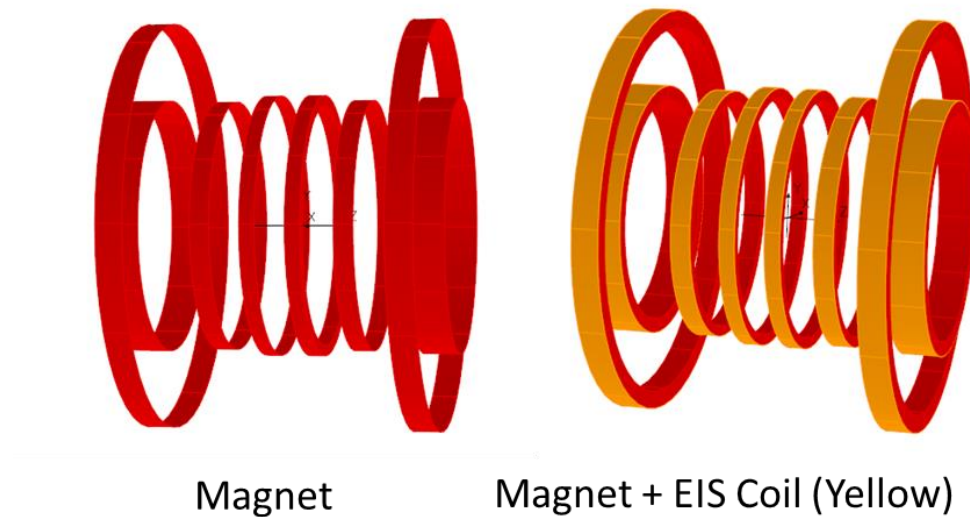


Figure 5.6 The position of the EIS coil concerning the main magnet.

EIS coil is wound over each of the main coils and the spacing between the EIS coil and the main coil is kept the same for each set of coils. The axial position of the EIS coil is different for each set of EIS and main coil combinations. The parameters are obtained using OPERA Software and analytical calculations.

### **Case 1: Uneven radial gap in each coil**

In this setup, the gap between the main magnet and the EIS coil varies among different coils. Specifically, for coils C1 and C4, the gap is maintained at approximately 3mm. For coils C5 and C6, this gap is increased to around 12mm. Meanwhile, for coils C7 and C8, the gap is further extended to approximately 32mm. This variation in gap measurements may be designed to achieve specific inductive properties or performance characteristics for each set of coils. The geometrical factor, which



influences the magnetic field distribution, is determined using Eq. 5.17 for the EIS coil, as shown in Table

Table 5.4 EIS coil parameters.

N (EIS coil)	main or eis coil center axial distance ( $Z = z$ ) (m)	EIS center radial distance (r)	Geometric factor, gs (T/A)
29	0.09563	0.5794125	3.01899E-05
29	0.09563	0.5794125	3.01899E-05
37	0.3020225	0.5548755	2.83741E-05
37	0.3020225	0.5548755	2.83741E-05
70	0.639224	0.5728775	2.28118E-05
70	0.639224	0.5728775	2.28118E-05
50	0.584829	0.9358475	2.04624E-05
50	0.584829	0.9358475	2.04624E-05
		Total gs	0.000203677

Table 5.5 The parameters of the EIS coil for case I.

Parameters	Values
Self-inductance	0.089 H
Geometric factor	0.02 mT/A
Stored energy	0.044 J
Mutual inductance	0.702 H
Coupling factor	0.384
Homogeneity	2.48
Screening factor	86.30 %

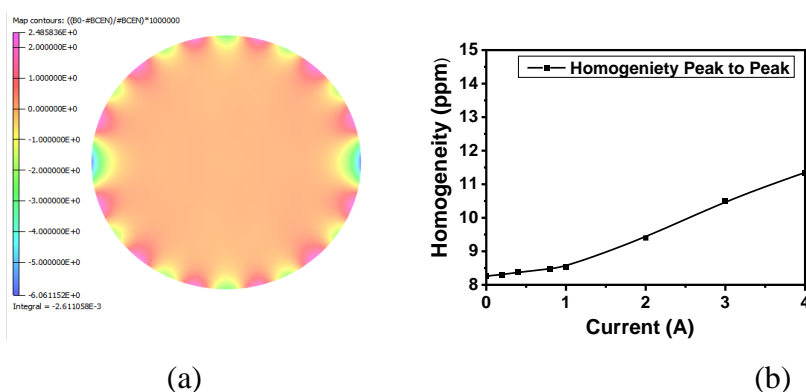


Figure 5.7 (a) Homogeneity of magnet and EIS coil in 45 cm FOV. (b) The homogeneity of magnet and EIS coil in 45 cm FOV for different induced currents.

The value of the geometric factor is also obtained by OPERA simulation software which is given in Table 5.6. Fig.5.7 shows the Homogeneity of the magnet and EIS coil in 45 cm FOV at 1A Current.

### Case 2: Even radial gap in each coil

In this setup, the radial gap between the main magnet and the EIS coils is consistently maintained at approximately 3mm across various coils. Specifically, for coils C1 and C4, the gap is around 3mm. This same gap measurement of about 3mm is also kept for coils C5 and C6, as well as for coils C7 and C8. The uniform gap across all these coils ensures consistent inductive properties and performance characteristics throughout the system. The geometrical factor, which influences the magnetic field distribution, is determined using Eq. 5.17 for the EIS coil, as shown in Table 5.7.

Table 5.6 EIS coil parameters.

N (EIS coil)	main or eis coil center axial distance ( $Z = z$ ) (m)	EIS center radial distance (r)	Geometric factor, gs (T/A)
29	0.09563	0.5794125	3.01899E-05
29	0.09563	0.5794125	3.01899E-05
37	0.3020225	0.5548755	2.83741E-05
37	0.3020225	0.5548755	2.83741E-05
70	0.639224	0.5638775	2.25692E-05
70	0.639224	0.5638775	2.25692E-05
50	0.584829	0.9068475	2.05516E-05
50	0.584829	0.9068475	2.05516E-05
		<b>Total gs</b>	<b>0.00020337</b>

Table 5.7 EIS Coil parameter for Case II.

Parameters	Values
Self-inductance	0.08 H
Geometric factor	0.002 mT/A
Stored energy	0.043 J
Mutual inductance	0.696 H
Coupling factor	0.386
Homogeneity	2.72
Screening factor	98.5 %

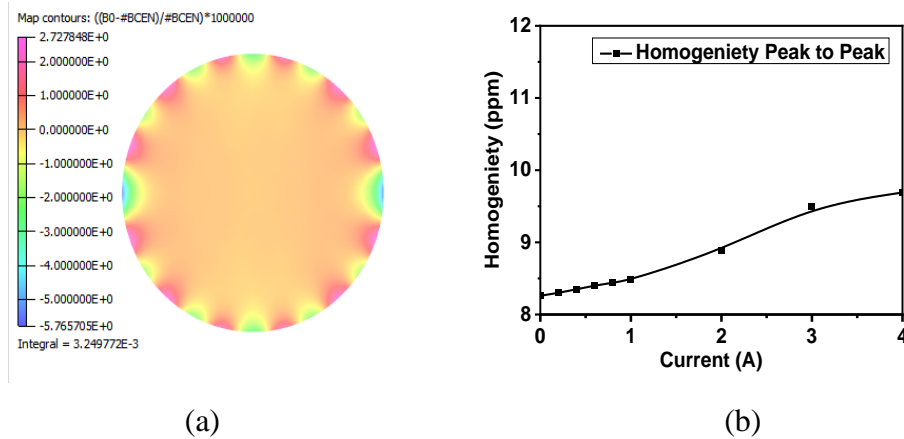


Figure 5.8 (a) Homogeneity of magnet and EIS coil in 45 cm FOV. (b) The homogeneity of the magnet and EIS coil in 45 cm FOV for different induced currents.

The value of the geometric factor is also obtained by OPERA simulation software which is given in Table 5.8. Figure 5.8(a) shows the homogeneity of the magnet and EIS coil in 45 cm FOV.

### 5.10 Result analysis of EIS coil

To understand the effect of radial separation, different cases of radial gaps: 5 mm, 10 mm, and 20 mm between the primary coil and the EIS coil are considered for this study. For each radial position, four sets (Case-1 to Case-4) of turns ratio between the EIS coil and the magnet coil are considered for the analysis. The details of the turn ratio for each set of the EIS coil are summarized in Table 2.

Where  $N_{S1,2}$  represents the number of turns in the EIS coil-1 (S1) or 2 (S2) and  $N_{C1,2}$  represents the number of turns in the magnet coil-1 (C1) or magnet coil-2 (C2). A similar nomenclature is followed for the remaining EIS and magnet coils. In Case-4, all the EIS coils have the highest turns ratio. The EIS coil in Case-1 has the lowest turns ratio. The turn ratios in the EIS coils of Case-3 and Case-4 are almost the same except for the innermost two coils; C1 and C2.

Table 5.8 The turns ratio between the EIS coil ( $N_s$ ) and the corresponding magnet coil ( $N_c$ ) for the Case-1 to Case-4.

Turns Ratio	Case-1	Case-2	Case-3	Case-4
$\frac{N_{S1,2}}{N_{C1,2}}$	0.0059	0.023	0.029	0.053
$\frac{N_{S3,4}}{N_{C3,4}}$	0.018	0.030	0.032	0.032
$\frac{N_{S5,6}}{N_{C5,6}}$	0.010	0.014	0.021	0.020
$\frac{N_{S7,8}}{N_{C7,8}}$	0.022	0.022	0.024	0.024

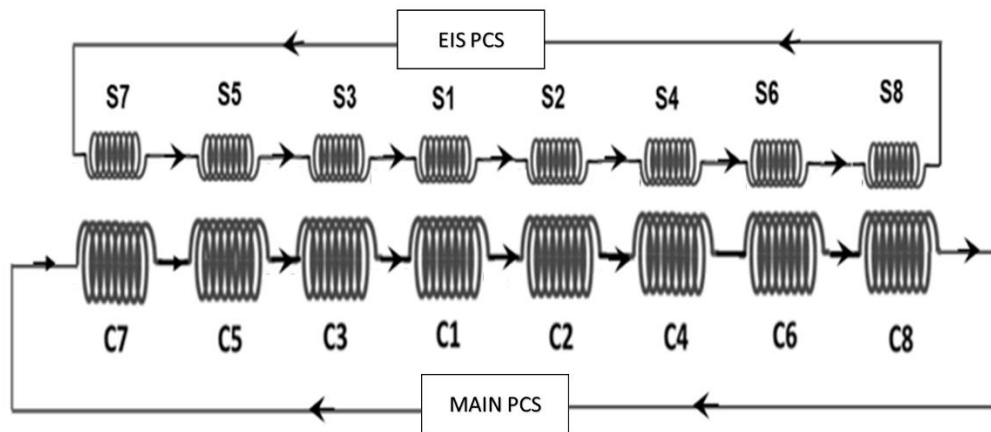


Figure 5.9 The simplified electrical scheme of the EIS coil and the magnet

The electrical scheme of a set of EIS coil and the magnet coil is shown in Fig.5.9. It shows that all the magnet coils are shorted through a PCS. Similarly, all the EIS coils are also shorted together through a separate PCS. When this shorted EIS coil is exposed to a varying, externally generated magnetic field, the total magnetic flux enclosed by the EIS coil remains constant. When the external field causes a change in magnetic flux in the EIS coil, the current in the EIS will be induced in a way so that the variation of the flux within the magnet will be equal but opposed to the external magnetic flux.

### 5.10.1 Geometrical factor:

The geometrical factors of the EIS coil for each case are estimated using Eq.5.10. The geometrical factor is the constants determined by coil geometry and expressed in Tesla per Ampere (T/A) that signifies that the field produced at its iso-center per unit amount of current induced in the EIS coil. Fig.5.10 shows the geometrical factor of the EIS coil for each case with a radial separation of 5 mm, 10mm, and 20 mm between the EIS coil and the corresponding magnet coil. It shows that the geometrical factor in Case-4 is the highest due to the highest number of turns ratio between the EIS coil and the corresponding magnet coil. The EIS coil in Case-1 has the lowest geometrical factor due to its lowest number of turns ratio between the EIS coil and the corresponding magnet coil. As the radial separation ( $\Delta r$ ) increases from 5 mm to 20 mm, the geometrical factor in each case is reduced by 1 %, as shown in Fig 5.10.

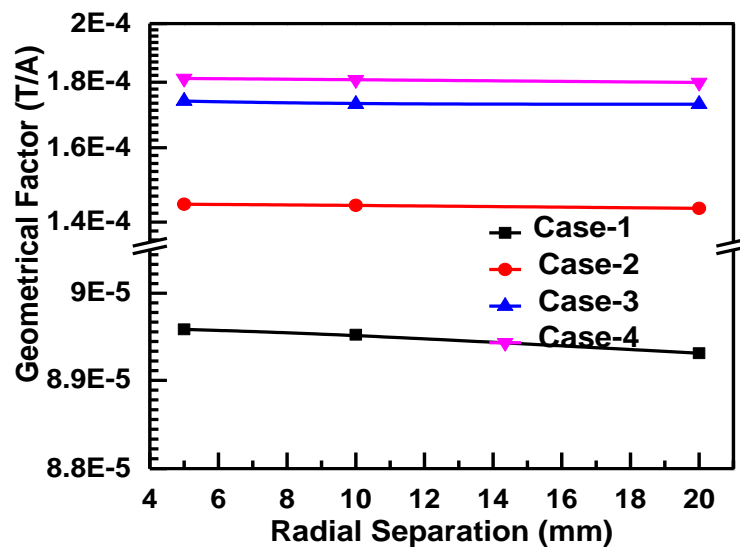


Figure 5.10 The geometrical factor of the EIS coil for each with radial separation of 5 mm, 10mm, and 20 mm between the EIS coil and the associated magnet coil.

### 5.10.2 Homogeneity

The flux conservation by the EIS coil does not guarantee the homogeneous field distribution in the FOV. A small amount of induced current through the EIS coil may deviate from the original field distribution profile. The external field interference which is coming from a remote source, may have different field profiles than the field profile by the induced current in the EIS coil. Adding these two opposing fields may not result in perfect cancellation at every point inside the FOV.

During the magnet's persistent operation, the magnet's current decays very slowly over time. This decay also causes a slow drift in the central magnetic field ( $B_0$ ) which eventually induces a current in the EIS coil. Over a period of time, this drift-induced current in the EIS coil may again alter the original field distribution in the FOV of the magnet.

Using the TOSCA code of the OPERA-3D program, the overall field homogeneity in the FOV at the iso-center of the magnet is estimated for each case (Case-1 to Case-4) by inducing 0.2 A, 0.5 A, 1 A, 2 A, 3 A, 4 A, 5 A of currents in the EIS coil. The overall homogeneity has also been analyzed in the FOV region for each case with the radial separation of 5 mm, 10 mm, and 20 mm between the EIS coil and the corresponding magnet coil.

Fig.5.11 shows peak-to-peak homogeneity in the FOV of 45 cm with induced current up to 5 A in the EIS coil with the radial separation of 5 mm between the EIS coil and the associated magnet coil. The '0 A' at the x-axis in Fig 5.11 signifies the peak-to-peak homogeneity (7 ppm) in the 45 cm of FOV of the magnet without the EIS coil. The homogeneity is found to deteriorate in the FOV as soon as some finite amount of current is induced in the EIS circuit for all the cases except in Case-1.

The homogeneity in Case-1 improves initially till 0.5 A of current in the EIS coil, and then it starts fast deterioration, as shown in Fig.5.11. It has the lowest turns ratio among the four cases as given in Table 5.9. The highest deterioration in the homogeneity is observed in Case-1 and Case-4. The homogeneities in both cases exceed the predefined limit of 10 ppm ( $\pm 5$  peak-to-peak) at 1.5-2 A of induced current

in their EIS coils as shown in Fig.5.11 In Case-3, the homogeneity deteriorated with the induction of current but did not exceed the predefined limit of 10 ppm (peak-to-peak) even up to 5 A of induced current. The peak-to-peak homogeneity in Case-2 reaches up to 11.5 ppm at 5 A of induced current. As the radial separation between the EIS coil and the magnet coil is increased in each case, a 5-8 % increment in the deterioration of homogeneity is observed as shown in Fig.5.11. Hence the EIS coils in Case-2 and Case-3 generate better homogeneity at the iso-center of the MRI magnet. There is no significant change in inhomogeneity in case of an increase in radial gap.

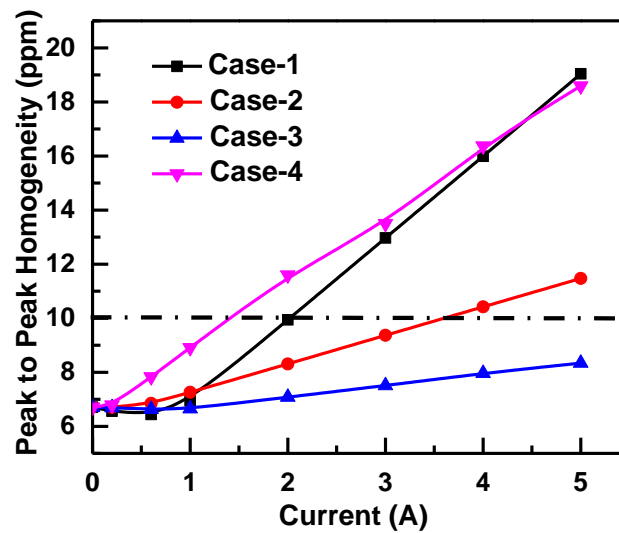


Figure 5.11 The peak-to-peak homogeneity in the FOV of 45 cm at the iso-center of the magnet with the induced current up to 5 A in the EIS coil with radial separation of 5 mm between the EIS coil and the associated magnet coil.

### 5.10.3 Mutual inductance and coupling factor

Fig.5.12 shows the mutual inductances between the EIS coil and its corresponding magnet coil in four cases with three values of radial separations (5 mm, 10 mm, and 20 mm) between them. The highest mutual inductance is found to be in Case-3 and Case-4, which is in the range of 0.55-0.58 H. Case-1 shows the lowest mutual inductance of 0.18 H. As the radial separation is increased, the mutual inductance is reduced, especially in Case-3 and Case-4. In Case-1, the mutual inductance almost

remains the same. The higher mutual inductance between the EIS coil and the magnet coil signifies stronger coupling, which is unacceptable.

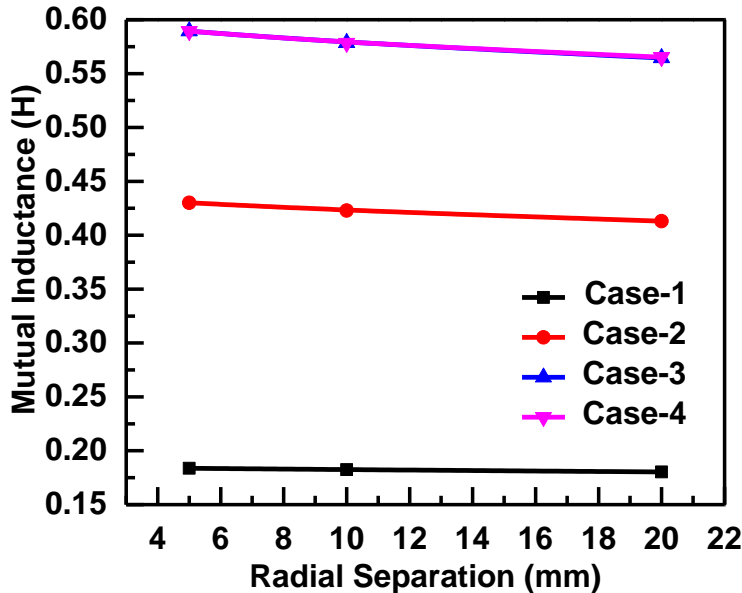


Figure 5.12 The mutual inductance between the EIS coil and the magnet coil for all four cases (Case-1 to Case-4) with the radial separation of 5 mm, 10 mm, and 20 mm between them.

The higher mutual inductance would eventually lead to a higher coupling factor between them. The behaviour is reflected in Fig.5.12 of coupling factors ( $K$ ) for all four cases (Case-1 to Case-4) with the radial separation of 5 mm, 10 mm, and 20 mm. The coupling factor plays an important role in designing of any EIS coil; it gives the fraction of magnetic field links due to currents induced in one coil due to the field change in another coil. Using Eq. (5.20), each case's coupling factor ( $K$ ) is estimated with three values of radial separations between the EIS coil and the corresponding magnet coil. At 5 mm of the radial separation, the lowest coupling factor (i.e., the weakest coupling) is found to be 0.18 for Case-1. The highest coupling factor (i.e., the strongest coupling) is found to be 0.38 in Case-3 and Case-4 due to their higher turn's ratio between the EIS coil and the corresponding magnet coil. As the radial separation



between the EIS coil and the magnet coil increases in each case, the coupling factor is reduced by an average value of 5 % in each case, as shown in Fig.5.13.

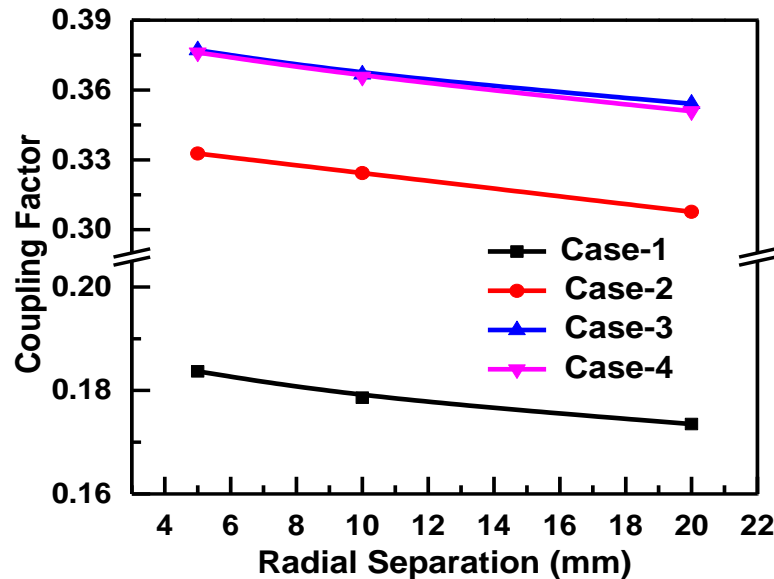


Figure 5.13 The coupling factor between the EIS coil and the magnet coil for all four cases (Case-1 to Case-4) with the radial separation of 5 mm, 10 mm, and 20 mm between them.

#### 5.10.4 Screening factor

The screening factor ( $S$ ) is one of the most crucial parameters for designing any EIS coil. It signifies how effectively the magnet is shielded from the influence of any external interference. Using Eq. (5.25) and Eq. (5.26), the screening factor for each set of EIS coil is estimated. Fig.5.14 shows the screening factor for all four cases of EIS coil with the radial separation of 5 mm, 10 mm, and 20 mm.

$$S(\%) = \left(1 - \frac{dB_0}{dB_d}\right) \times 100\% \quad (15)$$

The screening factor in percentage signifies the change in the central magnet field ( $B_0$ ) per hundred changes in the external field ( $B_e$ ). The shielding factor or screening factor

should be as high as possible to effectively shield an external magnetic field. The screening factor for the EIS coil for Case-1 is found to be the lowest. It varies in the 85-86 % range with the variation of the radial separation between the EIS coil.

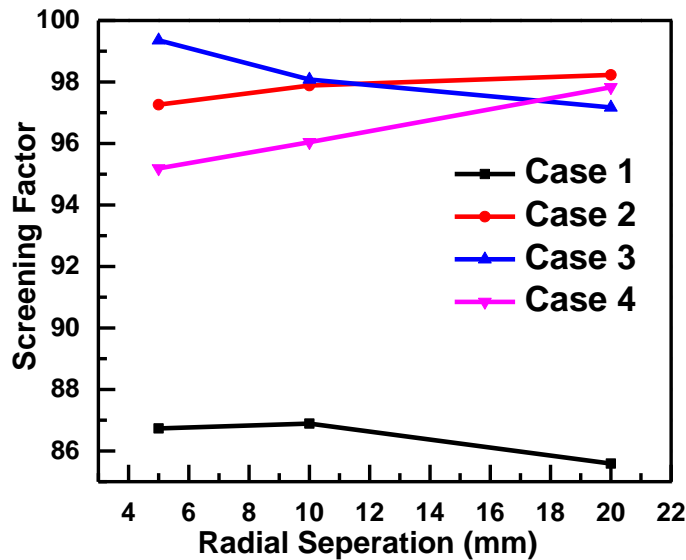


Figure 5.14 The screening factor (in %) of the EIS coil in each case (Case-1 to Case-4) with the radial separation of 5 mm, 10 mm, and 20 mm between the EIS coil and the corresponding magnet coil.

The screening factor remains greater than 95 % for all other cases of EIS coils. The screening factor of the EIS coil for Case-2 and Case-4 shows improvement (signifies improvement) as the radial separation between the magnet coil and the corresponding EIS coil increases. In Case 3, the screening factor deteriorates as the radial separation between the EIS coil and the corresponding magnet of the coil is increased. At 10 mm of radial separation, the screening factors for Case-2 and Case-3 are the same. Hence, the EIS coils in Case-2 and Case-3 provide better shielding of the external interference in the FOV of the present MRI magnet. The screening efficiency of case 2 and case 3 is in the range of 99 % means only around 99 % of disturbance was eliminated; only 1% was present.

### 5.11 Induced current during quench

Typically, the temporal stability of the MRI magnet is better than 0.1 ppm /hr. The corresponding field decay in the primary coils will though slowly induce current into the EIS coil but will not be able to quench the EIS circuit. Periodic intentional quenching of the EIS circuit will reset such accumulated current. Whereas during a quench in the MRI magnet, the magnetic field would be reduced to zero within a few seconds. The fast change in the magnet's field may induce a large current in the EIS coil despite their weak coupling. The quenching of the MRI magnet can happen in two scenarios: (1) during the ramping up of the magnet (i.e., the training quench) and (2) during the persistent operation of the magnet.

During the ramping up of the magnet, the PCS of the EIS coil will be at a normal state. During the magnet's persistent operation, the EIS coil's PCS will be in a superconducting state. Despite the weak coupling between the EIS coil and the magnet coil, the EIS coil would try to conserve the flux during quench in either condition. The amplitude of the induced current in the EIS coil would depend on the thermal state (superconducting state or normal conducting state) of the PCS of the EIS coil.

If the magnet quenches during its persistent operation, the induced current in the EIS coil will be significantly higher. Similarly, Fig.5.15 shows the induced eddy current in the EIS coil for all cases (Case-1 to Case-4) with 10 mm of radial separation between the EIS coil and the corresponding magnet coil in correlation with the current decay of the magnet during a quench when the PCS of the EIS coil is at normal state (during ramping up of the MRI magnet). The formation of the eddy-current peak in all cases happens at the same time, i.e., at 2.25 s after the quench. The peak eddy currents in the EIS coil for Case-2 to Case-4 are the same, which is ~ 1.5 A. In Case-1, the peak value of the eddy current is ~10 % less in comparison to other cases due to its lowest coupling factor (in Fig. 5.13).

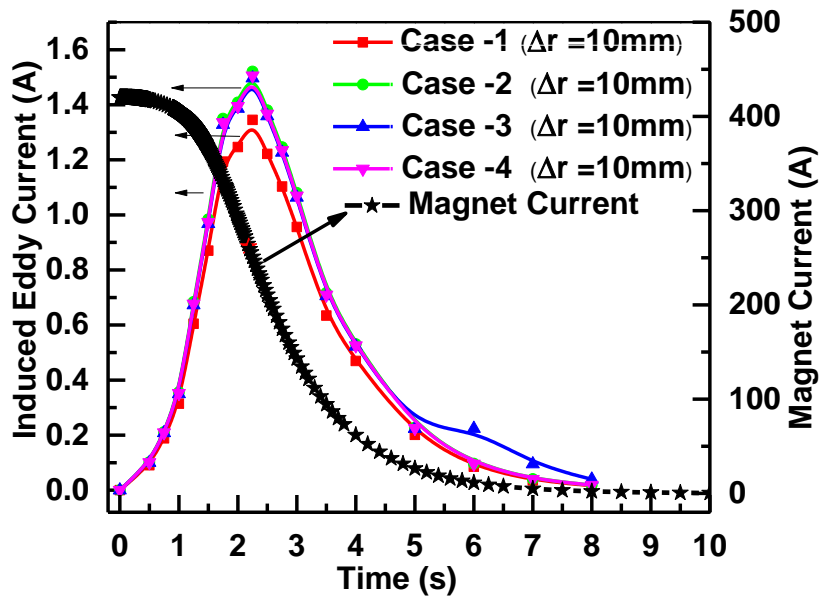


Figure 5.15 The quench-induced eddy current in the EIS coil of all cases (Case-1 to Case-4) in correlation with the magnet's current decay when the EIS coil's PCS is at normal state (quench during ramping up of the MRI magnet).

If the magnet quenches during its persistent operation, the induced current in the EIS coil will be higher due to the prevailing superconductive state of the EIS circuit. Fig.5.16 shows the quench-induced eddy current in the EIS coil in all four cases (Case-1 to Case-4) with 10 mm of radial separation between the EIS coil and the corresponding magnet coil. It shows that the critical currents in the EIS coils of Case-1 and Case-3 are attained in 0.58 s and 0.47 s, respectively. The weak coupling of the EIS coil of Case-1 due to its smaller turn ratio makes the time period to attain the critical current longer. Hence, the PCS of the EIS coil would be quenched automatically when the induced current in the EIS coil exceeds the critical value.

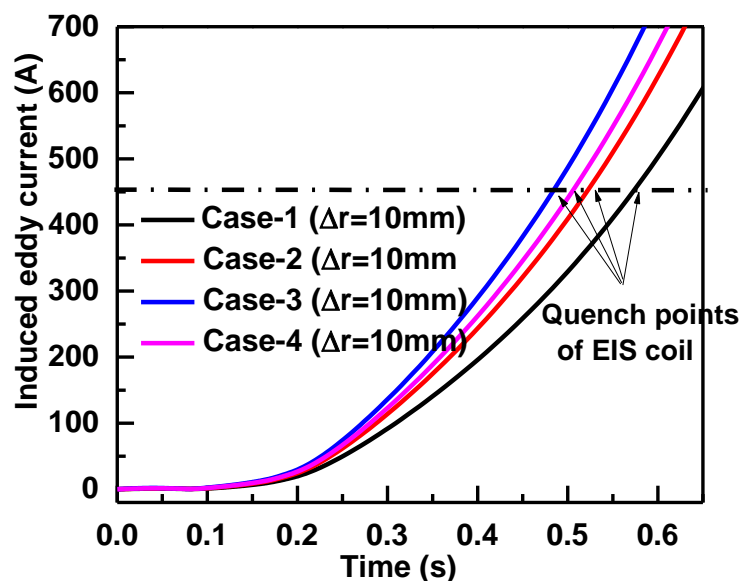


Figure 5.16 The quench-induced eddy current in the EIS coils of all four cases (Case-1 to Case-4) during persistent operation of the MRI magnet (EIS circuit is in a superconducting state)

## 5.12 Design and experimental test setup of the PCS

The PCS was made using a multi-filamentary CuNi-NbTi conductor with a diameter of 0.75 mm. It has 18 filaments of NbTi, each having a diameter of 105  $\mu$ m. The critical current of the CuNi-NbTi conductor is 250 A at 5 T. The average normal resistance of the conductor at 300 K is 1.05  $\Omega$ /m. The photograph of the PCS is shown in Fig.5.17. The former of the PCS was made of insulating material. The bifilar winding technique was used for the PCS to achieve lower self-inductance ( $\sim$ 5  $\mu$ H). The total normal resistance of the PCS at 300 K and 15 K is 40  $\Omega$  and 15  $\Omega$ . Table 5.10 summarizes the design parameters of the PCS. Its winding pack was impregnated with stycast 2850 FT. A film heater-1 (FH1) having electrical resistance of 90  $\Omega$  was placed between the two intermediate layers of the PCS. A silicon diode temperature sensor was placed at the intermediate layer to measure its temperature.



Figure 5.17 The PCS mounted onto the 1.5 T MRI magnet.

Table 5.9 Design parameters of the PCS.

<b>Description</b>	<b>Value</b>
Superconductor (SC)	CuNi-NbTi
Critical Temperature	9.2 K
Total length of the conductor used in PCS	38.1m
Normal Resistance at 300K	40 $\Omega$
Inductance	5 $\mu$ H

Fig.5.18 shows the schematic of the experimental test setup at 4.2 K. The film heater (FH1) of the PCS is connected to a DC power supply (24 V, 0.5 A) i.e., the EIS PCS controller, as shown in Fig.5.20. The PCS is connected to a separate DC power supply (24 V, 0.5 A) to feed the current through the PCS at the normal condition to measure the normal resistance. The voltage across the film heater and the PCS was simultaneously measured using a digital oscilloscope which was interfaced with a laptop for data recording.

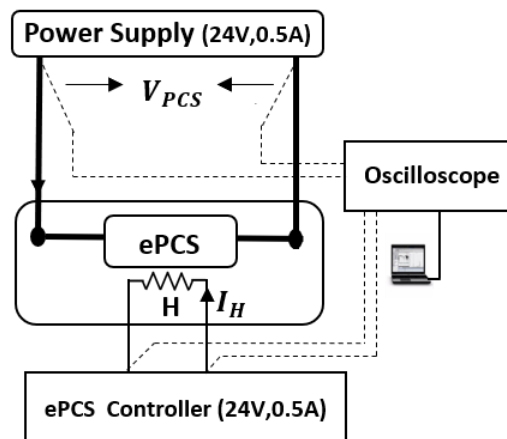


Figure 5.18 The schematic diagram of the setup for testing the PCS of the EIS circuit.

Fig.5.19 shows the voltage and the temperature profile of the PCS of the EIS circuit with 100 mA of current through the FH1. The temperature of the PCS was measured to be 5.3 K, thereby indicating a superconducting state. The resistance was measured by feeding 250 mA of current through the PCS. The PCS's temperature was increased by 0.3 K while feeding the current through the PCS. The voltage measured across the PCS was less than 1 V, as shown in Fig.5.19. Therefore, the resistance calculated for the PCS is  $\sim 3.5$  W, signifying a partial quench of the PCS.

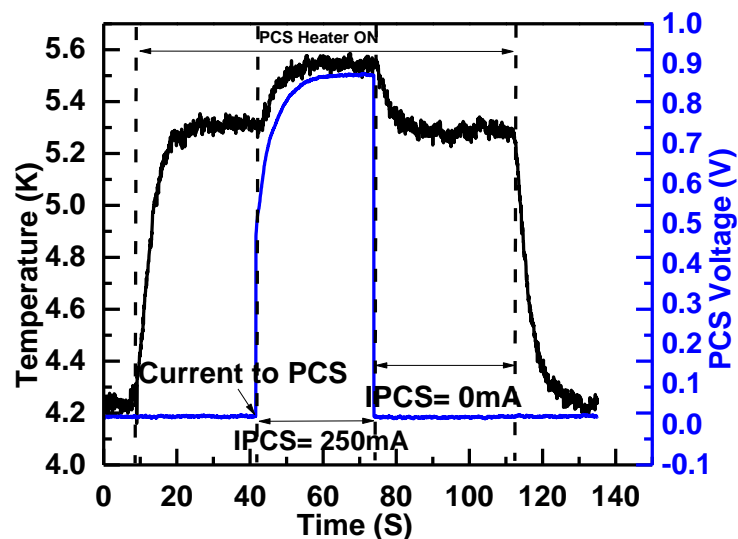


Figure 5.19 The PCS's temperature and voltage profile with 100 mA of current through the FH1 and 250 mA current through the PCS.

To achieve the full quench of the PCS, its heater was fed 250 mA of current. Fig.5.20 shows the voltage and the temperature profile of the PCS of the EIS circuit with 250 mA of current through the FH1. The temperature of the PCS was measured to be 9.5 K, indicating a normal state. The normal resistance was again measured by feeding 250 mA of current through the PCS. The PCS's temperature was increased by 0.4 K while feeding the current through the PCS. The voltage measured across the PCS was  $\sim 2.5$  V, as shown in Fig.5.22. Therefore, the normal resistance calculated for the PCS is  $\sim 10$  W, signifying the full quench of the PCS.

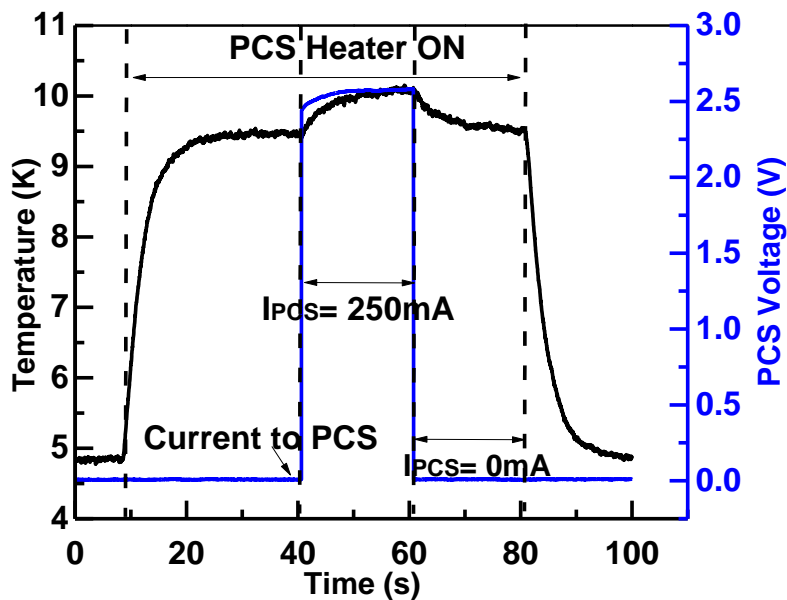


Figure 5.22 The temperature and the voltage profile of the PCS with 250 mA of current through the FH1 and 250 mA of current through the PCS.

### 5.13 Summary

A detailed study has been carried out on several competing parameters, namely, mutual inductance, the coupling factor, the homogeneity, and the screening factor, for several configurations of EIS coil having different values of turns ratio and the radial separation between each EIS coil and the corresponding magnet coil. The number of turns in each EIS coil would eventually determine the winding width, i.e., the axial



width of each coil. Hence the variation in the turns ratio in the EIS coils signifies the variation of their axial width in each coil. The axial width of each EIS coil plays a much bigger role than the radial separation in generating better peak-to-peak homogeneity in the FOV at the iso-center of the MRI magnet. The higher turns ratio, increases the mutual inductance and the corresponding coupling factor but provides better screening factors. The moderate turns ratio in the EIS coil of Case-2 and Case-3 provides better homogeneity and the screening factor for the given 1.5 T MRI magnet. A moderate amount of radial separation is considered for the present design of the EIS coil. The current induced in the EIS coil during the quench in the MRI magnet at different working scenarios is also analysed in detail.

Also, a PCS for the EIS coil of the 1.5 T MRI magnet has been designed, fabricated, and tested in liquid helium. A comparative analysis of the temperature profile and switching behaviour was analysed. The current for the heater for the normal transition was finalized to be 250 mA.

## **CHAPTER 6**

### **EIS BYPASS DIODES**

#### **6.1 Introduction**

The power diodes play a vital role in the operational aspects of a superconducting magnet. The selection of the diodes is crucial for optimal performance and reliability. These diodes are placed within the magnet cryostat, which subjects them to liquid helium (4.2 K) or cryogenic temperatures. The behavior of the diodes can change significantly at cryogenic temperatures. Hence, it is essential to characterize the behavior before they are installed onto a superconducting magnet system. In this chapter, the testing procedures and results for the two power diodes at temperatures of 300 K, 77 K, and 4.2 K were discussed in detail.

## 6.2 EIS bypass diodes

To protect the magnet against such external disturbances, external interference screening (EIS) coils are used, which are wound over each of the eight coils and shorted via a separate PCS [78-81]. External field disturbances induce a persistent current in the EIS coils that produce a field that is equal to and opposite the external field, which prevents distortion in the main field  $B_0$ . To protect the PCS against the excessive current that can be induced during the quench of the main magnet or any other eventuality, a bypass path consisting of a set of back-to-back power diodes is provided. The behavior of the power diodes can change significantly at cryogenic temperatures. Hence, studying their performance before installing them onto a superconducting magnet system is essential. Various research groups [61-64] have used different methods to protect the PCS in the main magnet, and EIS.

The characteristics of power diodes at 77 K at the liquid nitrogen boiling point have been the subject of a sizable number of investigations [116]. However, limited studies on power diodes at liquid helium temperature (4.2 K) are available [9-10,12]. The primary properties that have received the most attention are as follows: a) forward voltage, which typically increases at cryogenic temperatures; b) reverse (breakdown) voltage, which falls by about 20 %; c) resistance, which falls [117-121]; and d) reverse recovery characteristics, which typically increase at cryogenic temperatures and cut switching losses by 80 % [117-121]. However, because all the specific semiconductor components behave differently, the information provided in these articles is not general.

As discussed earlier, an MRI magnet runs in the persistent mode through a PCS. The PCS has a non-inductive superconducting coil, and a heater wound over it, as shown in Fig.3.1. For magnet energization, the heater is 'switched on,' which turns the PCS to the normal state. The current starts flowing through the magnet. Once the field is ramped up to the required field, the heater current is 'turned off.' The current now flows persistently through the magnet in a closed loop without dissipation, and the magnet power supply is disconnected, which produces a field with unprecedented stability.

The simplified electrical scheme of the main magnet coils and the EIS coils is shown in Fig.6.1. Each PCS is linked in series with the respective circuits, one for the main magnet circuit (MAIN PCS) and the other for the EIS circuit (EIS PCS). These PCSs enable the main magnet and EIS coils to run in the persistent mode. Two sets of back-to-back power diodes are connected in parallel with the MAIN PCS and the EIS PCS. These diodes protect the PCS coils against the excessive current built up during the magnet quench or during any eventuality thereby providing an alternate parallel current path.

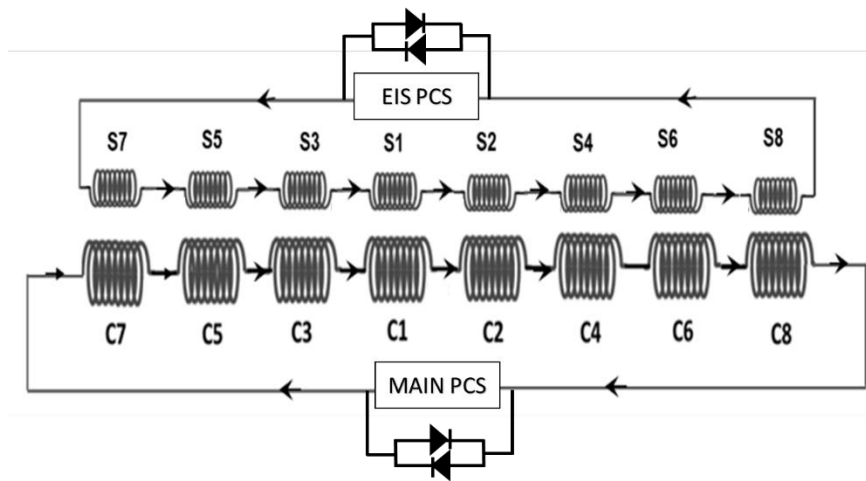


Figure 6.1 Simplified electrical scheme of the magnet circuit and the EIS circuit of an MRI magnet.

### 6.3 Diode parameters

Based on the simulation results explained in Chapter 5 and considering the current carrying capacity of EIS coils, two types of power diodes were selected for characterization. Fig.6.2(a) shows a standard recovery diode (Stud Version) 70 HFR 120, and Fig.6.2(b) shows an ultrafast avalanche sinter glass diode BYV 28-200 [16-17]. The specifications of these diodes are summarized in Tables I and II. These diodes have been tested at room temperature and at cryogenic temperature.

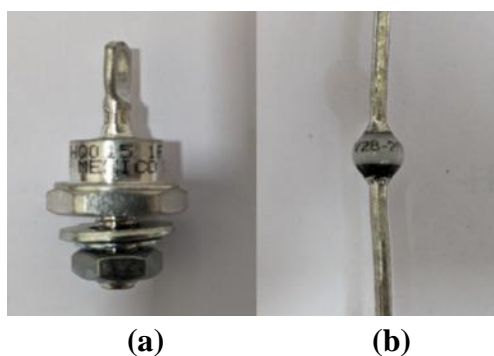


Figure 6.2 (a) Vishay diodes: (a) standard recovery diode (stud version) 70 HFR 120 [122]; (b) Ultrafast avalanche sinter glass diode BYV 28-200 [123].

Table 6.1 BYV 28-200 diode parameters.

Items	Value
Make	Vishay
Part No.	BYV 28-200
Forward Voltage	1.1 V @ 25 °C
Forward Current ( $I_F$ )	3.5 A
Reverse Voltage ( $V_R$ )	200
Junction operating Temp	- 55 to 175 °C
Casing	Sintered Glass Case
Weight	858 mg

Table 6.2 70 HFR 120 diode parameters.

Items	Value
Make	Vishay
Part No.	70 HFR 120
Forward Voltage	1.35 V @ 25 °C
Forward Current ( $I_F$ )	70 A
Reverse Voltage ( $V_R$ )	1440
Junction operating Temp	- 65 to 180 °C
Casing	Aluminum body
Weight	1200 mg

These power diodes are classified as standard recovery diodes (70 HFR 120) and fast recovery diodes (BYV 28-200). In the fast recovery diodes, as the name indicates, the recovery time ( $t_{rr}$ ) and the recovery charge ( $Q_{rr}$ ) are reduced by the lifetime control of the minority carrier, which enhances the recombination process. Because of this, the diodes have a higher conduction drop (1.1 V). The BYV 28-200

diode has a current rating of 3.5 A, whereas the blocking voltage rating of 200 V has the following ratings:  $V_{FM}$ - 1.1 V,  $I_{RRM}$ - 1  $\mu$ A, and  $t_{rr}$  - 30 ns. The standard recovery diodes 70 HFR 120 have a lower conduction drop (considering the same rating) but a higher  $t_{rr}$  [124].

#### 6.4 EIS PCS diode assembly

The EIS PCS assembly consists of two sets of series-connected diodes connected in the back-to-back configuration, as shown in Fig.6.3. The diodes are mounted on an L-shaped copper plate. Using two diodes (series connected) ensures that the bypass path remains active even when one of the diodes fails.

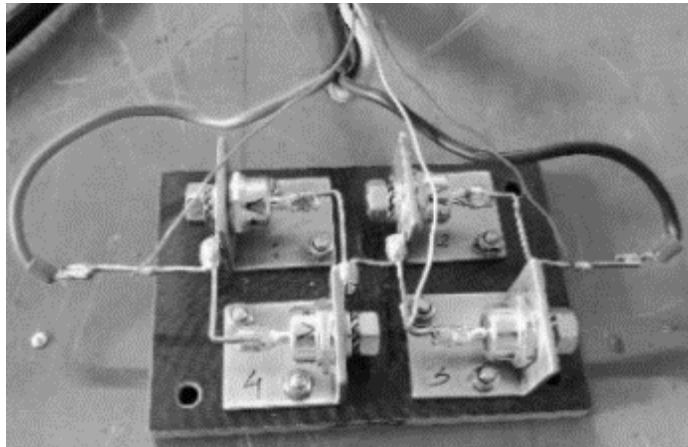


Figure 6.3 The back-to-back diode assembly of EIS circuit.

#### 6.5 Forward voltage test

A forward voltage test is conducted on the devices shown in Fig. 3. The testing of diodes is performed at room temperature, at 77 K reached when using liquid nitrogen, and at the 4.2 K reached using liquid helium. A KEPCO power supply (72 V @ 6 A) is used for their characterization at various temperatures. A simplified schematic of the test circuit is shown in Fig.6.4.

A diode is connected in the forward bias configuration with a power supply, which is in the current-driven mode, as shown in Fig.6.5. A  $5\ \Omega$  current limiting resistor and a shunt resistor of  $0.1\ \Omega$  are connected in series with the power supply. The shunt resistor is connected to monitor the supply current. The voltage taps are connected across the diode to monitor the forward voltage. The 77 K test setup is shown in Fig. 7. A double-walled vacuum jacketed cryo-bucket is used to carry out the V-I characterization at 77 K using liquid nitrogen. The temperature of the liquid bath was maintained during the measurement.

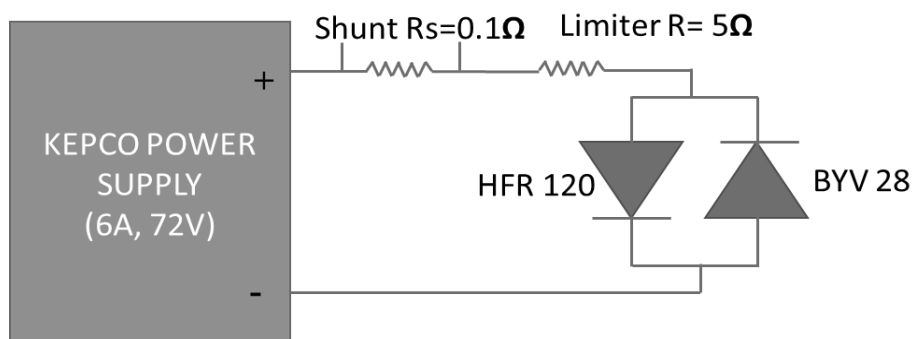


Figure 6.4 Simple electrical circuit diagram for the V-I characterization of the diodes.

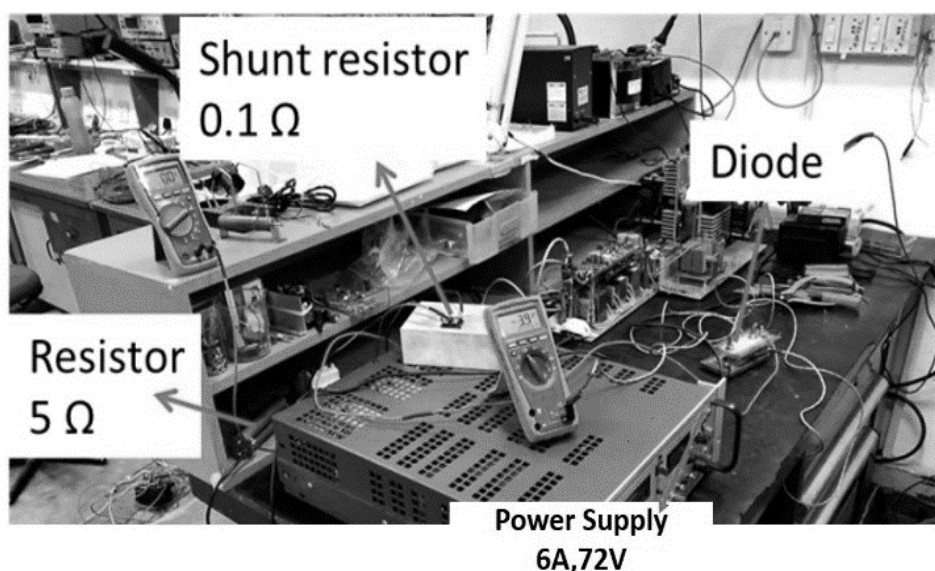


Figure 6.5 Photograph of the experimental test set up for the V-I characterization of diodes at room temperature (300 K).



Figure 6.6 Photograph of the experimental test set up for the V-I characterization of diodes at 77 K.

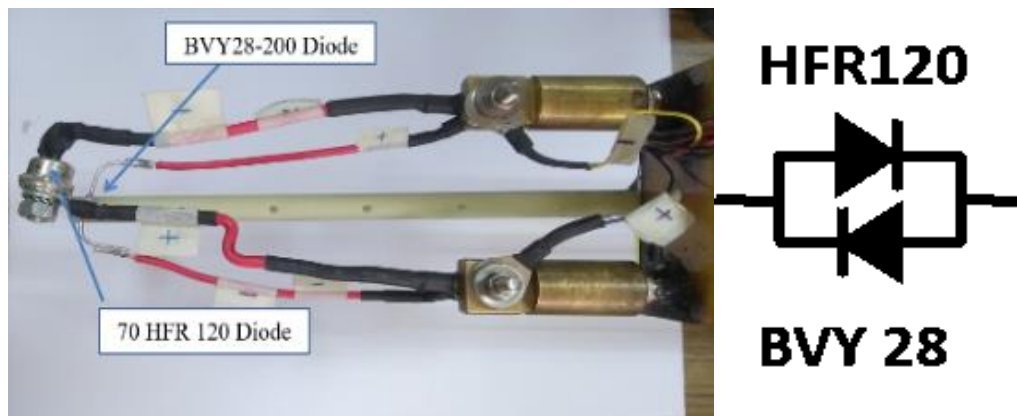


Figure 6.7 Mounting configurations for two diodes on a fixture.

A separate test setup was used for the V-I characterization of the diodes at 4.2 K when using liquid helium. Both the stud and fast recovery diodes were mounted in the back-to-back configuration for their low-temperature V-I characterization. The mounting schemes of the diodes are shown are in Fig.6.6.



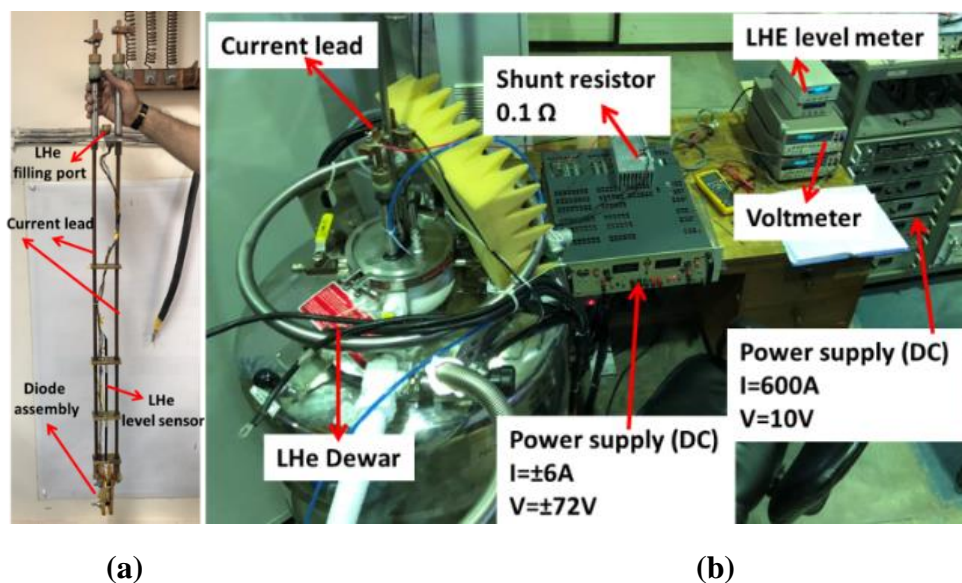


Figure 6.8 (a) Photograph of the 4.2 K test probe for the diodes; (b) V-I characterization test setup of the diodes at the temperature of LHe (4.2 K).

The test probe and test setup used for characterization at 4.2 K are shown in Fig. 6.8(a) - Fig. 6.8(b). The V-I characterization was limited to the operating current of 5 A to match the simulation of the induced current. The forward voltage of the diode was monitored under a continuous supply of DC current (~5 A) for a prolonged period, which ensures the long-term forward voltage stability of the diode.

The test setup used for the V-I characterization of the EIS PCS diode assembly as shown in Fig. 6.5 at 300 K and 77 K is shown in Fig.6.9. A Danfysik system 9100 magnet power supply (200 A, 10 V) is used for the characterization of the diodes at 300 K and at 77 K. The voltage taps used across each of the diodes were used to measure the forward voltage. A forward current of up to 5 A was applied to each of the diodes in steps.



Figure 6.9 Test setup of the PCS diode assembly at room temperature (300 K).

## 6.6 Results and discussion

V-I characterization results of HFR 120 and BYV 28-200 diodes at 300 K, 77 K, and 4.2 K are shown in Fig.6.10, Fig.6.11, and Fig.6.12, respectively. The forward voltage of the diodes at 300 K is around 0.6 to 0.7 V and at 77 K it is around 0.9 and 1 V for BVY 12 and HFR 120 diode respectively. At 4.2 K, the forward voltage of the HFR 120 is  $\sim 4.78$  V, and for the BYV 28-200, it is  $\sim 4.5$  V. The current carrying capacity of the BYV 28-200 is smaller than that of the HFR 120 diode, as mentioned in section 6.2. As shown in Fig.6.12, the curve displays a drop in the voltage while the forward current increases from 1 A to 2 A. Hence, it exhibits a negative differential resistance (NDR) region in the V-I curve. The Ohm's law still holds in the linear region of the V-I curve. However, it is not applicable in the NDR region. The reason behind such a high degree of reduction in the forward voltage is due to the high amplitude of the forward current flowing through the junction of the diode, which causes a substantial amount of joule heating, which generates a localized heated zone that eventually spreads throughout the junction. When the localized temperature increases, the forward voltage of the diodes decreases. The NDR does not create any problem for applications. The main parameter is the threshold forward voltage that is used to start bypassing the current of the EIS PCS in case of any eventuality. Once the diode starts

conducting, the current of the EIS circuit starts dissipating through the diodes resulting in a reduction of the current in the circuit.

During the forward bias, the diode can be represented by an offset junction drop and an equivalent series resistance that slopes positively in terms of the V-I characteristics. The diode has a typical forward conduction drop of 0.7 V that increases with a reduction in the junction temperature. The forward voltage of the power diodes was increased up to 6.5 times at 4.2 K. Similarly, the forward voltage of the diodes increased up to 1.71 times when it was cooled to 77 K. The increase in the forward voltage observed at lower temperatures is caused by a reduction in the carrier density at cryogenic temperatures. The junction starts behaving like an insulator. The following factors contribute to the change in forward voltage at low temperatures.

1. The carrier density is affected by the junction temperature.
2. When the carrier density is low, the junction temperature acts as an insulator at low temperatures.
3. In terms of the junction voltage at the junction region, the transport current flows easily across weak places. This occurs because the current moves locally, and has a high current density. Because of the high-power density of joule heating, this region is heated up rapidly [117-121].

Considering the current carrying capacity and observing the V-I characteristics of both diodes, the HFR 120 diode was selected for EIS PCS protection purposes. The EIS PCS diode assembly is placed in a region with a minimum background field (< 0.6 T) inside the MRI magnet system to minimize the field-induced effects. The effect of the magnetic field on the forward voltage appears to be favorable when the field and current travel the same through the diode [120]. In the experimental system, the diodes were placed in such a way that the magnetic field is parallel to the flow of the current from the diodes.

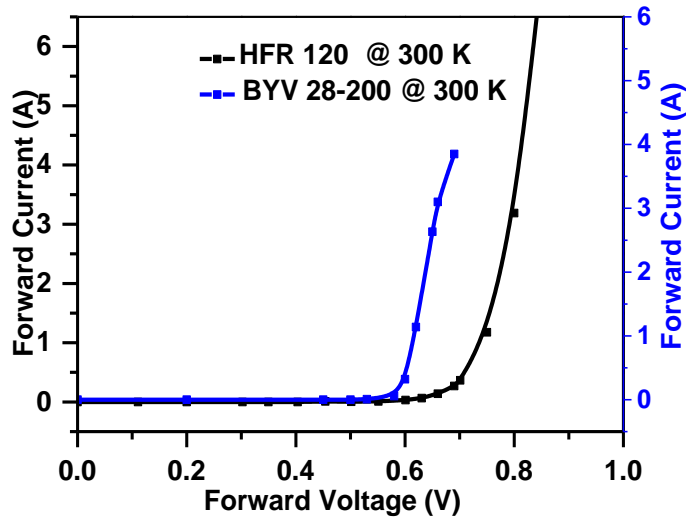


Figure 6.10 Forward characteristics of HFR 120 and BYV 28-200 diodes at 300 K.

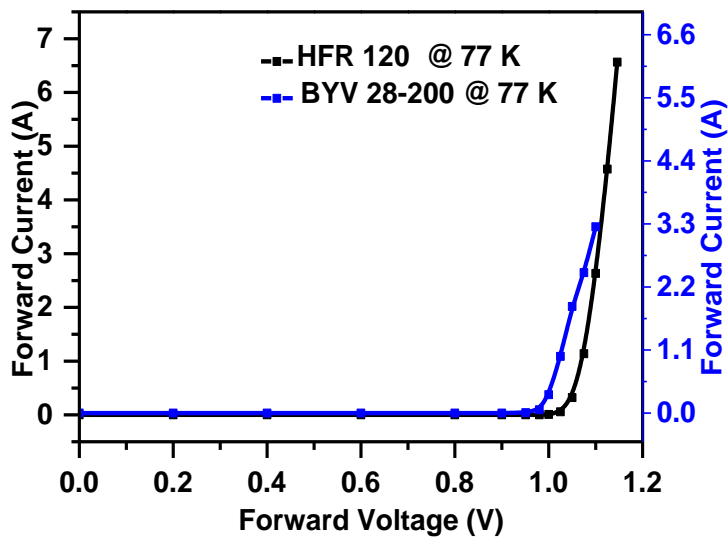


Figure 6.11 Forward characteristics of HFR 120 and BYV 28-200 diodes at 77 K.

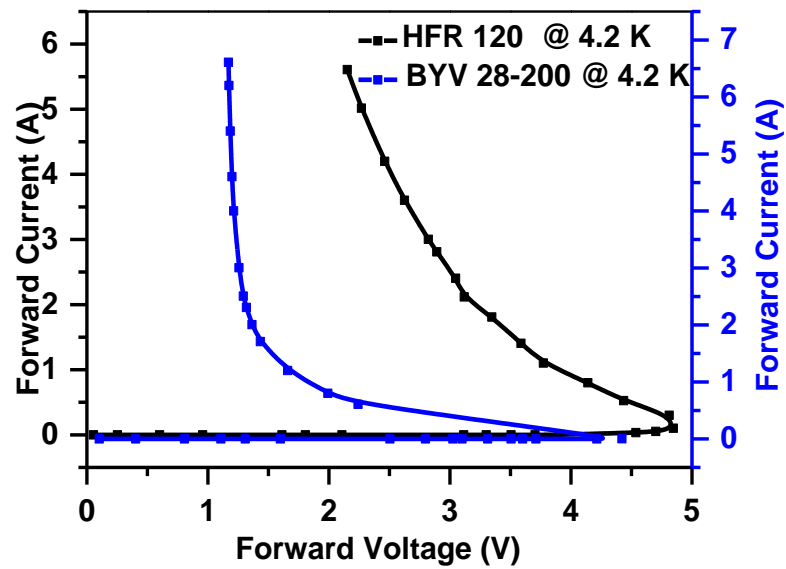


Figure 6.12 Forward characteristics of HFR 120 and BYV 28-200 diodes at 4.2 K.

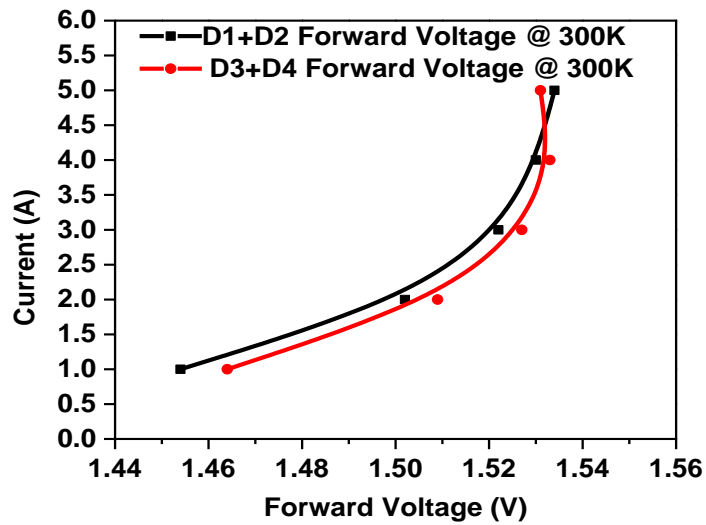


Figure 6.13 Forward characteristics of the back-to-back diode assembly of the PCS at 300 K.

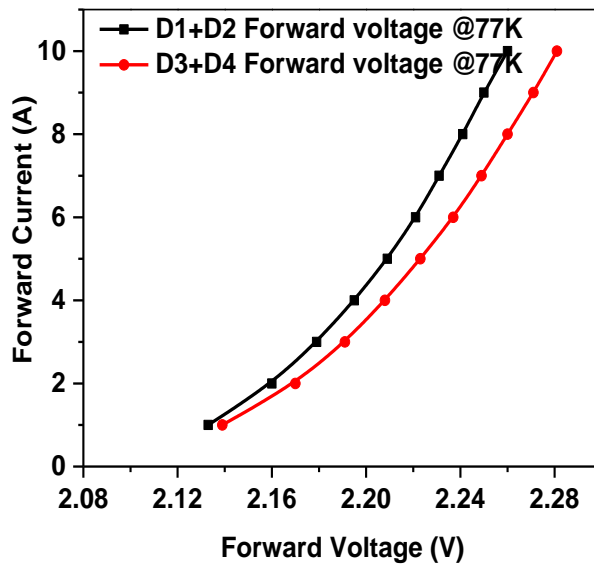


Figure 6.14 Forward characteristics of the back-to-back diode assembly of the PCS assembly at 77 K.

V-I characterizations of the back-to-back diode assembly for the PCS at 300 K and 77 K are shown in Fig.6.13 and Fig.6.14, respectively. The diode assemblies perform admirably at both 300 K and 77 K. Due to limitations in the test setup, the assembly was not tested at 4.2 K.

In the case of the PCS, the on-state resistance is around 15  $\Omega$ . Thus, if more than 0.6 A of current is induced in the EIS coil, the voltage across the PCS is 9 V. In addition, the current bypasses through the diode assembly when the series voltage of both diodes is around 8.9 V.

During testing of the diodes at 77 K and 4.2 K, each of the diodes was kept at the operating temperatures for at least an hour. In addition, each of the diodes was gone through the thermal cycling between 77 K or 4.2 K and 300 K at least for 2-3 times during the experiments. No physical damage was observed in the packaging of the diodes due to their usage at cryogenic temperature.

## 6.7 Summary

V- I characteristics of power diodes were studied at various temperatures to analyze their behaviors under different operating conditions. At room temperature (300 K), the power diodes exhibited a forward voltage drop in the range of 0.6-0.8 V and a reverse leakage current that is usually negligible. At lower temperatures, such as 77 K and 4.2 K, the characteristics of the power diodes changed significantly due to reductions in the thermal energy and mobility of carriers. The forward voltages of the HFR 120 and the BYV 28-200 are 4.78 V and 4.5 V at 4.2 K, respectively. The commercially available packages of both diodes were found to be suitable for the cryogenic temperature range. No deterioration was found in either of the packages at 77 K and 4.2 K. The performances of the diodes were certified at low temperatures.

## CHAPTER 7

### CONCLUSION, FUTURE SCOPE AND SOCIAL IMPACT

In conclusion, this comprehensive study has significantly advanced the development and understanding of critical components within a 1.5 T actively shielded superconducting MRI magnet, addressing both theoretical and practical aspects that are essential for optimizing MRI performance.

The development of the 4 K insert has been a key achievement, enabling precise characterization of superconducting joints. The measured electrical resistance as low as  $8 \times 10^{-15} \Omega$  at zero field between different conductors, such as Cu -NbTi and CuNi-NbTi, highlights the effectiveness of the insert in achieving near-perfect superconducting conditions. The ability to induce a current of 525 A in the secondary coil or the test coil, further underscores the capability of the 4 K insert to simulate operational conditions, providing insights into the joint's behavior and ensuring its reliability in actual MRI applications. Long-term field decay measurements have also confirmed the stability and performance of these joints, ensuring that they meet the stringent demands of MRI technology.



The research has also focused on the development and testing of a prototype PCS for a whole-body MRI magnet, a crucial component for ensuring the magnet's stability and operational efficiency. The comparative analysis of temperature profiles and switching behaviour with various thermo-foil heaters has been instrumental in identifying optimal operating conditions. Specifically, FH2 with a 250-mA input current, was found to offer the best performance by creating a balanced temperature profile while minimizing heat dissipation during ramping. These findings have been used to fine-tune the input parameters for the final PCS, ensuring that it meets the operational demands of the MRI system.

The investigation into the electromagnetic interference shielding (EIS) coil has provided a deeper understanding of the complex interplay between various design parameters. The research demonstrated that the axial width of each EIS coil plays a more significant role than radial separation in achieving peak-to-peak homogeneity in the field of view at the MRI magnet's iso-center. By varying the turns ratio, the study was able to balance mutual inductance, coupling factor, and screening effectiveness. It was found that a moderate turns ratio, as seen in the EIS coils of Case-2 and Case-3, offered the best combination of homogeneity and screening, which is crucial for maintaining image quality and system stability in a 1.5 T MRI magnet. The analysis also extended to the behavior of the EIS coil during quench scenarios, providing valuable data for improving the safety and reliability of the MRI system under various operational conditions.

Furthermore, the study of power diodes at cryogenic temperatures has yielded important findings for their application in MRI systems. The V-I characteristics of power diodes such as HFR 120 and BYV 28–200 were extensively analyzed, revealing significant changes in their behavior at lower temperatures, such as 77 K and 4.2 K, compared to room temperature. The increased forward voltage drops at these temperatures and the negligible reverse leakage current confirmed the diodes' suitability for cryogenic environments. Importantly, the diodes' performance at low temperatures was certified, with no observed deterioration in their commercial

packages, ensuring their reliability when used in the EIS PCS protection circuit. The HFR 120 diodes, in particular, were integrated into the circuit, enhancing the overall safety and efficiency of the system.

In summary, this thesis has provided a detailed and rigorous exploration of the development, optimization, and testing of essential components for a 1.5 T MRI magnet. The insights gained from the superconducting joint characterization, PCS and EIS coil design, and cryogenic diode performance offer valuable contributions to the field of MRI technology. These advancements not only improve the reliability and performance of MRI systems but also set the stage for future innovations in superconducting magnet design and application. This work has laid a robust foundation for further research and development, paving the way for more efficient and effective MRI technologies in both clinical and research settings.

The research presented in this thesis opens several avenues for future exploration and development in the field of superconducting MRI technology. One promising area is the further refinement of superconducting joint fabrication techniques. While the solder matrix replacement method has shown significant improvements, there is potential for developing new lead-free superconducting materials or processes that could further reduce resistance and enhance joint stability under varying operational conditions.

The rapid growth of High-Temperature Superconducting (HTS) technology is driving the need for further research into MRI Field. Developing efficient HTS creating reliable superconducting joints between HTS and LTS materials are key research areas with significant potential. Success in these areas could greatly enhance the performance and efficiency of MRI systems and other applications in the superconductivity field. If the superconducting joints perform well, they could lead to breakthroughs in the MRI industry, among other sectors.

Lastly, the development of higher field strength MRI magnets, such as 7 T or beyond, could benefit from the methodologies and insights gained in this study. As MRI technology advances, there will be a growing need to scale these findings to

accommodate the increased demands of higher-field systems, which could revolutionize medical imaging and research.

The advancements in MRI technology resulting from this research have significant social implications, particularly in the fields of healthcare and medical diagnostics. The development of more reliable and efficient MRI systems directly contributes to the improvement of diagnostic accuracy, enabling earlier and more precise detection of medical conditions such as tumors, neurological disorders, and cardiovascular diseases. This, in turn, can lead to better patient outcomes, as timely and accurate diagnosis is critical for effective treatment.

Moreover, the innovations in superconducting magnet design and the enhanced reliability of MRI systems could make advanced imaging technology more accessible. As these technologies become more refined and cost-effective, it may be possible to reduce the overall cost of MRI systems, making them more widely available in healthcare facilities, including those in underserved or remote areas. This increased accessibility can help bridge the gap in healthcare disparities, providing high-quality diagnostic tools to populations that previously lacked access.

In addition to healthcare, the broader implications of this research extend to scientific research and industrial applications. High-field MRI systems are crucial tools in neuroscience, materials science, and chemistry, among other fields. The improved performance and reliability of MRI magnets could accelerate discoveries in these areas, leading to advancements in our understanding of complex systems, the development of new materials, and innovations in other industries.

In conclusion, the research presented in this thesis not only advances the field of MRI technology but also holds the potential for far-reaching social impacts, improving healthcare, advancing scientific research, and contributing to the broader adoption of superconducting technologies across various industries.

## REFERENCES

- [1] M. Parizh *et al.*, 2017, “Conductors for commercial MRI magnets beyond NbTi: requirements and challenges,” *Superconductor Science and Technology*, vol. 30, no. 1, p. 014007.
- [2] Y. Lvovsky and P. Jarvis, 2005, “Superconducting Systems for MRI—Present Solutions and New Trends,” *IEEE Transactions on Applied Superconductivity*, vol. 15, no. 2, pp. 1317–1325.
- [3] <https://www.classcentral.com/course/mrifundamentals-5043>
- [4] <https://nationalmaglab.org/magnet-academy/read-science-stories/science-simplified/mri-a-guided-tour/>
- [5] D. Folio and A. Ferreira, 2017 "Two-Dimensional Robust Magnetic Resonance Navigation of a Ferromagnetic Microrobot Using Pareto Optimality," in *IEEE Transactions on Robotics*, vol. 33, no. 3, pp. 583-593, doi: 10.1109/TRO.2016.2638446.
- [6] <https://www.imaio.com/en/e-mri/mri-instrumentation-and-mri-safety/magnetic-field-gradients>.
- [7] <http://www.sprawls.org/mripmt/MRI02/index.html>
- [8] F. Nunio *et al.*, 2010 "Mechanical Design of the Iseult 11.7 T Whole Body MRI Magnet," in *IEEE Transactions on Applied Superconductivity*, vol. 20, no. 3, pp. 760-763, doi: 10.1109/TASC.2010.2040265.
- [9] Ogando-Rivas E, Castillo P, Beltran JQ, Arellano R, Galvan-Remigio I, Soto-Ulloa V, Diaz-Peregrino R, Ochoa-Hernandez D, Reyes-González P, Sayour E, 2022 “Mitchell D. Evolution and Revolution of Imaging Technologies in Neurosurgery:.. *Neurol Med Chir (Tokyo)*, 15;62(12):542-551. doi: 10.2176/jns-nmc.2022-0116.
- [10] K. Pieterman and H. Postma, 1984, “A 1.5 T superconducting magnet with closed cooling system for spin-imaging: an outline,” *Cryogenics*, vol. 24, no. 2, pp. 59–62.
- [11] K. Pieterman *et al.*, 1986 “Low Temperature Closed Cooling System for MRI Magnets,” in *Advances in Cryogenic Engineering*, Boston, MA: Springer US, pp. 533–541.
- [12] Y. Iwasa, 1994, *Case Studies in Superconducting Magnets: Design and Operational Issues*, 2<sup>nd</sup> edition. Springer.
- [13] Institute of Cryogenics and Superconductivity Technology, “MICE/MuCool Coupling Magnet Engineering Design,” China, 2008.
- [14] L. Wang *et al.*, 2011“Study on the mechanical instability of MICE coupling magnets,” *IEEE Transactions on Applied Superconductivity*, vol. 21, no. 3 PART 2, pp. 2363–2366.
- [15] M. A. Green and S. Q. Yang, “The Coil and Support Structure Stress and Strain the MICE Focusing and Coupling Magnets,” 2004.
- [16] L. Wang *et al.*, 2009, “Magnetic and cryogenic design of MICE coupling solenoid magnet system,” in *IEEE Transactions on Applied Superconductivity*, pp. 1344–1347.
- [17] S. Q. Yang *et al.*, 2005 “The Mechanical and Thermal Design for the MICE Focusing Solenoid Magnet System,” *IEEE Transactions on Applied Superconductivity*, vol. 15, no. 2, pp. 1259–1262.

- [18] L. Wang *et al.*, 2008 “The engineering design of the 1.5 m diameter solenoid for the MICE RFCC modules,” *IEEE Transactions on Applied Superconductivity*, vol. 18, no. 2, pp. 937–940.
- [19] T. Schild *et al.*, 2008 “The Iseult/Inumac Whole Body 11.7 T MRI Magnet Design,” *IEEE Transactions on Applied Superconductivity*, vol. 18, no. 2, pp. 904–907.
- [20] T. Schild *et al.*, 2010 “The Iseult/Inumac Whole Body 11.7 T MRI Magnet R&D Program,” *IEEE Transactions on Applied Superconductivity*, vol. 20, no. 3, pp. 702–705.
- [21] C. Berriaud *et al.*, 2010 “Conductor R&D for the Iseult/INUMAC Whole Body 11.7 T MRI Magnet,” *IEEE Transactions on Applied Superconductivity*, vol. 20, no. 3, pp. 1408–1411.
- [22] C. Berriaud *et al.*, 2012 “Iseult/INUMAC 11.7 T Conductor Production Status,” *IEEE Transactions on Applied Superconductivity*, vol. 22, no. 3, pp. 6001104–6001104.
- [23] H. Kanithi *et al.*, 2014 “Production Results of 11.75 Tesla Iseult/INUMAC MRI Conductor at Luvata,” *IEEE Transactions on Applied Superconductivity*, vol. 24, no. 3, pp. 1–4.
- [24] T. Schild *et al.*, 2010 “The Iseult/Inumac Whole Body 11.7 T MRI Magnet R&D Program,” *IEEE Transactions on Applied Superconductivity*, vol. 20, no. 3, pp. 702–705.
- [25] L. Quettier *et al.*, 2014 “Status of the Shielding Coil Fabrication for the Iseult/INUMAC Whole Body 11.75 T MRI Magnet,” *IEEE Transactions on Applied Superconductivity*, vol. 24, no. 3, pp. 1–4.
- [26] L. Quettier *et al.*, 2015 “Status of the Shielding Coils Fabrication for the Iseult/INUMAC Whole Body 11.75 T MRI Magnet,” *IEEE Transactions on Applied Superconductivity*, vol. 25, no. 3, pp. 1–4.
- [24] T. Schild *et al.*, 2016 “Iseult/INUMAC 11.7-T MRI Assembly Status,” *IEEE Transactions on Applied Superconductivity*, vol. 26, no. 4, pp. 1–4.
- [28] L. Quettier *et al.*, 2016 “Expected Magnetic Field Quality From the Preliminary Measurements Performed During the Manufacturing of the Iseult/Inumac Whole-Body 11.7-T MRI Magnet,” *IEEE Transactions on Applied Superconductivity*, vol. 26, no. 4, pp. 1–4.
- [29] L. Quettier *et al.*, 2018 “Manufacturing Completion of the Iseult Whole Body 11.7 T MRI System,” *IEEE Transactions on Applied Superconductivity*, vol. 28, no. 3, pp. 1–4.
- [30] L. Li *et al.*, 2012, “Effect of pretension, support condition, and cool down on mechanical disturbance of superconducting coils,” *IEEE Transactions on Applied Superconductivity*, vol. 22, no. 2, pp. 3800104–3800104.
- [31] Y. Li *et al.*, 2017 “Design of the superconducting magnet for 9.4 Tesla whole-body magnetic resonance imaging,” *IOP Conference Series: Materials Science and Engineering*, vol. 171, no. 1, p. 012105.
- [32] L. Li *et al.*, 2017 “Numerical Analysis of Mechanical Behavior for a 9.4-T Whole-Body MRI Magnet,” *IEEE Transactions on Applied Superconductivity*, vol. 27, no. 4, pp. 1–5.
- [33] Y. Dai *et al.*, 2012 “Structural design of a 9.4 T whole-body MRI superconducting magnet,” *IEEE Transactions on Applied Superconductivity*,

- vol. 22, no. 3, pp. 4900404–4900404.
- [34] J. Overweg, 2006, “MRI main field magnets,” in *Proceedings of the 14th ISMRM*.
- [35] Y. Lvovsky *et al.*, 2013, “Novel technologies and configurations of superconducting magnets for MRI,” *Superconductor Science and Technology*, vol. 26, no. 9, p. 093001.
- [36] Collins, S.C., 1955 “Some experiments with persistent currents”, (unpublished report).
- [37] Leupold, M. J., & Iwasa, Y., 1976 "Superconducting joint between multifilamentary wires 1. Joint making and joint results", *Cryogenics*, 16(4), pp.215–216.
- [38] Iwasa, Y., April 1976 "Superconducting joint between multifilamentary wires 2. Joint evaluation technique", *Cryogenics*, 16(4), pp.217–219.
- [39] R. F. Thornton, Superconducting joint for superconducting wires and coils, U.S. Patent 4584547, April 1986.
- [40] Tominaka T., Kakugawa S., Hara N., and Maki N., 1991 "Electrical properties of superconducting joint between composite conductors," *IEEE Transactions on Magnetism*, 27(2), pp.1846–1849.
- [41] H. M. Wen, L. Z. Lin and S. Han, 1992 "Joint resistance measurement using current-comparator for superconducting wires in a high magnetic field," in *IEEE Transactions on Magnetism*, vol. 28, no. 1, pp. 834-836.
- [42] Phillip, S., Porto, J. V. & Parpia, J. M., 1995 "Two methods of fabricating reliable superconducting joints with multifilamentary Nb-Ti superconducting wire." *J. Low Temp. Phys.* 101, pp. 581–585.
- [43] Mizumaki, S. & Yamamoto, A. 1997 "Experimental study of current sharing and transfer in superconductor joint," *IEEE Trans. Appl. Supercond.* 7, pp. 805–807.
- [44] Ryan D. T., Jones H., Timms W., and Killoran, N., 1997 "Critical current measurements at electric fields in the pV m/sup -1 regime", *IEEE Transactions on Applied Superconductivity*, pp.1455–1458.
- [45] Cheng, J. *et al.*, 2012 "Fabrication of NbTi superconducting joints for 400-MHz NMR application", *Transactions on Applied Superconductivity*, 22, 4300205.
- [46] Liu J., Cheng J., Zhou F., Wang Q., Chang K., and Li X., 2013 "Electrical properties of cold-pressing welded NbTi persistent joints," *Cryogenics*, 58, pp.62–67.
- [47] Liu, J., Cheng, J. & Wang, Q., 2013 "Evaluation of NbTi superconducting joints for 400 MHz NMR magnet", *IEEE Transactions on Applied Superconductivity*, Vol. 23, pp. 34–39.
- [48] Liu, S., Jiang, X., Chai, G. & Chen, J., 2013 "Superconducting joint and persistent current switch for a 7-T animal MRI magnet", *IEEE Transactions on Applied Superconductivity* 23, 4400504.
- [49] Jaroszynski, J., 2014 "Race against time: resistance of superconducting joints measurements," *Superconductor Science and Technology*, 28(1), 010501.
- [50] G. D. Brittles, T. Mousavi, C. R. M. Grovenor, C. Aksoy, and S. C. Speller, 2015 "Persistent current joints between technological superconductors," *Supercond. Sci. Technol.*, vol. 28, no. 9, p. 093001.
- [51] Brittles G., 2016 "Persistent current joints between NbTi superconducting

- wires," Ph.D. thesis, University of Oxford.
- [52] Motomune, K., Kazutaka, O., Yasunori, K., Tsutomu, Y. & Hiroyuki, W., 2015 "Analysis for formation of the current path in the superconducting joint between Nb-Ti wires with the solder matrix replacement method," *Supercond Sci Technol* 28, 045019.
- [53] Patel, D. *et al.*, 2019 "Niobium-titanium (Nb-Ti) superconducting joints for persistent-mode operation," *Scientific Reports*, 9:14287.
- [54] Santra, S., Davies, T., Matthews, G., Liu, J., Grovenor, C. R. M., & Speller, S. C., 2019 "The effect of the size of NbTi filaments on interfacial reactions and the properties of InSn-based superconducting solder joints," *Materials & Design*, 176, 107836.
- [55] K. Kobayashi, G. Nishijima, A. Uchida, M. Amaya, N. Banno and H. Kitaguchi, 2020 "Development of a Superconducting Joint Resistance Evaluation System," in *IEEE Transactions on Applied Superconductivity*, vol. 30, no. 4, pp. 1-4.
- [56] Weilun Tan, "Different techniques of producing superconducting joints and methods of joints characterization, 2020" *Journal of Physics: Conference Series, IFEMMT- 2020*, Vol. 1635, China Jilin.
- [57] F. Zhou *et al.*, 2013 "Numerical Simulation of NbTi Superconducting Joint with Cold-Pressing Welding Technology," *IEEE Transactions on Applied Superconductivity*, vol. 23, no. 6, pp. 40-45.
- [58] Martin N Wilson, 1983, "Superconducting magnets", Oxford: Clarendon.
- [59] Harrowell, R. V., 1974 "A new superconducting switch," *Journal of Physics D: Applied Physics*, 7(4), pp. 491–499.
- [60] Hagedorn, D., & Dullenkopf, P., 1974 "A fast-acting superconducting switch for protection of superconducting coils in the persistent current mode." *Cryogenics*, 14(8), pp. 429–430.
- [61] S. Yamamoto, T. Yamada and M. Iwamoto, 1988 "Quench protection of persistent current switches using diodes in cryogenic temperature," *PESC '88 Record., 19th Annual IEEE Power Electronics Specialists Conference*, Kyoto, Japan, vol.1, pp. 321-325.
- [62] H. Maeda, M. Urata, Y. Oda, M. Kageyama, and S. Kabashima, 1991 "Instability of persistent current switch," in *IEEE Transactions on Magnetics*, vol. 27, no. 2, pp. 2124-2127.
- [63] T. K. Ko, Y. S. Oh and S. J. Lee, 1995 "Optimal design of the superconducting persistent current switch with respect to the heater currents and the operating currents," in *IEEE Transactions on Applied Superconductivity*, vol. 5, no. 2, pp. 262-265.
- [64] Kazuyuki shibutani, Toshiaki Takagi, Satoshi Itoh, Seiji Hayashi, Masao shimada, and Yoshio kawate, 1997 "Persistent current operation of a cryogen-free NbTi superconducting magnet," *Japanese Journal of Cryogenic Engineering*, Vol.32, No.10, pp.35-42.
- [65] B. Dorri and E. T. Laskaris, 1995 "Persistent superconducting switch for cryogen-free M.R. magnets," in *IEEE Transactions on Applied Superconductivity*, vol. 5, no. 2, pp. 177-180.
- [66] Rock-Kil Ko *et al.*, 2001 "Performance test of a persistent current switch insulated with cotton tape," in *IEEE Transactions on Applied*

- Superconductivity*, vol. 11, no. 1, pp. 2425-2428.
- [67] M. Tomita, K. Nemoto, M. Murakami, K. Sugawara, 2001 "Switching reaction of Nb<sub>3</sub>Sn persistent current switch with a high current capacity", *Physica C: Superconductivity*, Volumes 357–360, Part 2, pp. 1336-1341.
- [68] Park, D. K., Kang, H., Ahn, M. C., Yang, S. E., Yoon, Y. S., Lee, S. J., & Ko, T. K., 2006 "Design and Test of a Thermal Triggered Persistent Current System using High-Temperature Superconducting Tapes," *Journal of Physics: Conference Series*, 43, pp.5–8.
- [69] Ma, W. B., Zhao, L., Zhang, G. Q., Ning, F. P., & Zhu, Z. A., 2011 "Development of a 7 T Experiment System for Superconducting Switch Test", *Journal of Superconductivity and Novel Magnetism*, 24(5), pp. 1803–1807.
- [70] C. Cui, Y. Lei, L. Li, Z. Ni, F. Gao and Q. Wang, 2012 "Performance Test of Superconducting Switch for NMR Magnet," in *IEEE Transactions on Applied Superconductivity*, vol. 22, no. 3, pp. 9502004-9502004.
- [71] Persistent switch control system, superconducting magnet apparatus employing the same, and method of controlling persistent switch, EP2648013, A2, 2012.
- [72] S. Liu, X. Jiang, G. Chai, and J. Chen, 2013 "Superconducting Joint and Persistent Current Switch for a 7-T Animal MRI Magnet," in *IEEE Transactions on Applied Superconductivity*, vol. 23, no. 3, pp. 4400504-4400504.
- [73] C. Cui, J. Cheng, S. Chen, L. Li and X. Hu, 2016 "Design and Test of Superconducting Persistent Current Switch for Experimental Nb<sub>3</sub>Sn Superconducting Magnet," in *IEEE Transactions on Applied Superconductivity*, vol. 26, no. 4, pp. 1-4.
- [74] C. Li *et al.*, 2018 "Design for a Persistent Current Switch Controlled by Alternating Current Magnetic Field," in *IEEE Transactions on Applied Superconductivity*, vol. 28, no. 4, pp. 1-5.
- [75] C. Li *et al.*, 2019 "Persistent Current Switch for HTS Superconducting Magnets: Design, Control Strategy, and Test Results" in *IEEE Transactions on Applied Superconductivity*, vol. 29, no. 2, pp. 1-4.
- [76] Hollis T. J., Non-coupling magnet shielding coil, U.S. patent 0021465 A1, 2004.
- [77] Gabrielse G, Tan J, Clateman P, Orozco L A, Rolston S L, Tseng C H, and Tjoelker , 1991 "A superconducting solenoid system which cancels fluctuations in the ambient magnetic field," *Journal of Magnetic Resonance* 91, 564-572.
- [78] Gabrielse G and Tan J, 1988 "Self-shielding of Superconducting solenoid system," *Journal of Applied Physics* 63 (10), 5143-5148.
- [79] Soeldner L, Davies F, Magnet Assembly, U.S. patent 5329266, 1994.
- [80] Weinstock H 2000 Application of Superconductivity, Kluwer Academic Publishers, 383-414, 2000.
- [81] Lakrimi M., Thomas A. M., Hutton G., Kruij, M., Slade R., Davis P., Marshall C. A., 2011 "The principles and evolution of magnetic resonance imaging," *Journal of Physics: Conference Series*, 286, 012016.
- [82] Jayakumar R, Compensation coil for temporal drift of a superconducting magnet, U.S. Patent 4812797, 1989.
- [83] Schnur G, Superconducting actively shielded magnet, U.S. Patent 828903, 2010.
- [84] Overweg J A, Peeren G N, Magnetic resonance apparatus comprising a superconducting shielding magnet, U.S. patent 5235282, 1993.



- [85] Kellogg J, Confronting challenges to urban-based MRI facilities, *DotMedBusiness News*, pp. 72-3, March 2011.
- [86] Ito, Keita, Ishiyama, Atsushi, Ueda, Hiroshi, & Noguchi, 2019 "Numerical evaluation of reduction methods for screening current-induced magnetic field in a REBCO Multiple coil system for 9.4-T whole-body MRIs", *Teion Kogaku (Online)*, 54(2), pp. 119-126.
- [87] H. Ueda et al., 2015 "Reduction of Irregular Magnetic Field Generated by Screening Current in REBCO Coil," in *IEEE Transactions on Applied Superconductivity*, vol. 25, no. 3, pp. 1-5, Art no. 6603205, doi: 10.1109/TASC.2014.2375953
- [88] S. Kar, N. Suman, T. S. Ram, V. Soni, R. Kumar, S. K. Saini, J. Antony, S. Sahu, M. Kumar, S. Babu et al., 2019, "Development of high homogeneity and high stability 1.5 T superconducting magnet for whole body MRI scanner," *Indian J. Cryog.* 44(1), 193.
- [89] T Davies. C R M Grovenor and S C Speller, 2020, Atmospheric oxidation of NbTi superconductor. *J Alloys Compound*, 848:156345.
- [90] Susie Speller, Timothy Davies, Chris Grovenor., 2022, Persistent Mode Joints from:Handbook of Superconductivity, *Processing and Cryogenics*, doi/10.1201/9780429183027-34
- [91] S. Phillip, J. V. Porto, and J. M. Parpia, 1995, "Two methods of fabricating reliable superconducting joints with multifilamentary Nb–Ti superconducting wire," *J. Low Temp. Phys.* 101, 581–585.
- [92] W. Tan, 2020 "Different techniques of producing superconducting joints and methods of joints characterization," *J. Phys.: Conf. Ser.* 1635, 012008.
- [93] J Nuding, Method of making a superconductive joint. patent, US3422529:1963–1965, 1969.
- [94] F. Zhou et al., 2013 "Numerical Simulation of NbTi Superconducting Joint With Cold-Pressing Welding Technology," in *IEEE Transactions on Applied Superconductivity*, vol. 23, no. 6, pp. 40-45, Art no. 4802706, doi: 10.1109/TASC.2013.2277779
- [95] Mukoyama, Shinichi, 2020, "Superconducting joint technology for a low-temperature superconducting wire", *Teion Kogaku (Online)*, 55(4), 255-261.
- [96] E Karvonen and J-M Rayroux. Electrical connection between superconductors. patent, US3527876, 1970.
- [97] Brittles G., "Persistent current joints between NbTi superconducting wires," Ph.D. thesis, University of Oxford, 2016.
- [98] Banno, N., Kobayashi, K., Uchida, A. et al. 2021, "High-temperature-tolerable superconducting Nb-alloy and its application to Pb- and Cd-free superconducting joints between NbTi and Nb<sub>3</sub>Sn wires", *J Mater Sci* 56, 20197–20207, . <https://doi.org/10.1007/s10853-021-06585-8>
- [99] C A Swenson and W D Markiewicz., 1990, "Persistent joint development for high field NMR", *IEEE Trans. Appl. Supercond.*, 9(2):185–188.
- [100] K Seo, S Nishijima, K Katagiri, and T Okada., 1991, "Evaluation of solders for superconducting magnetic shield", *IEEE Trans. Magn.*, 27(2):1877–1880.
- [101] R F Thornton. Superconducting joint for superconducting wires and coils and method of forming. patent, US4907338, 1990.
- [102] M Hansen and K Anderko. Constitution of Binary Alloys. McGraw-Hill, New

- York, 1958.
- [68] H W King, C M Russell, and J A Hulbert, 1966, “Superconducting transition temperatures in  $\epsilon$ -phase Pb-Bi alloys”. 20(6):600–601.
- [103] G. B. Yntema, 1955, “Superconducting winding for electromagnets,” *Physical Review*, vol. 98, no. 4, pp. 1144–1209,
- [104] J E Evetts and J M A Wade, 1970, “Superconducting properties and the phase diagrams of the Pb-Bi and Pb-In alloy systems.”, *J. Phys. Chem. Solids*, 31(5):973–982.
- [105] C Malseed and W A Rachinger, 1969, “Superconductivity in the lead-bismuth system”, *Scr. Metall.*, 3(2):139–142.
- [106] A M Campbell, J E Evetts, and D Dew-Hughes, 1968, “Pinning of flux vortices in type II superconductors”, *Philos. Mag.*, 18(152):313–343.
- [107] E Evetts and J M A Wade, 1970, “Superconducting properties and the phase diagrams of the Pb-Bi and Pb-In alloy systems”, *J. Phys. Chem. Solids*, 31(5):973–982.
- [108] W H Warren., 1969, “Superconductivity measurements in solders commonly used for low temperature research”, *Rev. Sci. Instrum.*, 40(1):180–182.
- [109] T Mousavi, C Aksoy, C R M Grovenor, and S C Speller, 2016, “Microstructure and superconducting properties of Sn– In and Sn–In–Bi alloys as Pb-free superconducting solders”, *Supercond. Sci. Technol.*, 29(1):15012.
- [110] S A Levy, Y B Kim, and R W Kraft., 1966, “Effect of structure on the superconducting properties of eutectic alloys”, *J. Appl. Phys.*, 37(10):3659–3665.
- [111] Patel, Dipakkumar J., Design and fabrication of solid nitrogen cooled MgB<sub>2</sub> based persistent magnet for MRI application, Doctor of Philosophy thesis, School of Mechanical, Materials and Mechatronic Engineering, University of Wollongong, 2016. <https://ro.uow.edu.au/theses/4748>.
- [112] J. W. Ekin, *Experimental Techniques for Low-Temperature Measurements*, Oxford University Press, Oxford, 2006.
- [113] See [https://trc.nist.gov/cryogenics/materials/material\\_properties.htm](https://trc.nist.gov/cryogenics/materials/material_properties.htm) for more information about Cryogenics Material Properties, Trc.nist.gov, 2020; accessed 9 September 2022.
- [114] K. R. Efferson, 1967 “Helium vapor cooled current leads,” *Rev. Sci. Instrum.* 38, 1776.
- [115] Persistent switch control system, superconducting magnet apparatus employing the same, and method of controlling persistent switch, EP2648013, A2, 2012.
- [116] Willering, G.P., et al., 2015, “Performance of the cold powered cold diodes and diode leads in the main magnets of the LHC”, *IOP Conf. Ser.: Mater. Sci. Eng.* 101, 012076.
- [117] Gui, H., et al, 2020, “Review of power electronics components at cryogenic temperatures”, *IEEE Trans. Power Electron.* 35, 5144–5156.
- [118] Soni, V., Gupta, A., Kar, S., 2022 “High-power cold diodes for the protection of the 1.5 T superconducting MRI magnet system”, *Semi- cond. Sci. Technol.* <https://doi.org/10.1088/1361-6641/ac7163>
- [119] Ostapchuk, M., Dmitry, S., Daniil, S., Sergey, Z., 2022, “Research of static and dynamic properties of power semiconductor diodes at low and cryogenic temperatures”. *Inventions* 7, 96.

- [120] Rajashekara, K., Akin, B., 2013, “A review of cryogenic power electronics - status and applications.” *International electric machines & drives conference*. Chicago, IL, USA, pp 899–904. <https://doi.org/10.1109/IEMDC.2013.6556204>
- [121] Ward, R.R., et al., 2003 “Power diodes for cryogenic operation”, *Proc. IEEE 34th Power Electron. Spec. Conf.* 4, 1891–1896.
- [122] Standard Recover Diode, Vishay, [www.vishay.com](http://www.vishay.com), 2020 [Online]. <https://docs.rs-online.com/39f1/0900766b8130080d.pdf>. Accessed 11 May 2020.
- [123] Ultra-Fast Avalanche Sinterglass Diode, Vishay, [www.vishay.com](http://www.vishay.com), 2020 [Online]. <https://www.vishay.com/docs/86044/byv2850.pdf>. Accessed 11 May 2020.
- [124] Bose, B.K.: *Power electronics and AC. Drives*, Prentice-Hall, Englewood, NJ 1986.



## PLAGIARISM REPORT

**Title of the Thesis:** Field Stability and External Interference Shielding of 1.5 T Clinical MRI Scanner

**Total Pages:** 174

**Name of the Scholar:** Ajit Nandawadekar

**Supervisors:**

- 1) Prof. Mukhtiar Singh
- 2) Dr. Soumen Kar

**Department:** Electrical Engineering

This is to report that the above thesis was scanned for similarity detection. The process and outcome are given below:

**Software used:** Turnitin    **Similarity Index:** 8%    **Total word count:** 45777

**Date:**

**Candidate's Signature**

**Signature of Supervisor(s)**



## CURRICULUM VITAE

**AJIT DATTU NANDAWADEKAR**

Contact No.: 9503876597

E-mail: [ajitnandawadekar21@gmail.com](mailto:ajitnandawadekar21@gmail.com)



**Ajit Nandawadekar** received his B.E degree in Electrical Engineering from the University of Pune, Pune, India, in 2014; and his M.Tech. degree in Power Electronics from the Amrita School of Engineering (ASE), Bangalore, India, in 2017. His current research interests include superconducting magnets, MRI, superconducting joints and switches, power electronics, multiphase drives, and cryogenics engineering.

### WORKING STATUS

- ❖ **Scientist – DESY-XFEL, Hamburg, Germany**  
Period - July 2024 – to present.

### PERSONAL DETAILS

- ❖ **Date of Birth** : 21 June 1993
- ❖ **Visa Status** : Germany skilled worker visa
- ❖ **Language Known** : English, Hindi, Marathi
- ❖ **Nationality** : Indian